

Syracuse University

SURFACE

Dissertations - ALL

SURFACE

6-1-2015

Nanoparticle Biofunctionalization for Self-Assembly and Energy Transfer Applications

Kaitlin Jeanne Coopersmith
Syracuse University

Follow this and additional works at: <https://surface.syr.edu/etd>



Part of the [Physical Sciences and Mathematics Commons](#)

Recommended Citation

Coopersmith, Kaitlin Jeanne, "Nanoparticle Biofunctionalization for Self-Assembly and Energy Transfer Applications" (2015). *Dissertations - ALL*. 278.

<https://surface.syr.edu/etd/278>

This Dissertation is brought to you for free and open access by the SURFACE at SURFACE. It has been accepted for inclusion in Dissertations - ALL by an authorized administrator of SURFACE. For more information, please contact surface@syr.edu.

Abstract

Metal and semiconductor nanocrystals (NCs) have unique optical and physical properties that are dependent on size, composition and morphology. When NCs are coupled to biomolecules, their properties are combined to create unique materials with biomimetic capabilities that can function as biosensors, cellular imaging agents or drug delivery vehicles. Most NCs are synthesized in air free, non-polar conditions, so surface chemistries must be tuned to accommodate hydrophilic biomolecules. This can be achieved through ligand exchange or polymer encapsulation procedures. This work takes advantage of both phase transfer routes to functionalize gold nanoparticles (AuNPs), quantum dots (QDs), and quantum rods (QRs) with DNA and proteins for self-assembly, energy transfer and drug delivery applications.

In the first project, we explored the ability to assemble QDs into clusters with a high degree of control through DNA-mediated interactions. The hydrophobic QDs were first transferred to buffers using a polymer encapsulation approach that used an amphiphilic polymer. The polymer encapsulated QDs were successfully functionalized with oligonucleotides through both EDC/NHS coupling and click chemistry. The final QD/DNA conjugates were assembled into multicolor QD clusters through a colloidal stepwise approach. One of the greatest challenges of this project was an inconsistent batch-to-batch QD/DNA coupling efficiency, which was attributed to the presence of excess polymer, QD aggregates and poor stoichiometry. Purifying QDs via ultracentrifugation in a sucrose density gradient removed excess polymer, leading to a decreased optical scattering and increased DNA loading that was beneficial for increasing coupling efficiency. In these clusters, a decrease in the QD donor emission and an increase in the QD acceptor emission indicated that QD-QD FRET occurred. One disadvantage to using QDs as energy acceptors is their broad absorption profile, which causes them to be coexcited with the donor. To overcome this

limitation, a bioluminescent protein can be used to generate QD emission through bioluminescence resonance energy transfer (BRET) without external excitation.

In the next project, CdSe/CdS quantum rods (QRs) were functionalized with the bioluminescent firefly protein, *Photinus pyralis* (Ppy). The aim of this project was to improve the long-term stability of the QR/Ppy conjugates. To make these conjugates, hydrophobic CdSe/CdS QRs are rendered hydrophilic through a ligand exchange with histidine (His) followed by an additional ligand exchange to conjugate hexahistagged Ppy proteins to QRs (QR/His/Ppy). In these conjugates, there was a decrease in the stability of the BRET over time. The retention of the BRET signal was significantly improved by changing the QR capping ligand prior to protein conjugation from His to glutathione (GSH). This is because the GSH ligands that remain on the QR surface after Ppy coupling are more highly charged than His, leading to more efficient electrostatic repulsions between QRs. To incorporate the improved QR/Ppy nanoconjugates into the QD/DNA clusters, the QR emission should be a result of non-radiative energy transfer contributions only to prevent simultaneous excitation of the energy donor and acceptor. To investigate the contribution from radiative energy transfer to the BRET signal, control experiments were performed that indicated that most of the BRET signal arises from non-radiative energy transfer from the Ppy to the QR.

In the last project, DNA functionalized AuNPs were used as drug carriers for idarubicin (IDA), a clinically approved chemotherapeutic agent. To construct these conjugates, AuNPs are synthesized using a citrate reduction method and a ligand exchange is carried out to exchange the citrate capping molecules with thiol modified DNA and thermoresponsive polymers. Drug binding was investigated using DNA denaturation measurements and kinetic studies. An increase in duplex DNA melting temperature with drug loading verified IDA intercalation at the dsDNA. The kinetics

of drug release were investigated at physiological temperature, where the presence of drug outside of a dialysis membrane was monitored through IDA fluorescence. The low drug release, small dissociation rate constant of 0.05 min^{-1} and high equilibrium constant of $3.0 \times 10^8 \text{ M}^{-1}$ demonstrates that these nanoconjugates can act as efficient vehicles for in vivo drug delivery.

Nanoparticle Biofunctionalization for Self-Assembly and Energy Transfer Applications

by

Kaitlin Jeanne Coopersmith

B.S. State University of New York at Potsdam, 2011

Submitted to the Department of Chemistry in partial fulfillment of the requirements for the degree of

Doctor of Philosophy in *Chemistry*

Syracuse University
June 2015

Copyright © 2015, Kaitlin Jeanne Coopersmith
All Rights Reserved

Acknowledgements

I would like to express my deepest appreciation for my advisor, Dr. Mathew Maye, for his guidance, patience and inspiration throughout these past four years. I am very thankful for everything he has contributed towards my scientific growth and development.

I would like to thank the members of my committee, Dr. Kevin Sweder, Dr. Arindam Chakraborty, Dr. Yan-Yeung Luk, Dr. James Dabrowiak and Dr. Karin Ruhlandt for their support and time during the defense process. I would especially like to thank Dr. James Dabrowiak and Dr. Karin Ruhlandt for their guidance during my time at Syracuse.

A special thanks to my undergraduate research advisors, Dr. Maria Hepel and Dr. Magdalena Stobiecka, who taught me to love research and encouraged me to pursue graduate studies.

I am grateful to the Maye lab group members, past and present, who have provided me invaluable support through insightful discussions and companionship. I would also like to thank the past REU students that I have had the pleasure of working with and mentoring, including David Reishofer, Peter Pruso and Jan Borstelmann.

I would like to acknowledge my oldest and dearest friends, Tara Giovanelli, Michael Dolan and Sierra Friberg for always being there for me. I would also like to thank Peter Rosado for teaching me salsa and giving me advice about post grad school life.

I would like to thank my family including my parents and my sisters, Rose and Michelle, for being very supportive throughout every stage in my educational development. I am extremely grateful that my parents instilled in me the drive for constant learning. I am very thankful for my fiancé, Adam, for always believing in me and pushing me to be the best I can be. His support and companionship has made this journey a lot more memorable. I would also like to thank my future in-laws, the Lawrences, for their encouragement these past few years.

Table of Contents

List of Figures	ix
List of Schemes	xiv
List of Tables	xv
List of Abbreviations	xvi

Chapter 1: Introduction

1.1 Physical and optical properties	2
1.1.1 Metal NCs	2
1.1.2 Semiconductor NCs	4
1.1.2.1 Anisotropic QRs	7
1.2 Nanocrystal Synthesis	9
1.2.1 Core/shell QDs and QRs	10
1.2.2 AuNPs	12
1.3 Surface Chemistry	13
1.3.1 Polymer Encapsulation	14
1.3.2 Ligand Exchange	15
1.4 Nanocrystal Applications	17
1.4.1 Ligand Mediated Self Assembly	17
1.4.1.1 Kinetics	18
1.4.1.2 DNA-Mediated Assembly	22
1.4.2 Resonance Energy Transfer	23
1.4.2.1 Förster Resonance Energy Transfer	25
1.4.2.1 Bioluminescence Resonance Energy Transfer	27
1.4.3 Encoded Nanocarriers	29
1.4.3.1 Drug Release Kinetics	30
1.5 Nanocrystal Characterization	31
1.6 Research	33
1.7 References	34

Chapter 2: Probing the QD-QD Energy Transfer in Self-Assembled Quantum Dot Clusters

2.1 Introduction	43
2.2 Experimental	46
2.2.1 Chemicals	46
2.2.2 Synthesis and Functionalization of QDs	46
2.2.3 DNA Modification of a Solid Support	49
2.2.4 Cluster Assembly and Release	49
2.2.5 Instrumentation	50
2.2.6 Calculations	51
2.3 Results and Discussion	54
2.3.1 DNA Functionalization via Polymer Encapsulation	54
2.3.2 DNA Functionalization via Aqueous Shell Growth	75
2.4 Conclusions	80
2.5 References	82

Chapter 3: Investigating the Colloidal Stability and Energy Transfer of Quantum Rod Bioconjugates

3.1 Introduction	86
3.2 Experimental	90
3.2.1 Chemicals	90
3.2.2 Synthesis and Functionalization of QRs	90
3.2.3 BRET Measurement and Analysis	92
3.2.4 QR Immobilization on Glass Substrates	92
3.2.5 Instrumentation	92
3.2.6 Calculations	94
3.3 Results and Discussion	96
3.3.1 Improving QR/Ppy Colloidal Stability	96
3.3.2 Investigation of BRET of Immobilized QRs	108
3.4 Conclusions	118
3.5 References	120

Chapter 4: Investigating the Drug Binding in Encoded Nanocarriers for the Delivery of Idarubicin

4.1 Introduction	123
4.2 Experimental	126
4.2.1 Chemicals	126
4.2.2 Synthesis and Functionalization of AuNPs	126
4.2.3 Dialysis Monitoring of Drug Release	128
4.2.4 Instrumentation	128
4.2.5 Calculations	129
4.3 Results and Discussion	131
4.4 Conclusions	139
4.5 References	140

Chapter 5: Conclusions and Future Outlook **142**

Curriculum Vitae **145**

List of Figures

Figure 1.1: Schematic illustration showing the interaction between metal NCs with a light wave to produce surface plasmons. Only the electric field plane of light is shown for simplicity.

Figure 1.2 Jabłoński diagram illustrating the effect of decreasing QD size on band gap (E_g)

Figure 1.3 E_g and exciton confinement for different types of core/shell systems.

Figure 1.4: (a) Schematic visualization of how the upper valence orbitals are formed by bonding among the Se atoms. Normal to the long axis (c-axis), the p_x and p_y orbitals bond strongly in each layer giving a band of orbitals. That band is further widened and increased in density by bonding among the layers in the stack along the c-axis. The situation is similar for the p_z orbitals, but the upper part of the band lies lower than that of the p_x and p_y bands owing to the crystal field splitting. (b) When the nanocrystal grows into a rod there are more layers of orbitals in z direction and the net effect is that the width of the p_z band increases more than that of the p_x and p_y bands. That more than compensates for the crystal field splitting and raises the p_z orbital to be the highest lying frontier valence orbital. Copyright © 2008 John Wiley and Sons.

Figure 1.5 Polymer wrapping procedure to increase QD hydrophilicity.

Figure 1.6 Proposed mechanisms for ligand exchange on a NC surface

Figure 1.7 Jabłoński energy diagram illustrating the electronic changes during the FRET process and a donor acceptor pair and resulting spectral change from energy transfer.

Figure 1.8: Firefly bioluminescence mechanism

Figure 2.1: Representative number weighted DLS results for QD_D (blue circles) and QD_A (red circles) of QDs after polymer encapsulation, DNA conjugation and assembly. (i) QD/TOP (QD_D $d_h = 7.8 \pm 2.8$ nm; QD_A $d_h = 6.4 \pm 2.9$ nm); (ii) NH_2 -PEG/EA/QD (NH_2 -PEG/EA/ QD_D ($d_h = 12.9 \pm 3.0$ nm); NH_2 -PEG/EA/ QD_A $d_h = 22.1 \pm 9.0$ nm); (iii) ssDNA/QD (**AB**/ QD_D $d_h = 17.3 \pm 5.5$ nm; **B'**/ QD_A $d_h = 30.0 \pm 8.1$ nm); (iv) Released **AB**/ QD_D + **B'**/ QD_A cluster from solid support ($d_h = 169.1 \pm 36.8$ nm).

Figure 2.2: FTIR for surface linking through EDC/NHS coupling: (i) EA, (ii) NH_2 -PEG, (iii) PSMA, (iv) QD/PEG/EA

Figure 2.3: FTIR for surface linking through click chemistry: (i) Azide, (ii) PSMA, (iii) QD/Azide.

Figure 2.4: Effect of polymer encapsulation and functionalization on QD QY and gel mobility. (0.8-1% Agarose gel, 70-75 V, 40-45 mins)

Figure 2.5: Effect of QD concentration on the final QD/PSMA conjugate.

Figure 2.6: Effect of different polymers on polymer encapsulation product. UV-Vis: (a) QD(520)/PSMA, (b) QD(520)/PMAO, and (c) QD(520)/PIMA; gel electrophoresis and structures of the different polymers used in this study. [QD] = 1 μ M; gel conditions: 0.8% Agarose, 70 V, 45 mins.

Figure 2.7: Effect of polymer encapsulation on the optical spectra and clarity of the QD sample.

Figure 2.8: Sucrose ultracentrifugation results for the purification of QD(570) after PSMA/NH₂-PEG/EA wrapping and phase transfer: (a) image of QD/PSMA/NH₂-PEG/EA conjugates before (1) and after (2) centrifugation under UV light illumination and (b) optical changes in UV-Vis of the QDs before (1) and after (2) purification. Inset: Gel electrophoresis of QD conjugates before (1) and after (2) purification.

Figure 2.9: (a) UV-illuminated image of the sucrose gradient (1) before and (2) after purification and (b) dynamic light scattering results before sucrose purification (grey circles, $d_h = 68.6 \pm 4.3$ nm) and after sucrose purification (blue circles, $d_h = 51.9 \pm 9.9$ nm).

Figure 2.10: The PL monitoring of the MB supernatant for QDs and QRs incubated with the A'/MB solid support: AB(QD(570)) (a) before (i) and after 2 hours of incubation with A'/MB (ii), (b) after the addition of A'' and AB/QR(625) (c) before (i) and after 2 hours of incubation with A'/MB (ii) and (d) after the addition of A''.

Figure 2.11: (a) AB/QR(625) (i) before and (ii) after 2 hours of incubation with A'/MB and (b) azide/QR(625) (i) before and (ii) after 2 hours of incubation with A'/MB; (c) PL decrease for azide/QR(625) in solution.

Figure 2.12: The PL monitoring of the MB supernatant during the assembly of (a) AB/QD(590) at the A'/MB support, (b) B'/QD(630) at the immobilized AB/QD(590) and (c) the release of the DNA-linked AB/QD(590)+B'/QD(630) cluster upon addition of A'' with release times of (iii) 5, (iv) 14, and (v) 24 h. ($r = [\text{QD}(630)]/[\text{QD}(590)] = 1$; $\text{QY}_D = 2\%$, $\text{QY}_A = 1\%$).

Figure 2.13: (a) Peak deconvolution for the released cluster after 24 hours of measured release ($\text{PL}_A/\text{PL}_D = 4.2$), (b) Spectral overlap of the absorbance of the acceptor (QD(630)) with the PL of the donor (QD(590)) and acceptor and (c) FRET efficiency plot for the released cluster ($R_0 = 3.7$ nm).

Figure 2.14: (a) QD/PEG/EA before (i) and after (ii) incubation with A'/MB and (b) after the addition of a fuel strand for (i) 2 hours and (ii) 14 hours.

Figure 2.15: The PL monitoring of the supernatant during the assembly of AB/QD(570) at the A'/MB support (a), the B'/QD(635) at the AB/QD(570) immobilized on the A'/MB (b), and the release of the DNA-linked AB/QD(570)+B'/QD(635) cluster upon addition of A''-F (c), with release times of 2, 5, and 14 h.

Figure 2.16: PL spectral changes for release of AB/QD(570) + B'/QD(635) clusters after introducing fuel strand A'' at assembly ratios, $r = [\text{B}'/\text{QD}(635)] / [\text{AB}/\text{QD}(570)] = 0$ (a), 0.1 (b), 0.25 (c), 0.50 (d), 0.95 (e), and ~ 1.3 (f). Arrow indicates release times of 2, 5, and 14 h. ($\text{QY}_D = 6.7\%$, $\text{QY}_A = 1.8\%$).

Figure 2.17: (a) The PL and UV-vis spectra for QD(570) (green) and QD(635) red. (b) Spectra overlap of QD(570) energy donor and QD(635) energy acceptor. (c) Observed PL intensity

changes between the QD(570) donor (PL_D) and QD(635) acceptor (PL_A) for the released $AB/QD(570) + B'/QD(635)$ clusters at increasing r (i). Red dashed line (ii) represents simulated PL_A/PL_D based on individual QY values. Inset: Corresponding FRET efficiency plot.

Figure 2.18: The PL monitoring of the MB supernatant during the assembly of (a) $AB/QD(570)$ at the A'/MB support, (b) $B'/QD(630)$ at the immobilized $AB/QD(570)$ and (c) the release of the DNA-linked $AB/QD(570)+B'/QD(630)$ cluster upon addition of A'' with release times of (iii) 2, (iv) 5, and (v) 14 h. ($r = [QD(630)]/[QD(570)] = 0.3$; $QY_D = 2\%$, $QY_A = 5\%$).

Figure 2.19: FRET parameters for the assembled cluster: (a) Spectral overlap of the absorbance of the acceptor (QD(630)) with the PL of the donor (QD(570)) and acceptor.

Figure 2.20: Fluorescence lifetime measurements for (i) QD(530) in the absence of the acceptor (τ_D) and (ii) donor in the presence of the acceptor (τ_{DA}). Data was fit to a biexponential fit.

Figure 2.21: Spectral change with time of ZnS shell growth on CdSe/CdS-His conjugates in the presence of MPA: (a) UV-Vis, (b) PL and (c) emission wavelength as a function of time.

Figure 2.22: (a) UV-vis and (b) PL of QD/His (CdSe/CdS-His) and QD/DNA (CdSe/CdS/ZnS-DNA) after ZnS shell growth in the presence of DNA ($r [DNA] / [QD] = 100$); (c): Gel electrophoresis of CdSe/CdS/ZnS-DNA conjugates after ZnS shell growth in the presence of DNA with different DNA/QD ratios ($r = 0-100$). Inset: UV-illuminated image of QD/His and QD/DNA ($r = 100$).

Figure 2.23: The PL monitoring of the MB supernatant during the assembly of (a) $AB/QD(590)$ at the A'/MB support, (b) $B'/QD(620)$ at the immobilized $AB/QD(590)$ and (c) the release of the DNA-linked $AB/QD(590)+B'/QD(620)$ cluster upon addition of A'' with release times of (iii) 2, (iv) 5, and (v) 22 h. ($r = [QD(630)]/[QD(590)] = 1$; $QY_D = 0.4\%$, $QY_A = 1.7\%$).

Figure 2.24: (a) Peak deconvolution for the released cluster after 22 hours of measured release ($PL_A/PL_D = 32$), (b) spectral overlap of the absorbance of the acceptor (QD(615)) with the PL of the donor (QD(590)) and acceptor and (b) FRET efficiency plot for the released cluster.

Figure 2.25: PL of the QD cluster release at the solid support for (a) QDs functionalized with DNA via polymer wrapping procedure (QD/PSMA/DNA) and (b) QDs functionalized with DNA via the direct attachment procedure (QD/pt-DNA).

Figure 3.1: (a) TEM of CdSe QR core and (b) TEM of CdSe/CdS QR(665) core/shell; (c) ensemble fluorescence polarization measurements of (i) Rhodamine 6G, (ii) core and (iii) core/shell QRs.

Figure 3.2: (a) BRET measurement for QR(665) ($BR = 3$); (b) spectral overlap ($J = 1.3 \times 10^{-11} \text{ cm}^{-6}$), (c) energy transfer efficiency plot ($R_0 = 10 \text{ nm}$).

Figure 3.3: BRET stability of (a) QR/His/Ppy conjugates over time; (b) scatter plot of (i) QR/His/Ppy BRET stability and (ii) Ppy bioluminescence stability over time.

Figure 3.4: BRET at (i) 20 mins and (ii) 360 mins of (a) QR/His/Ppy, (b) QR/TGA/Ppy and (c) QR/GSH/Ppy. Inset: UV illuminated images of the solutions prior to BRET measurements.

Figure 3.5: FTIR of (i) GSH and (ii) QR/GSH.

Figure 3.6: FTIR of (i) Ppy, (ii) QR/GSH, (iii) QR/GSH/Ppy

Figure 3.7: Effect of Ppy loading ($L = [\text{Ppy}]:[\text{QR}]$) on (a) the BRET signal and (b) BRET efficiency.

Figure 3.8: BRET stability of (a) QR/GSH/Ppy; (b) scatter plot of (i) QR/His/Ppy BRET stability and (ii) QR/GSH/PPy BRET stability over time.

Figure 3.9: Bioluminescence of QR/His + non-histagged Ppy.

Figure 3.10: Qualitative molecular calculations for Ppy of (a) surface charge and (b) hydrophobicity (red regions are hydrophobic).

Figure 3.11: Probing the energy transfer of QR/Ppy conjugates (a) BRET of QR/Ppy; (b) Bioluminescence of (ii) QR/PEG-SH+Ppy and (iii) Ppy alone; (c) Ppy intensity for the different conjugates to investigate the extent of energy transfer.

Figure 3.12: Bioluminescence of QR/GSH/Ppy (a) before and (b) after the addition of imidazole ($[\text{Imidazole}]:[\text{QR}]=100,000$); (c) change in LH_2 +Ppy intensity for the different nanoconjugates.

Figure 3.13: (a) Bioluminescence of QR/GSH/Imidazole+Ppy (b) Ppy intensity for the different nanoconjugates.

Figure 3.14: (a) UV-Vis and (b) PL spectra of (i) unsilanized glass after incubation with QDs for 7 hrs in toluene and (ii) silanized glass after incubation with QDs for 7 hrs in toluene; (c) UV illuminated image of an unsilanized blank slide, (i) unsilanized glass slide after QD incubation and (ii) silanized glass slide after QD incubation.

Figure 3.15: Fluorescence spectra showing the effect of different QD/TOPO incubation times with silanized and unsilanized glass (i) unsilanized glass incubated for 74 hours, (ii) unsilanized glass incubated for 7 hours, (iii) silanized glass incubated for 7 hours and (iv) silanized glass incubated for 74 hours.

Figure 3.16: Effect of solvent on QR glass incubation: (1a) QR/TOPO in toluene and (1b) QR/His in borate buffer; (2) TEM of QR/TOPO (Aspect ratio = 3.72) (3a) AFM of QR/TOPO and (3b) AFM of QR/His.

Figure 3.17: Quantification of QD(655) on glass: (a) UV-Vis of the QD glass supernatant (i) before and (ii) after glass incubation ($\epsilon_{\text{QD}} = 2.1 \times 10^6 \text{ M}^{-1}\text{cm}^{-1}$); (b) Fluorescence spectra for known QD concentrations drop casted on glass and (c) Beer's Law plot for the fluorescence spectra ($y = 9.59x - 2.82$; $R^2 = 0.98$)

Figure 3.18: FTIR: (i) MPTS, (ii) Silanized glass, (iii) QD/His on glass. These samples were baseline corrected using a piece of glass freshly cleaned with piranha solution.

Figure 3.19: (a) False color confocal image for glass with QD655 (red) excited with a 405 nm laser and under 10x magnification; (b) PL of QD655 on glass.

Figure 3.20: False color confocal images for glass with QD515 (green): (1a) Overlay of fluorescence images for the QD515 and the QD580 channel ($\lambda_{\text{ex}} = 405 \text{ nm}$), (1b) Fluorescence of the QD515 channel ($\lambda_{\text{ex}} = 405 \text{ nm}$), (1c) Fluorescence emission from the QD580 channel ($\lambda_{\text{ex}} = 405 \text{ nm}$); (2) Overlay of both channels, excited at 488 nm; (3) Overlay of the emission from QD515 and QD580 ($\lambda_{\text{ex}} = 633 \text{ nm}$).

Figure 3.21: False color confocal images for glass with QD580 (purple): (1a) Overlay of the fluorescence channels for QD515 and QD580 excited at 405 nm, (1b) Fluorescence channel for QD 515, excited at 405 nm, (1c) Fluorescence intensity for QD580 only excited at 405 nm; (2) Overlay of both channels, excited at 543 nm; (3) Fluorescence emission overlaid for both QDs, excited at 633 nm.

Figure 3.22: False color confocal images for glass with QD515 (green) + QD580 (purple): (1a) Excited at 405 nm overlaid both channels, (1b) Excited at 405 nm channel for QD515 only, (1c) Excited at 405 nm channel for QD580 only; (2) Excited at 543 overlaid both channels; (3) Excited at 633 overlaid both channels.

Figure 3.23: QR/Ppy+LH₂ on glass (a) PL, (b) BL.

Figure 3.24: Confocal imaging of BRET on glass substrates (a) QD(655)/PPy on glass before the addition of LH₂ excited at 633 nm; (b) QD(655)/PPy + LH₂ in the absence of an excitation source; (c) QD(655)/PPy+ LH₂ excited at 633 nm.

Figure 4.1: a) PyMOL representation of the drug molecule complex upon IDA intercalation in the DNA helix; b) chemical structure and functional groups of IDA.

Figure 4.2: (a) TEM and (b) size distribution histogram (c) number weighted DLS spectra for cit/AuNP.

Figure 4.3: (a) Full UV-Vis Spectra for dsDNA/AuNP and cit/AuNP; (b) UV-Vis zoomed into the surface plasmon peak.

Figure 4.4: (a) gel electrophoresis and (b) DLS spectra of the **a**/AuNP and **p-a**/AuNP conjugates

Figure 4.5: Change in absorbance as a function of T_m for **a**/AuNP, **ab**/AuNP, and **p-ab**/AuNP.

Figure 4.6: (a) Thermal denaturation of IDA/**ab**/AuNP loaded with different ratios of drug. (b) Ratio of drug as a function of melting temperature ($y = 66.2 + 0.3x$; $R^2 = 0.92$). ($[\text{ab}/\text{AuNP}] = 7 \text{ nM}$)

Figure 4.7: Results of dialysis experiments monitoring the dissociation of IDA from (i) IDA/**ab**/AuNP ($y = 3.76(1 - e^{-0.05t})$, $R^2=0.96$), and (ii) IDA/**p-ab**/AuNP ($y = 5.96(1 - e^{-0.02t})$, $R^2=0.99$).

List of Schemes

Scheme 2.1: Overview of the QD Polymer encapsulation procedure employed for phase transferring QDs into aqueous environments.

Scheme 2.2: High throughput DNA-mediated assembly of two color QD clusters on a solid support.

Scheme 3.1: Functionalization of QRs with Ppy for BRET studies

Scheme 3.2: Illustration demonstrating the silanization of glass substrate immobilized with QDs.

Scheme 4.1: The polymer and dsDNA functionalization of AuNPs. IDA binding sites are highlighted in red.

Scheme 4.2: Schematic describing the drug equilibrium for the association and disassociation of IDA from the AuNP nanocarrier.

List of Tables

Table 2.1: DNA Quantification

Table 2.2: Biexponential fit results for lifetime measurements

Table 3.1: FTIR Vibrations

Table 3.2: FTIR Vibrations

Table 3.3: Comparison of different techniques to quantify QDs immobilized to glass substrates

Table 3.4: FTIR Vibrations

Table 4.1: Change in AuNP d_h for the various functionalization steps

Table 4.2: Summary of Kinetic and Equilibrium results for the release of IDA from the different nanocarriers at 37 °C.

Table 4.3: Summary of Published Kinetic and Equilibrium results for the release of DOX and ActD from the different nanocarriers at 37 °C.

List of Abbreviations

α	Percent drug released at equilibrium
ActD	Actinomycin D
Ar	Argon
β	Rate constant
Abs	Absorbance
a_0	Exciton Bohr radius
AFM	Atomic force microscopy
AgNP	Silver nanoparticle
AuNP	Gold nanoparticle
Azide	11-azido-3,6,9-trioxaundecan-1-amine
b.c.c	Body centered cubic
BBS	Borate buffer saline
BL	Bioluminescence
bp	Base pair
BRET	Bioluminescence resonance energy transfer
CCD	Charge coupled diode
$\text{Cd}(\text{CH}_3)_2$	Dimethyl cadmium
CdO	Cadmium oxide
CdS	Cadmium sulfide
CdSe	Cadmium selenide
CdTe	Cadmium teluride
cit	Citrate
COOH	Carboxylic acid
CRET	Chemiluminescence resonance energy transfer
CTAB	Cetyltrimethylammonium bromide
cy3	Cyanine dye 3
d	Diameter
DDA	Dodecylamine
DET	Dexter energy transfer
d_h	Hydrodynamic diameter
DL	Diffusion limited
DLS	Dynamic light scattering
DNA	Deoxyribonucleic acid
DOX	Doxorubicin
dsDNA	Double stranded deoxyribonucleic acid
DTT	Dithiothreitol
ϵ	Extinction coefficient
e^-	Electron
E	Energy transfer efficiency
EA	Ethanolamine
$E_{\text{confinement}}$	Confinement energy
EDC	1-Ethyl-3-(3-dimethylaminopropyl) carbodiimide HCl
E_{exciton}	Exciton energy
E_g	Energy gap

f.c.c	Face centered cubic
FeNP	Iron nanoparticle
FRET	Förster resonance energy transfer
FTIR	Fourier transform infrared spectroscopy
GSH	Glutathione
h	Planck's constant
h ⁺	Hole
HeNe	Helium neon laser
His	Histidine
HOMO	Highest occupied molecular orbital
HPA	Hexylphosphonic acid
HSAB	Hard soft acid base
IDA	Idarubicin
J	Spectral Overlap
κ	Orientation factor
k _a	Association rate constant
k _b	Boltzmann constant
k _d	Dissociation rate constant
kDa	Kilodalton
K _{eq}	Equilibrium rate constant
λ	wavelength
L	Loading ratio
LH ₂	Luciferin
LH ₂ -AMP	Luciferyl-adenylate complex
LUMO	Lowest unoccupied molecular orbital
μ	Reduced electron mass
MA	Maleic anhydride
MB	Magnetic bead
m _e	Mass of an electron
MEOH	Methanol
MES	2-(N-morpholino) ethanesulfonic acid
Mg-ATP	Magnesium adenosine triphosphate
MPA	Mercaptopropionic acid
MPTS	3-Mercaptopropyltrimethylsilane
η	Refractive index
NC	Nanocrystal
NP	Nanoparticle
NSET	Nanometal surface energy transfer
OAc	Oleic acid
OAm	Oleylamine
p	Poly-n-isopropyl acrylamide-co-propylacrylamide, T _c = 51 °C
PBS	Phosphate buffer saline
PDB	Protein database
PEG	Jeffamine M1000 polyetheramine
PEG-SH	(11-Mercaptoundecyl)tetra(ethylene glycol)
PIMA	

PL	Photoluminescence
PL _A	Acceptor photoluminescence
PL _{DA}	Photoluminescence of the donor in presence of the acceptor
PL _D	Donor photoluminescence
PMAO	Poly maleic anhydride octadecene
PMT	Photomultiplier tube
PNIPAAm	Poly(N-isopropylacrylamide)
pol	Polarization
Ppy	<i>Photinus pyralis</i>
PSMA	Poly(styrene-co-maleic anhydride)
pt-DNA	Phosphorothiolate modified DNA
QD	Quantum dot
QR	Quantum rod
QY	Quantum yield
r	Acceptor to donor QD concentration ratio
R ₀	Förster distance
RDS	rate determining step
rh6g	Rhodamine 6G
RL	Reaction limited
rpm	Rotations per minute
R _y	Rydberg constant
SPR	Surface plasmon resonance
ssDNA	Single stranded DNA
Sulfo-NHS	N-hydroxysulfosuccinimide
τ _D	Fluorescence lifetime of the donor
τ _{DA}	Fluorescence lifetime of the donor in the presence of the acceptor
%t	Percent transferred
TBP	Tributylphosphine
T _c	Critical temperature
TCEP	Tris(2-carboxyethyl) HCl
τ _D	Donor decay
TDPA	Tetradecylphosphonic acid
TEM	Transmission electron microscopy
TGA	Thioglycolic acid
THF	Tetrahydrofuran
T _m	Melting temperature
TOP	Trioctylphosphine
TOPO	Trioctylphosphine oxide
UV-Vis	UV-visible spectroscopy
ζ	Zeta potential
ZnAc	Zinc acetate
ZnS	Zinc sulfate

Chapter 1

Introduction

Nanotechnology exploits the unique size dependent optical, electronic and physical properties of nanomaterials derived from metals, metal oxides and semiconductors for a gamut of novel applications. Nanocrystals (NCs) are typically made up of an inorganic core, with at least one dimension on the nanometer scale, that is coated with a monolayer of ligands that influence their properties and functionalities.¹ NCs are increasingly popular for drug delivery and self-assembly applications due to their high surface to volume ratio, surface plasmon resonance (SPR) in noble metal NCs,²⁻¹¹ and quantum confinement in semiconducting NCs, or quantum dots (QDs).¹²⁻¹⁷

The goal of the work presented within this thesis is to create functional nanomaterials for self-assembly, drug delivery and energy transfer applications. In the first project, QDs were functionalized with oligonucleotides and self-assembled using DNA mediated interactions (Chapter 2). QD clusters were assembled with defined stoichiometries on a magnetic solid support and we studied the QD-QD energy transfer that occurred in these clusters. Measuring the energy transfer in these clusters was not straightforward because there was coexcitation of the donor and acceptor due to the broad QD absorption spectra. To overcome this challenge, a bioluminescent protein was directly conjugated to quantum rods (QRs) to create nanoconjugates that emit light without an external light source (Chapter 3). QRs with rod-in-rod microstructures were used because they are the most efficient BRET acceptors. The goal of this work was to overcome colloidal stability issues and to investigate the nature of energy transfer in these nanoconjugates. We increased the colloidal stability by changing the ligand that imparted polar solubility from histidine to glutathione (Chapter 3). In the final project, DNA and polymer functionalized gold

nanoparticles (AuNPs) were used as encoded nanocarriers for the cancer drug idarubicin (IDA) (Chapter 4). We confirmed drug binding through the increase in DNA melting temperature and measured equilibrium rate constants on the order of 10^8 .

1.1 Physical and Optoelectronic Properties of Nanocrystals

1.1.1 Metal Nanocrystals

Colloidal solutions of silver and gold NCs display bright yellow and deep red colors, respectively, due to surface plasmon resonance (SPR).²⁻¹¹ SPR is generated when the free electrons in the conduction band of a material coherently oscillate as a result of electromagnetic excitation. This oscillation causes the displacement of the electron cloud relative to the nuclei due to Coulombic forces as shown in Figure 1.1.^{6,7}

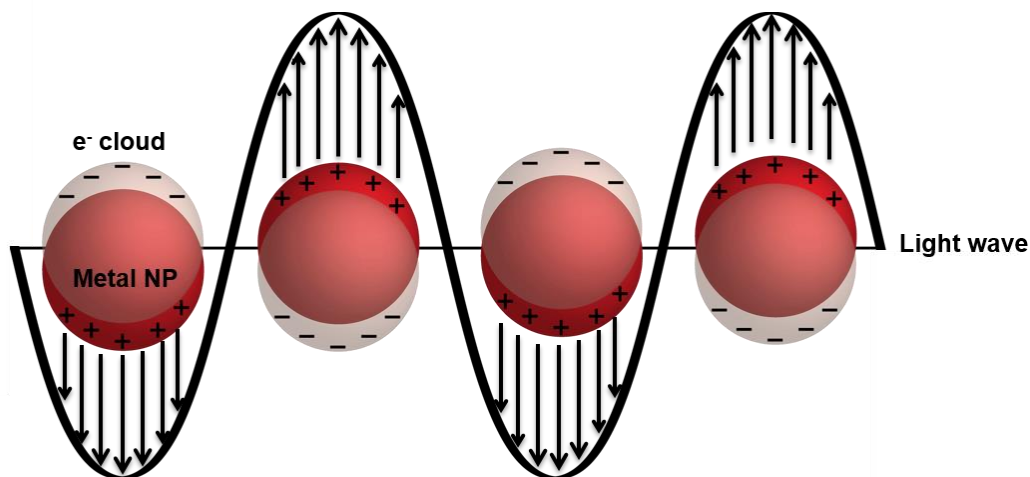


Figure 1.1: Schematic illustration showing the interaction between metal NCs with a light wave to produce surface plasmons. Only the electric field plane of light is shown for simplicity.

SPR is generated for NCs that are smaller than or equal to the wavelength of incident light and create an optical excitation maximum at the plasmon resonant frequency. In noble metal NCs, this plasmon frequency is found in the visible region and quadrupole excitation can increase the

optical absorption into the infrared region. The frequency and width of the SPR band changes with temperature, the density of the electrons, effective electron mass, the shape and the size of the NCs as well as the dielectric constant of the metal and surrounding environment.⁶⁻⁹ This is demonstrated in Equation 1.1.^{18,19}

$$c_{ext}(cm^{-1}) = \frac{24\pi^2 R^3 \epsilon_m^{3/2}}{\lambda} \frac{\epsilon_i}{(\epsilon_r + 2\epsilon_m)^2 + \epsilon_i^2} \quad (1.1)$$

Where c_{ext} is the extinction cross section in single particle, R is the radius, ϵ_m is the dielectric function of the medium, ϵ_r is the real part of the dielectric function, ϵ_i is the imaginary part of the dielectric function, and λ is the wavelength. The c_{ext} is related to the extinction coefficient, ϵ , and Avogadro's number N_A , by Equation 1.2.^{18,19}

$$\epsilon(M^{-1}cm^{-1}) = \frac{10^{-3} N_A c_{ext}}{2.303} \quad (1.2)$$

The SPR electromagnetic field is only present close to the interface so changes in the SPR are sensitive to molecular processes that influence the dielectric property close to the interface.¹¹ As the sizes of metal NCs decrease toward the size where quantum confinement effects predominate, the SPR band dampens in a matter that is inversely dependent on the radius from the scattering of surface electrons.⁸ As the size increases to over 85 nm, there is an increase in scattering efficiency of the NCs that causes a change in the power dependence on the extinction coefficient compared to smaller metal NCs.²⁰ NCs with anisotropic shape can interact with light differently, and a secondary peak can arise from longitudinal SPR, where the energy difference between the two plasmon bands increase as the aspect ratio increases.^{7,21}

1.1.2 Semiconductor Nanocrystals

Unlike metal NCs, semiconductor NCs have strong size-dependent optical properties that arise from the quantum confinement of an electrically neutral quasiparticle called an exciton, which is created when a QD absorbs a photon with enough energy to cause a quantum change ($h\nu > E_g$). The energy gap (E_g) is the energy difference between the frontier orbitals: the Se 4p orbitals in CdSe that make up the top of the valence band, or the highest occupied molecular orbital (HOMO), and the Cd 5s orbitals that make up the bottom of the conduction band, or the lowest occupied molecular orbital (LUMO).^{12,13,17} The wavelength of the emitted photon depends on the degree of quantum confinement, which is a function of the ratio between the square of the Bohr radius of the exciton (a_0^2) and the size of the QDs.¹³

According to Schrödinger's equations for a particle in a 3D box, the energy of confinement of an electron is inversely proportional to the size of the box; this is observed for QDs where a decrease in particle size leads to an increase in emission energy, as shown in Figure 1.2.¹³ As QDs get smaller in size, there are fewer orbital overlaps that cause an increase in the E_g , so the discrete electronic transitions QDs shift to higher energies. Photoexcitation causes an electron (e^-) from the valence band to be excited into the conduction band and leave behind a positively charged hole (h^+).¹⁷ The electron relaxes to the first energy level of the excited state and then recombines with the hole, emitting energy radiatively with light or non-radiatively due to the presence of surface trap states. The amount of emitted energy is quantified through quantum yield (QY). During the emission process, the exciton (e^-h^+ pair) is held together through Coulombic charge interactions, which causes the electronic excitation states to be lower in energy than the E_g by tens of mV.¹⁷ Even though the exciton fine structure excitation energies are lower than E_g , trends in exciton

energy as a function of size, shape or material are still largely dictated by E_g , so the e^-h^+ spatial separation is described using the Bohr radius (a_0).¹⁷

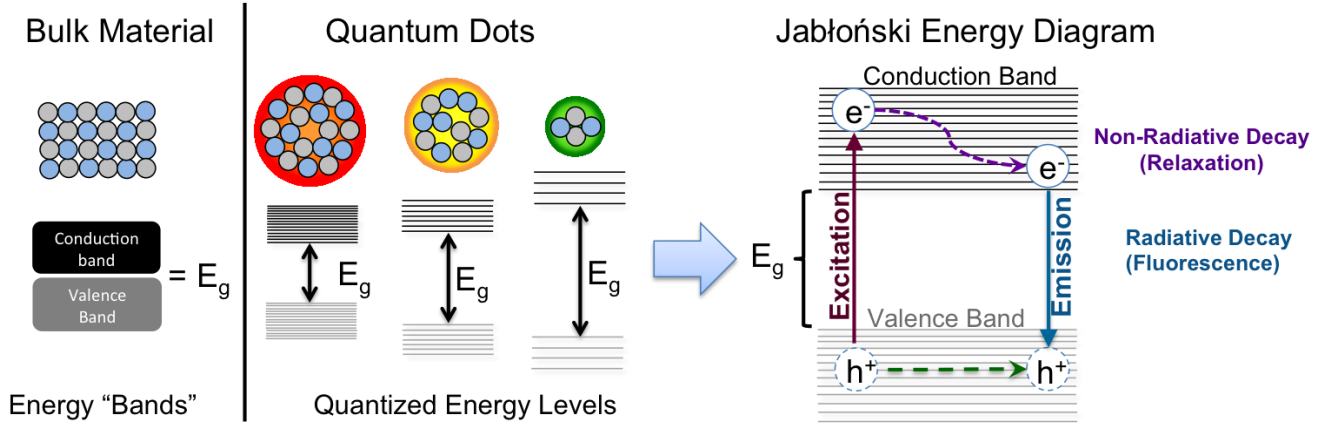


Figure 1.2: Jabłoński diagram illustrating the effect of decreasing QD size on band gap (E_g)

The energy of the emitted wavelength can be calculated using equation 1.3.²²

$$E = E_g + E_{\text{confinement}} + E_{\text{exciton}} = E_g + \left(\frac{h^2 \pi^2}{2a_0^2} \left(\frac{1}{m_e} + \frac{1}{m_h} \right) \right) + \left(-\frac{\mu R_y}{\epsilon^2 m_e} \right) \quad (1.3)$$

Where E_g is the band gap energy, $E_{\text{confinement}}$ and E_{exciton} are the confinement and exciton energies, respectively, h is Planck's constant, a is the radius of the QD, a_0 is the Bohr radius, m_e and m_h are the electron and hole masses, respectively, μ is the reduced mass, R_y is the Rydberg constant and ϵ is the size dependent dielectric constant. As shown in the equation, the emission energy is inversely proportional to the radius of the QD and the dielectric constant of the material.

QDs that are made up of smaller metals with smaller a_0 and larger bulk E_g , such as cadmium chalcogenides, experience quantum confinement at smaller sizes compared to materials with a larger a_0 and smaller E_g , so the emission wavelength can also be tuned by changing the material. CdSe QDs have emission in the visible range while PbSe NCs have been able to emit into the IR region.²³ The absorbance spectra of QDs typically have multiple peaks that arise from the different allowed transitions in the electronic structure. At lower energy wavelengths, the UV-vis spectra

arises from the quantum confinement of the band gap, but at higher energies, the spectra is closer to that of the bulk material and is no longer in the strong confinement regime.¹² The energy of the first transition usually carries most of the oscillator strength.¹² Oscillator strength is an intrinsic property of nanomaterials that is the strength of coupling between two electron states and describes the probability of absorption or emission of electromagnetic radiation.^{24,25} The contribution of light scattering to the absorbance of QDs is usually neglected since the size of the NC is much smaller than the wavelength of light.¹⁵ In semiconductor NCs, carrier confinement dictates the extinction coefficient.¹⁴

Electronically excited QDs typically display a Stokes shift, where the emitted radiation has a lower frequency than the absorbed radiation. This is present when the electron is excited above the first vibrational level of the excited state and non – radiative vibrational relaxation can occur before radiative electronic relaxation to minimize the lifetime of the excited state. Depending on the application, a smaller or larger stokes shift is preferred. For example, incorporation of QDs as a laser requires a large stokes shift to prevent self-absorption. For self-assembly and energy transfer applications, a small stokes shift is desired to minimize non-radiative energy losses, decrease co-excitation and increase the amount of energy available for the system.

The quantum confinement can also be manipulated by growing a shell of a different semiconductive material over the QD core. As shown in Figure 1.3, the exciton confinement is dictated by the E_g alignment between the core and shell materials. In type I materials (e.g: CdSe/ZnS), a shell is grown with a material that has a larger E_g than the core. This eliminates surface trap states and protects the exciton from the environment, leading to an increased QY.^{17,26} Although the core dictates the optical properties, there is typically a small red shift in emission PL after shell growth that is proportional to the reduction in electron confinement. This occurs because

there is a small amount of exciton leakage into the shell material due to the finite energy offset between the core and shell materials. Type I $\frac{1}{2}$, or quasi type II, heterostructures (e.g CdSe/CdS), the h^+ is confined to the core and the e^- is delocalized along the whole crystal.^{17,26} Overgrowth of this type of shell causes a larger red shift and longer exciton radiative lifetimes due to the larger loss of confinement from decreased exciton wavefunction overlaps. In type II heterostructures, such as CdSe/CdTe, the E_g levels are staggered, so the e^- and h^+ are on different sides of the heterojunction.^{17,26} Type II materials (e.g: CdTe/CdSe) have a very small, non-zero exciton overlap. These materials exhibit the largest stokes shift and largest red shift after shell growth.

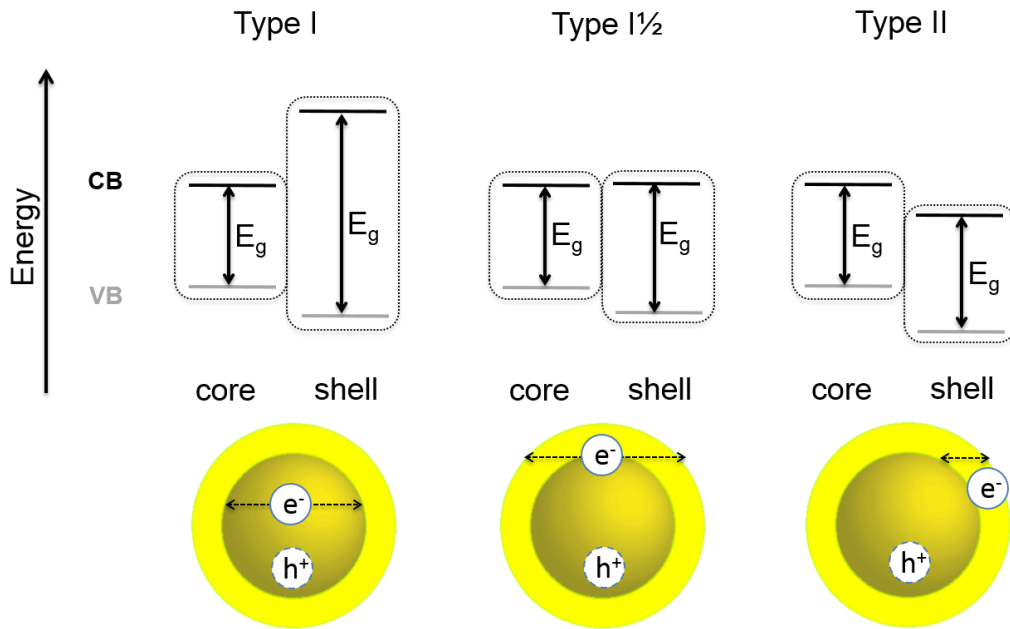


Figure 1.3: E_g and exciton confinement for different types of core/shell systems.

1.1.2.1 Anisotropic QRs

The optical emission properties of semiconductor NCs can be tuned by adjusting the height, width and shape of the potential that confines the exciton.^{16,17} For spherical QDs, the exciton is confined in all directions so it is experienced as zero dimensional. Quantum wires confine the

exciton one dimensionally in the diameter direction and quantum wells confine the exciton two dimensionally in the thickness direction. Quantum rods (QRs), exhibit properties between 0 and 1 dimensionally confined charge carriers, where there is a decrease in confinement along the length direction.²⁷ Consequently, the QRs exhibit E_g and emission wavelengths that are strongly dependent on the diameter and weakly dependent on the length. CdSe QR cores grow along the c -axis. Normal to the c -axis, the Se $4p_x$ and $4p_y$ orbitals bond stronger because of the orbitals directionality. The p_z orbitals lie along the c -axis at lower energies due to crystal field splitting. When growth occurs along the c -axis, the p_z orbital density decreases and the frontier valence band orbitals become dominated by p_z orbitals, as shown in Figure 1.4.¹⁷ This elongation causes the QR optical properties to be linearly polarized along the wurtzite c -axis.^{16,17,27,28} In this thesis, wurtzite type I $\frac{1}{2}$ CdSe/CdS QRs are utilized, which confine the h^+ in the core and delocalizes the e^- along the whole heterostructure. Longer QRs are expected to have longer lifetimes and lower QYs since the e^- is less spatially confined, which causes the e^- and h^+ to be more spatially separated and decreases the chances of recombination.²⁷ Also, the large QR surface area increases the probability of surface trapping that can lead to an increased nonradiative decay rate.²⁷

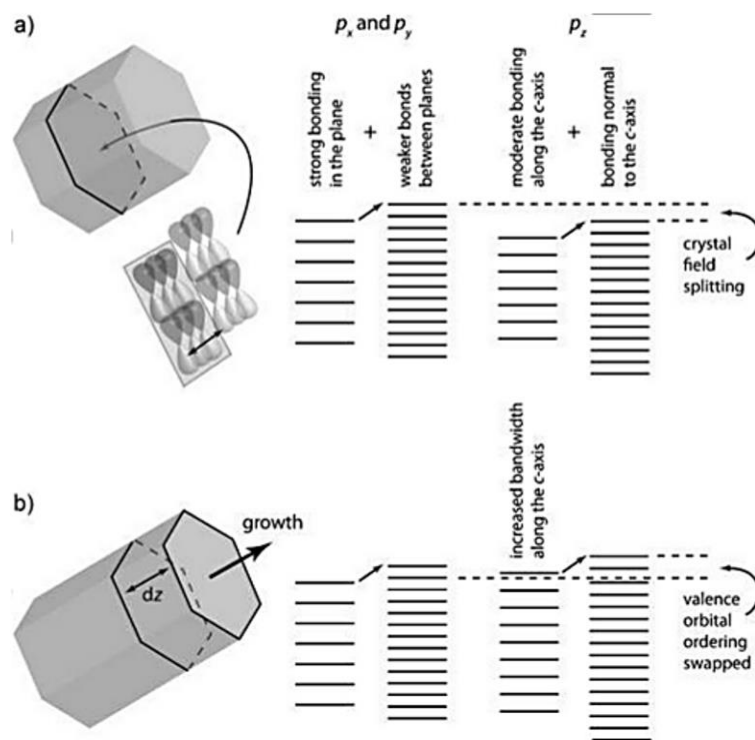


Figure 1.4: (a) Schematic visualization of how the upper valence orbitals are formed by bonding among the Se atoms. Normal to the long axis (c-axis), the p_x and p_y orbitals bond strongly in each layer giving a band of orbitals. That band is further widened and increased in density by bonding among the layers in the stack along the c-axis. The situation is similar for the p_z orbitals, but the upper part of the band lies lower than that of the p_x and p_y bands owing to the crystal field splitting. (b) When the nanocrystal grows into a rod there are more layers of orbitals in z direction and the net effect is that the width of the p_z band increases more than that of the p_x and p_y bands. That more than compensates for the crystal field splitting and raises the p_z orbital to be the highest lying frontier valence orbital. Reproduced with permission from reference 17. Copyright © 2008 John Wiley and Sons.

1.2 NC Synthesis

Colloidal NCs have size dependent physical and chemical properties, making synthetic size control very crucial.^{23,29–31} The stages of NC growth include formation of monomers, nucleation, and growth. An annealing stage can be present in some synthetic protocols, where the growth of NCs stops and equilibrium is achieved to improve the crystallinity and surface quality. Unfortunately, this may also lead to an undesirable broadening of the shape and size distribution.^{23,29} In the beginning of the reaction, the mixture is homogeneous, with no phase

differences in the reaction. The reaction turns into a heterogeneous solution when the nuclei are created, with both solid and liquid phases present. The crystal nuclei have to be above the critical radius, which is the minimum size for a stable nucleus; nuclei smaller than this will redissolve and nuclei larger than this will continue to grow.²³ As the reaction proceeds, the nuclei agglomerate and grow into larger crystals until they reach a saturation point and stop growing or until the reaction is quenched. The chemical potential and solubility of the NC into monomers increases as the size decreases.²⁹

The driving force for crystal growth is the minimization of the free energy of the system, which is the difference between the free energy of the monomers and the crystals in solution.^{23,29} The energy spent breaking the bond between the monomers and the surfactant should be less than the energy freed by forming the chemical bonds in the crystal's nucleus for successful growth.²³ The monomers at the surface of the NC will have unsaturated bonds, increasing the total free energy of the system. This can be minimized by the presence of stabilizing ligands and surfactants, which lower the surface tension of the crystal faces.^{17,23,29}

1.2.1 Core/Shell QDs and QRs

QDs and QRs are typically synthesized at high temperatures through the thermal decomposition of organometallic precursors.²³ For CdSe QDS, a cadmium compound, such as CdO or Cd(CH₃)₂, is dissolved in a solution with ligand to form a cadmium complex.^{23,30} The ligand-cadmium complex is then mixed with a second precursor, a ligand-chalcogenide complex. The Cd complex cleaves the ligand-chalcogenide bond, creating a Cd-chalcogenide bond.³⁰ It was hypothesized that the electron rich chalcogenide binds to Cd²⁺ because the cadmium acts a Lewis acid and facilitates a nucleophilic attack by the ligand. The cleavage of TOP-Se was found to occur

two times faster in the presence of Cd-oleic acid than in the presence of oleic acid, indicating the Lewis acidity of the cadmium.³⁰ It was also observed that changing the concentration of the surfactants changed the rate of the bond cleavage, uncovering their role in monomer formation. The monomer formation is believed to be the rate-limiting step for NC formation.²³

Depending on the temperature and composition of the solution, QDs with different shapes, sizes and microstructures can be created. At higher temperatures and in the presence of phosphonic acids, QDs tend to grow in a wurtzite structure, but at lower temperatures, they tend to adopt a zinc blende structure. At equilibrium conditions with homogenous ligands, NCs will form spherical crystals. To create shapes that are different than those formed at equilibrium conditions, the relative surface tension of the crystal faces can be altered by using surfactants that have facet-selective adsorption.¹⁷ Coordinating ligands bind dynamically; they need to desorb from a site to allow monomers to attach, so stronger binding ligands will impede growth and weaker ligands will enable vectorial growth on the crystal face they are adsorbed to.^{17,23,30,31}

The surfactants change the surface tension of the different crystal faces to different extents through the ligand-NC bonding nature and the solvation of the ligand tails by the solvent.¹⁷ In kinetic growth, the structure that is produced during NC growth is dependent on the relative growth rates of each facet.¹⁷ If one of the crystal faces has a relatively higher surface tension, then the system will want to lower the surface energy by growing along that face, so this face will grow relatively faster. In wurtzite crystals, the (0001) face is anion rich and has more dangling bonds, so anisotropic growth generally grows along this face.^{17,23}

Overcoating the QD or QR core with an inorganic material can alter the degree of the Stokes shift and exciton confinement, depending on the E_g alignment between the different

materials. The thickness of the shell is limited by interfacial strain from the crystal lattice mismatch between the two materials.

1.2.2 AuNPs

The synthesis of metal NCs involves the reduction of metal salt precursors at relatively low temperatures, typically 90-110°C. Common reducing agents are sodium borohydride, which produces smaller crystals, and the weaker sodium citrate, which produces larger crystals. Once the reducing agent is added, the ions are reduced to atoms (Au^0) until the solution is supersaturated, creating the reactive monomers. The Au^0 atoms then coalesce into subnanometer particles that act as nucleation sites for particle growth, called seeds.³² Growth onto the nuclei to form seeds occurs either from the binding of unbound Au^0 atoms in solution, the aggregation of unreacted metal species onto nuclei followed by reduction or the coalescence of two small nuclei together.³² After growth, AgNPs and AuNPs typically adopt a face centered cubic (f.c.c) crystal lattice. Final AuNPs are composed of a core with Au^0 atoms surrounded by a layer of negative ions that creating a particle surface charge. This outer layer can be $[\text{AuCl}_2]^-$ ions, borohydride ions or citrate ions, depending on the reaction conditions. The electrostatic interactions between AuNPs increase the stability and prevent further growth. AuNPs can be grown into rods after they are synthesized through a seeded initiation route, where the addition of a surfactant such as cetyltrimethylammonium bromide (CTAB), which binds preferentially to one of the crystal faces while the other faces agglomerate, leading to growth in one direction. Seedless initiation routes have also been developed to create anisotropic shapes from gold atoms.^{33,34}

1.3 Surface Chemistry

Since up to half of the atoms in a NC can be surface atoms, the NCs properties are sensitive to the surfactant layer. Manipulating the morphology of the ligand-NC interface is pivotal to increase their scope of application.^{1,35,36} Ligands can influence the shape, size, polydispersity, growth rate, optical properties, chemical stability, electronic structure and chemical reactivity of NCs.^{1,30,35-43} To control the optical properties of QDs and QRs, ligands can influence the QY and emission peak, depending on the overlap of the ligand orbitals with the QD band gap.^{35,37,44} If the ligands shift the orbitals of the unpassivated surface molecules away from the HOMO-LUMO gap then they can increase the QY by decreasing non-radiative relaxation. Reduction of these trap states can also decrease the Stokes shift. Poor surface passivation can decrease the QY through aggregation, ligand desorption or surface oxidation.⁴⁴

There are also uncertainties to the ligand layer. For example, ligand binding competition can lead to a surface composition that isn't dependent on the ratio of ligands used during synthesis or ligand exchange.⁴⁵ It was found that chemical impurities in trioctylphosphine oxide (TOPO) influences QD synthesis and lead to a variety of ligands on the surface. The ligands on the surface of NCs dynamically bind on and off of the surface depending on the strength of the metal-ligand bond. To overcome these uncertainties and to increase their scope of applications, a plethora of work has been devoted to ligand characterization techniques, including ligand quantification and kinetics. The chemical modification of NC surfaces is a popular technique to increase the scope of NC applications.

Ligands can impart different functionalities and change the solubility of the NCs. The electrostatic and van der Waals forces for ligand-ligand and ligand-NC interactions dictate the solubility of the NCs and are sensitive to the degree of surface curvature and ligand density.^{39,46}

Strong attractive van der Waals forces cause irreversible agglomeration of particles, whereas repulsive electrostatic interactions stabilize the particles and create a barrier that limits aggregation growth.³⁹ Although the ligand shells govern the particle solubility by kinetically stabilizing the NCs through short ranged ligand-ligand interactions, long ranged van der Waals attraction between NCs make agglomeration energetically favored.³⁹ Ligands tend to dynamically bind on and off of the surface and can bind to certain facets stronger than others depending on binding strength and ligand size.^{1,37,38,42} For stable, non-aggregating particles, the binding rate should be faster than the rate of agglomeration.

To control the properties of AuNPs, QDs and QRs, the ligand layer can be manipulated through polymer wrapping techniques, where an amphiphilic polymer encapsulates the NC surface⁴⁷⁻⁵⁷ or through ligand exchange, where the native capping agents are exchanged either through an increased bond strength or mass action effect. In this thesis, both techniques were employed to impart polar solubility for QDs and QRs and to change the functionalities of AuNPs.

1.3.1 Polymer Encapsulation

One route towards polar solubility is a polymer encapsulation technique.⁴⁷⁻⁵⁷ To accomplish this, non-polar NCs are mixed with an amphiphilic polymer that contains polar and non-polar subunits. As the polarity is increased, the hydrophobic polymer subunits interact with the hydrophobic ligands on the NCs to create a shell surrounding the particle with the hydrophilic subunits exposed to the solvent, as shown in Figure 1.5.^{47,48} The outer polar shell of the polymer wrapped NC is available for further functionalization via attachment chemistries such as EDC/NHS coupling or click chemistry.

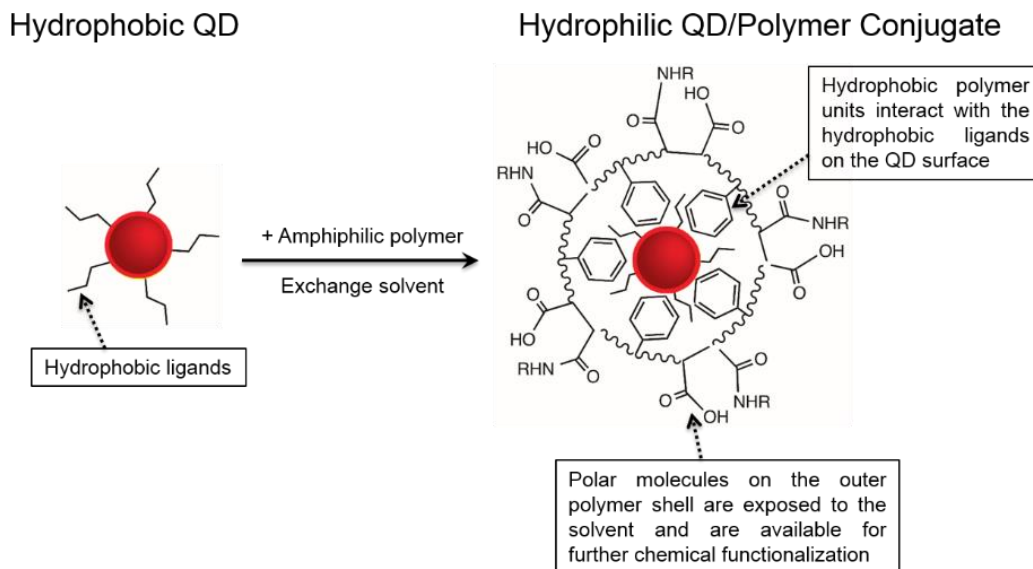


Figure 1.5: Polymer wrapping procedure to increase QD hydrophilicity.

Since the original ligands are retained, polymer coated NCs have displayed an increased long-term stability under a wide range of pH or ionic strengths compared to ligand exchanged QDs.^{47,48} The size of the polymer-NC nanoconjugate depends on the polymer's size and conformation in a solvent, and the method used to encapsulate the NC.⁴⁸ The relative dispersion forces between the two groups depend on the degree of intercalation between the alkyl groups on the NC and the hydrophobic groups on the polymer.

1.3.2 Ligand Exchange

Ligand exchange can be employed to replace the original ligand layer with new ligands to change the NC's solubility and functionality. The ligands on the surface of the NC are in equilibrium with free ligands in the solution and ligand desorption can lead to deterioration of the optical properties, aggregation and precipitation.⁴⁸ During ligand exchange, ligands are replaced either through mass action or competition based on the relative strength of all of the ligands

involved.¹ Ligands are usually composed of an electron-donating coordinating group that has a high affinity for the metal and a non-coordinating group that dictates the reactivity of the NCs.^{1,35} The interactions between the metal and the anchoring group are usually dictated through hard-soft acid-base (HSAB) theory. The most common ligands for AuNPs have a sulfur group, where sulfur can either bind covalently as a thiolate or form a weaker coordination bond through the lone pair electrons of a thiol.^{41,58} The most common ligands for QDs have amino or phosphorus groups. QDs passivated with mercaptans typically display PL quenching from hole trapping.⁴⁴

Ligand adsorption onto NC surfaces is a complex process. NC surfaces have defect sites (edges and vertices) and non-defect sites (terraces) with different chemical reactivities and ligand affinities.⁴⁶ Each of these different sites have different electron densities and steric behavior due to the small size and high surface curvature of NCs.^{36,59,60} The changes in reactivity as a function of NC size, where a size decrease corresponds to an increased rate, has been attributed to the size dependent ratio of defect to non-defect sites.⁵⁹ The degree of dynamic binding depends on the strength of the bond between the NC and anchoring group as well as the size and bulkiness of the ligands. For weakly binding ligands, such as histidine, there is a relatively fast dynamic on and off rate; if there aren't any ligands in the surrounding environment to exchange with the ligands on the surface, NC aggregation is induced. For stable NCs, the ligand's on/off rate should be faster than the rate of NC aggregation. Ligand exchange can be described as either an associative or dissociative mechanism as shown in Figure 1.6.^{36,59} For these mechanisms, there are different rate determining steps (RDS) and different kinetic constants. During the associative mechanism, the incoming ligand binds to the metal and subsequently displaces the old ligand. The RDS is the binding of the incoming ligand to the metal.⁶¹ For a dissociative mechanism to occur, a ligand on

the metal has to depart before the incoming ligand can bind. The RDS for these mechanisms is the dissociation of the outgoing ligand.⁶¹

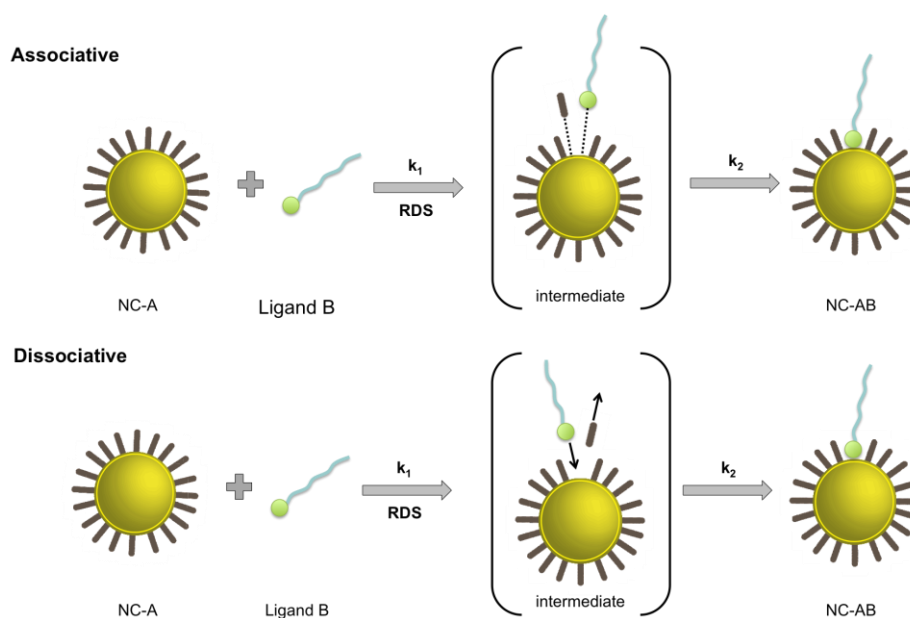


Figure 1.6: Proposed mechanisms for ligand exchange on a NC surface

Compared to the kinetics of ligand exchange for smaller, inorganic complexes, the rate constant for ligand exchange on NCs is typically slower. Ligand substitution in metal complexes have first order rate constants that range from 10^{-5} to 10^9 s^{-1} .^{62,63} In NC systems, the first order kinetic rate constants for ligand exchange were reported to be 10^{-3} to 10^2 s^{-1} .⁴²⁻⁴⁴

1.4 NC Applications

1.4.1 Ligand Mediated Self-Assembly

The main goal of ligand-mediated NC self-assembly is to obtain the controlled formation of organized, complex shapes from initially disordered mixtures of particles that is driven by the interactions between building blocks.⁶⁴ The nature of these selective interactions can be biomolecular such as peptide conjugation⁶⁵ and Watson-Crick base pairing of DNA,^{66,67} chemical

such as the host-guest chemistry of cucurbit[n]urils^{64,68,69} and click chemistry,⁶⁶ or physical such as the interfacial tension at liquid or air interfaces or the presence of an external field.⁷⁰⁻⁷⁵ The coupling of individual components is usually driven by kinetic and thermodynamic forces, where the local interactions between the building blocks minimizes the overall energy of the system.^{64,76-78} Ideal assembly conditions allow for a high degree of control over the resulting architecture, including interparticle distances, composition and long-range order of the constituents.^{77,79} Synergistic properties that arise from linked NCs, such as energy transfer (ET) between chromophores⁸⁰⁻⁸³, or the coupling of metal NC SPR^{68,69} makes these structures unique materials for sensing, energy transfer and catalysis applications.^{64,68-70,75,84}

1.4.1.1 Kinetics

The kinetics of NC self-assembly is dictated by colloidal stability, which is a balance between attractive van der Waals forces and repulsive electrical double layer interactions.⁸⁵ Interparticle forces can be manipulated by changing the particle shape, size and surface chemistry, where the surface ligands provide steric or electrostatic repulsions that influence particle-particle interactions.^{69,76} Since the ligand layer dictates most of the interparticle properties, NC composition does not influence the rate.⁸⁶ Most ligand-mediated self-assembly studies aim to gain control over the interparticle distance and the size and organization of clusters.^{64,76,77} Uncontrolled self-assembly can lead to unwanted organization of the constituents or irreversible precipitation, so the specificity and extent of assembly needs to be highly controlled.

The kinetics of the aggregation of colloidal particles into clusters has been described by a combination of Smolukowski kinetics and a Langmuir-type surface reaction.⁸⁶⁻⁸⁹ Smolukowski kinetics assume that the rate of collision between two particles is proportional to the product of

their concentrations, as shown in Equations 1.4 for low particle concentrations and 1.5 for high particle concentrations.^{90,91}

$$\beta = \frac{2}{3} \frac{k_B T}{\eta} (x_1^{y_1} + x_2^{y_2}) (x_1^{-y_1} + x_2^{-y_2}) \quad (1.4)$$

$$\beta = \frac{2}{3} \frac{k_B T}{\eta} \frac{(x_1 x_2)^{\gamma}}{w} (x_1^{y_1} + x_2^{y_2}) (x_1^{-y_1} + x_2^{-y_2}) \quad (1.5)$$

Where β is the reactivity rate of two particles (x_1, y_1 and x_2, y_2) x is the particle mass, y is the fractal dimension, k_B is the Boltzmann constant, T is the temperature, W is the Fuchs stability ratio, η is the viscosity, and γ is a fitting parameter called the product kernel.⁹¹

Linker-induced aggregation is typically described by a “probability of sticking” term.^{89,92} The probability of the particles sticking is dependent on the concentration of linkers. When no linkers are bound to particles, the probability of two particles sticking together is zero.⁹² Sticking only occurs when the repulsive energy barrier is small ($E < k_B T$) during the collisions between the two molecules involved in the cross-linking.⁸⁶ The higher the energy barrier, the more collisions that have to occur to result in cross linking.⁸⁶ When collision results in formed bonds between the NCs, the cross linking is irreversible and the clusters continue to diffuse, collide and aggregate.⁸⁶ NCs have highly curved and rigid structures, so a high surface coverage of linker groups can increase the rate of aggregation as long as the surface molecules don't prevent binding by blocking access to unbound sites.^{86,92} Two distinct kinetic regimes are usually observed during aggregation with a rate constant that is proportional to the diffusion of the particles toward each other.^{68,87–89} At low particle concentrations or low ionic strengths, the aggregation is reaction-limited (RL), where particle collision is relatively slow due to a decreased probability of collisions, so any formed clusters may have time to rearrange and create more ordered structures.⁸⁸ At higher concentrations or ionic strengths, cluster formation is dependent on diffusion-limited aggregation

(DL). These conditions increase the probability that collisions will occur and the aggregation is limited only by diffusion.^{68,87,88} The repulsive forces are higher for RL aggregation so the rate is limited to the time it takes to overcome these forces; for DL aggregation, the energy barrier of repulsion is much smaller than $k_B T$.^{86,93}

The crossover from RL to DL kinetics has been observed by several different groups by altering reaction conditions.^{68,88} For example, Taylor *et al.* compared the integrated extinction over time for the coupling of curcubit[5]uril (CB5) with AuNPs with different CB5 concentrations. CB5 binds to AuNP surfaces through carboxylate groups on the molecule, so fixed interparticle distances could be achieved.⁶⁸ A transition from RL to DL kinetics with increasing CB5 concentrations was measured. RL showed a linear increase in integrated extinction over time whereas DL changed abruptly after about 10 minutes. The DL change is attributed to the presence of two mechanisms: the immediate formation of NC dimers followed by chain-like multiparticle growth.⁶⁸ When the AuNPs were coupled, the plasmon band at 525 nm decreased and broadened but a secondary band centered around 650 nm appeared, indicating aggregation.⁶⁸ Cobbe *et al.* coupled AuNPs through streptavidin and DNA mediated interactions and controlled the aggregation kinetics by taking advantage of the RL and DL kinetic regimes. The nanocrystal concentration and the salt concentration were independently varied to control the rate of aggregation.⁸⁸ Increases in particle or salt concentration led to an increased growth rate. By measuring the change in the hydrodynamic diameter over time, a power law dependence of the aggregation size on time was observed.

The aggregation of gold, silica and polystyrene particles were theoretically and experimentally studied to investigate the universality of the two kinetic regimes in colloid chemistry.⁹³ For AuNPs (7.5 nm), aggregation was induced through ligand exchange with neutrally

charged pyridine. The reduction in electrostatic charge destabilized the particles and induced aggregation with the creation of metallic bonds between particles. The aggregation rate was controlled by the concentration of pyridine. Aggregation was induced in colloidal silica (3.5 nm) by increasing the ionic strength in basic conditions to create siloxane bonds upon aggregation. Polystyrene latex (19 nm) were initially stabilized by carboxylic acid groups. The interparticle screening was decreased by the addition of HCl to induce aggregation. These aggregates were measured using TEM and light scattering techniques to compare the kinetic behavior of the particles. It was concluded that the RL and DL kinetic regimes are independent of the chemical nature of NCs.⁹³

The kinetics of irreversible agglomeration of NCs was investigated and was also found to follow a RL and DL process. In RL aggregation, the stability of NCs is temperature dependent because the aggregation rate is dependent on overcoming the potential barrier of the electrostatic interactions between ligands. RL aggregation kinetics followed an exponential dependence. DL aggregation is temperature independent and followed a power law.³⁹

The degree and rate of ligand induced self-assembly has been investigated using *p*-aminothiophenol as the molecular linker for citrate capped AuNPs.⁶⁹ Assembly was induced when the mercapto and amino groups on the *p*-aminothiophenol attached to different AuNPs. The linearly coupled AuNPs displayed a secondary plasmonic peak that arose due to the plasmonic coupling between the NCs.⁶⁹ The rate of self-assembly was tuned through linker concentration added to an ensemble of AuNPs. The assembly rate decreased with increasing linker concentration at higher concentrations but increasing concentration increased the rate at lower linker concentrations.⁶⁹ This was attributed to the electrostatic interactions that were available at different ligand concentrations; through zeta-potential measurements, the favorable conditions for assembly

was measured at $\zeta < 35$ mV.⁶⁹ Changing the linker concentration influenced the rate of assembly to a greater degree than changing the pH. It was suggested that the AuNPs underwent surface chemical modifications after assembly as indicated by a decreased zeta potential without a decrease in UV-vis peak intensities that indicate assembly.⁶⁹

Compared to chemical reactions, the kinetic equilibrium constant of self-assembly systems involving NCs is larger. For example, the kinetics of DNA hybridization for a fully complementary 15mer sequence was measured with Langmuir kinetics.⁹⁴ The rate constants for association and dissociation were $1.8 \times 10^4 \text{ M}^{-1}\text{s}^{-1}$ and $1.3 \times 10^{-5} \text{ s}^{-1}$, respectively, with $K = 14 \times 10^8 \text{ M}^{-1}$.⁹⁴ The self-assembly of proteins onto NC surfaces was on the order of $10^8 \times 10^9 \text{ M}^{-1}$.⁹⁵ Since the kinetic constants are the ratio of the associated kinetic constant and dissociative kinetic constant, NC assembly has a stronger association than the DNA duplex in solution.

1.4.1.2 DNA-Mediated Assembly

DNA is a unique tool to rationally design various assembled structures with NCs as the building blocks.^{64,66,67,78,80,88,96-99} Advances in nucleic acid synthetic methods allow for specific base pair (bp) sequence engineering and the incorporation of functional groups on the oligonucleotides for NC coupling. The assembly of oligonucleotides into DNA duplexes is highly specific through Watson-Crick base pairing, allowing for a high degree of control, predictability and precision of the resulting nanoarchitectures. NC surfaces are also able to support a large number of DNA strands, typically between 1 and 300 DNA per NC, depending on the synthetic parameters, NC size, the length and chemical composition of the spacer between the NC surface and the oligonucleotide, and DNA strand length and sequence.⁹⁸⁻¹⁰¹ DNA linked materials have been built for optical and electrical detection of analytes, siRNA delivery or to create crystalline

structures from NCs.^{78,98,102,103} The studies involved in DNA based programming aim to engineer the building blocks and the final assembled structures.^{78,80,99} In DNA-programmable NC crystallization, different DNA sequences directed the assembly of AuNPs into different crystal structures.⁷⁸ When linked to particles, the DNA properties, including thermal melting transitions (T_m), differ from free DNA in solution.⁹⁸ The properties of the DNA linked materials are dependent on the polyelectrolytic and base pair hybridization of the duplexes.⁹⁸ The assembly of DNA coated colloids can either be kinetically or thermodynamically controlled.⁷⁸ To achieve the thermodynamic product, the DNA oligonucleotides are combined above their T_m and then slowly cooled to room temperature.⁷⁸ Park *et. al.* found that when two oligonucleotide coated AuNP particles were combined thermodynamically above the T_m , the AuNPs formed a disordered face centered cubic (f.c.c) crystal that increases the entropy of the entire system by creating the smallest volume of the crystal.⁷⁸ However, when the AuNP colloids were hybridized to form the kinetically favored product at room temperature, the AuNPs formed a non-close packed body centered cubic (b.c.c) crystalline material, which maximized DNA binding events.⁷⁸ These and other studies have shown that the product that is formed during DNA mediated assembly can be controlled through assembly temperature, DNA rigidity, DNA length, valency and particle size.^{78,80} General methods of DNA programmable equivalents have been developed to create DNA functionalized building blocks regardless of the colloid material.⁹⁹

1.4.2 Resonance Energy Transfer

The self-assembly of NC clusters leads to synergistic properties including non-radiative energy transfer between fluorescent particles. In QD excitation, light is used to create a forced oscillation of dipoles. In a forced oscillation, the amplitude of the oscillation in a system is at a

maximum when the frequency of an external force equals the natural frequency of a system, which is called the resonance frequency.

Coupled nanomaterials can participate in a variety of different energy transfer processes for a wide variety of applications related to chemical sensing, biological imaging and quantum computing. The energy transfer that occurs depends on the optical properties of the individual components, allowed electronic transition and intermolecular separation. For example, fluorophores that are in close proximity ($d = 1-10$ nm) can transfer energy non-radiatively from an excited donor to a ground state acceptor through Förster resonance energy transfer (FRET)^{25,104,105} or nanometal surface energy transfer (NSET).⁸³ If the wavefunction of donor and acceptor overlap and they have a smaller intermolecular separation ($d < 2$ nm), Dexter energy transfer (DET) can occur.^{79,106} These processes have a different dependence on the intermolecular separation and strength of dipole coupling. NSET has an inverse fourth intermolecular separation dependency, whereas FRET has an inverse sixth dependency on component separation; this causes NSET to undergo more efficient energy transfer than FRET. Because of the strong distance dependence, FRET and NSET can be used as optical rulers. Energy transfer can also occur with bioluminescent donors in bioluminescence resonance energy transfer (BRET)^{81,82,107-115} or with chemiluminescent donors in chemiluminescence resonance energy transfer (CRET).¹¹⁶

The nanomaterials that undergo these processes must be at very short distances, typically under 10 nm. A donor and acceptor can be brought into close proximity through coupling mechanisms, including DNA mediated interactions or organic coupling reactions such as click chemistry. These systems are very sensitive and a large degree of control over the energy transfer can be obtained.

1.4.2.1 Förster Resonance Energy Transfer

In FRET, energy is transferred from an excited fluorescent donor to a ground state acceptor that emits a lower energy photon. FRET processes occur from long range coulombic dipole-dipole interactions between a donor and acceptor in close proximity.²⁵ FRET does not involve the emission and reabsorption of photons. Instead, FRET assumes the fluorophore acts as an oscillating dipole that can exchange energy with another dipole with a similar oscillating frequency.²⁵ Figure 1.7 shows a summary of the electronic and spectral changes that occur as a result of the energy transfer process between a donor and acceptor pair.

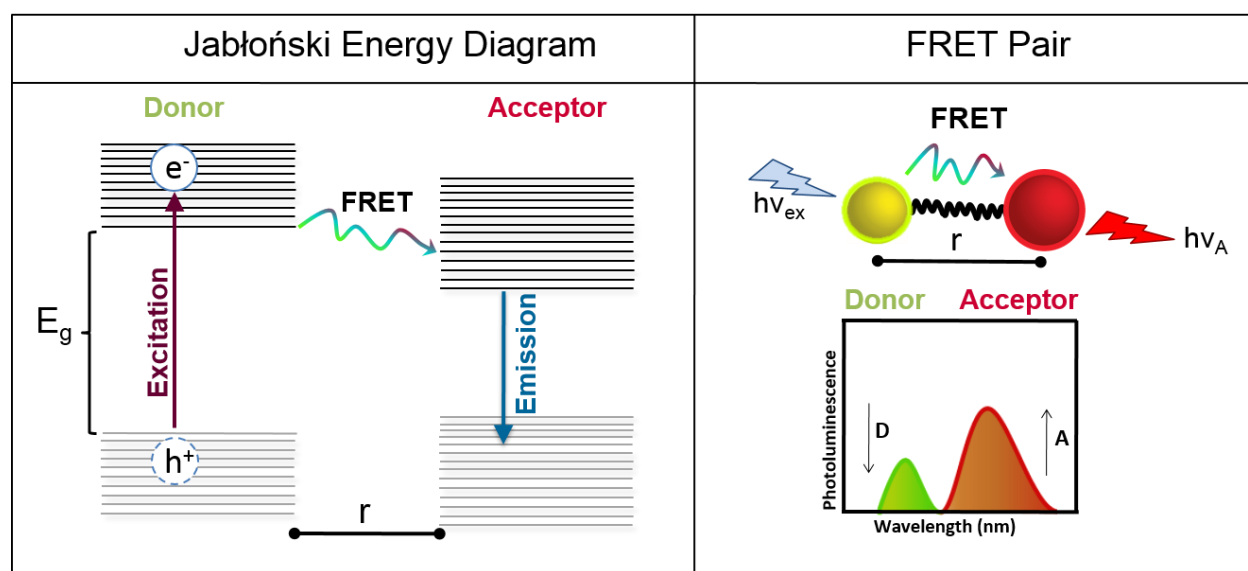


Figure 1.7: Jablonski energy diagram illustrating the electronic changes during the FRET process and a donor acceptor pair and resulting spectral change from energy transfer.

These processes are dependent on the degree of spectral overlap, donor and acceptor distance and orientation, the acceptor extinction coefficient, and donor quantum yield (QY). FRET usually occurs between molecules that are separated by a distance of 10 nm or less, so there is an intrinsic sensitivity to nanometer changes in intermolecular distance and changes in dipole orientations. The rate of energy transfer is given in Equation 1.6.^{25,104,105}

$$k_T = \frac{1}{\tau_D} \left(\frac{R_0}{r} \right)^6 \quad (1.6)$$

Where τ_D is the donor decay time in the absence of the acceptor, r is the distance between the donor and acceptor and R_0 is the Förster distance, a parameter that is calculated from the spectral overlap and dipole orientations as shown in Equation 1.7.^{25,104,105}

$$R_0 = 9.78 \times 10^2 [\kappa^2 \eta_D^{-4} Q_D J(\lambda)]^{1/6} \quad (1.7)$$

Where κ is the orientation factor ($\kappa = 2/3$), η_D is the refractive index of the medium, Q_D is the quantum yield of the donor and $J(\lambda)$ is the overlap integral at wavelength (λ). The probability of energy transfer is quantified using the overlap integral, J , which describes the degree of spectral overlap between the donor PL spectrum and the acceptor absorbance spectrum, as shown in Equation 1.8.^{25,104,105}

$$J(\lambda) = \int_0^{\infty} F_D(\lambda) \varepsilon_A(\lambda)^4 d\lambda \quad (1.8)$$

The FRET efficiency, E , describes the fraction of non-radiative energy transferred from the donor to the acceptor and is defined in Equation 1.9.^{25,104,105}

$$E = \frac{R_0^6}{R_0^6 + r^6} = 1 - \frac{F_{DA}}{F_D} \quad (1.9)$$

Where F_D and F_{DA} is the fluorescence intensity of the donor in the absence and presence of the acceptor, respectively.²⁵ The FRET efficiency can be measured through steady state and time resolved fluorescence spectroscopy. Evidence for FRET includes donor emission quenching shortened exciton lifetime that is concurrent with photoluminescence enhancement and increased exciton lifetime for a fluorescent acceptor.^{25,105}

QDs are ideal FRET donors due to their high QYs, large extinction coefficients, narrow emission peaks and high photobleaching thresholds.^{105,117} The larger sizes of QDs relative to

organic fluorophores allow systems to be configured with different donor-acceptor stoichiometries for multiplexing capabilities. Since the fluorescence emission of QDs can be spectrally tuned, QDs can act as both donors and acceptors depending on the relative emission wavelengths. One limitation to QDs in FRET applications includes their large absorption cross-section that allows them to be excited at multiple wavelengths. This makes it more complicated to prevent direct acceptor excitation.

A variety of mechanisms can inhibit the energy transfer between two particles. If non-radiative pathways show up after dipole coupling, FRET efficiency can decrease. There can be intersystem energy transfer if two FRET pairs come into close enough contact in solution. Interactions with the solvent can also create non-radiative pathways. If there is any fluctuation in donor and acceptor distances, then the FRET efficiency will be more difficult to measure.

1.4.2.2 Bioluminescence Resonance Energy Transfer

When the energy donor is a bioluminescent species, the energy transfer is known as bioluminescence resonance energy transfer (BRET). Many species have independently evolved to be bioluminescent, including bacteria, coelenterates, and beetles,¹¹⁸ but the North American firefly, *Photinus pyralis* (Ppy), is believed to have the most efficient bioluminescence with quantum yields (QY) around 30%.¹⁰⁷ Although the genes that are responsible for bioluminescence are unrelated between the different species, they all involve the reaction of molecular oxygen with a substrate, luciferin, and enzymes, luciferase, to produce photons.¹¹⁸ Figure 1.8 shows the mechanism of the bioluminescence for Ppy.^{119–123}

these conjugates can be used to prevent simultaneous excitation of the donor and acceptor for compounds that have broad absorption spectra, including QDs and QRs.

1.4.3 Encoded Nanocarriers

Ligand-mediated assembly has also been used to couple NCs with drug molecules.^{96,125,126} Assembled nanoconjugates can function as therapeutic agents that can overcome current limitations in drug therapies, such as low water solubility, low targeting ability and cell drug resistance.^{96,125–135} Current chemotherapeutic moieties are administered with no target selectivity and high collateral damage that leads to lower quality of life for the patient.¹³³ Current research is devoted to improving the drug delivery and efficacy by creating nanoconjugates that are stable, provide site-specific delivery and programmed release of drugs, and can be cleared by the body to reduce cytotoxic effects.^{130,131} Metal NCs, such as AuNPs and iron oxide nanoparticles (FeNPs) are promising candidates for drug delivery applications due to their high surface to volume ratio, tunable surface chemistries, low cytotoxicities, cellular uptake abilities and magnetic capabilities.^{127,130} The surface of NCs have been modified with a variety of ligands, including folic acid,¹²⁶ thermoresponsive polymers,^{96,135} and peptides¹³⁶ to increase the cell targeting potential and cellular toxicity.¹²⁶ It has been shown that NCs can be internalized in cells through endocytosis.¹³⁰ The NC surface chemistry can affect cellular uptake ability, intracellular localization or cellular response.¹³⁰ There are many promising NC conjugates for drug delivery in the literature, including the electrostatic assembly of NC-drug conjugates,¹³⁴ covalent attachment of drugs to NC surfaces,¹²⁷ the entrapment of drug in NC cages,¹³⁵ and the intercalation of drug in DNA functionalized NPs.^{125,126,128} Oligonucleotide degradation has been a major challenge for nucleic acid based drug delivery. DNA modified AuNP conjugates have been found to overcome this

limitation by resisting enzyme degradation due to the high local ion concentration on the densely packed DNA that inhibits enzyme activity.¹³⁰

1.4.3.1 Drug Release Kinetics

The kinetics of drug release in nanoconjugates created for drug delivery is important for determining the strength of the drug binding and rate of release.^{96,125,137} This is typically measured using a dynamic dialysis method, where the nanoconjugate is loaded into a dialysis membrane and the appearance of drug outside of the membrane is measured.^{96,125,137}

The chemical equation for the creation of the drug complex, which is the drug bound to the nanoconjugate is found in Equation 1.10.



where k_a and k_d are the reaction rate constants for the association and dissociation of the drug complex, respectively. The rate of the reaction is expressed as shown in Equation 1.11:

$$rate = k_a [drug][site] = k_d [complex] \quad (1.11)$$

where [drug], [site] and [complex] are expressed in molar concentrations. The rate of drug release is then expressed as the rate for the reverse reaction. Drug release is typically assumed to be a first order reaction that follows the exponential in Equation 1.12.^{96,125,137}

$$y = \alpha(1 - e^{-\beta t}) \quad (1.12)$$

Where α is the percent drug released after equilibrium, β is the rate of drug release after equilibrium, and t is the time of drug release.¹⁸ The equilibrium binding constant, K_{eq} , can then be calculated using Equation 1.13.

$$K_{eq} = \frac{k_d}{k_a} = \frac{[Complex]}{[drug][site]} \quad (1.13)$$

where [IDA], [site] and [Complex] are the molar concentrations at equilibrium and k_a and k_d are the association and dissociation rate constants, respectively. Typical K_{eq} values are on the order of 10^2 - 10^7 for NC drug conjugates.^{128,137}

1.5 NC Characterization

The metal and semiconductor NCs described in this thesis were characterized using a variety of methods, including spectroscopic and microscopic techniques.

The photophysical properties and NC concentrations were measured using UV-Vis spectroscopy and photoluminescence spectroscopy (PL). These techniques measure the electronic changes associated with the absorption and emission of light. In UV-Vis, the extinction coefficient is an important parameter that measures how strongly a chemical species absorbs light at a given wavelength. Since various materials absorb light to different extents, the extinction coefficient is characteristic of the material and is related to particle size, composition, oscillator strength, absorption cross-section, light scattering from the particle surface and dielectric environment.^{2,6,15} The Beer-Lambert Law is employed to determine extinction coefficients and concentrations as shown in Equation 1.14.

$$\log \frac{I_0}{I} = A = \epsilon c L \quad (1.14)$$

Where I_0 and I are the intensity of light before and after hitting the sample, respectively, A is the absorbance of the sample at a given wavelength, c is the concentration of the sample and L is the path length (cm) of radiation that goes through the sample. There are limitations to the Beer-Lambert law including, but not limited to: stray light, polychromatic radiation, high optical density, and chemical change of analyte.²⁵ The concentration limit for colloids is smaller than for smaller molecules, which deviate at concentrations above 0.01 M because of their large size.¹³⁸ In NC

optical studies, NCs can be instable at the linear portion of the Beer's Law plot from dilute conditions and the small errors on the size will generate large errors in the calculation of the extinction coefficient due to the power dependence between volume and extinction coefficient.¹⁴ Size dispersion also has an effect so a correction using half width at half maximum for either the absorption or emission spectra is sometimes applied.^{139,140}

Various groups have experimentally determined the extinction coefficients of AuNPs and QDs and QRs. The absorption arises from different effects in AuNPs compared to QDs and QRs. For AuNPs, UV-Vis spectra arise from surface plasmon resonance. The experimentally determined extinction coefficient for AuNPs smaller than 85 nm is found in Equation 1.15.¹⁴¹⁻¹⁴⁵

$$\epsilon = 4.7 \times 10^4 d^{3.3} \quad (1.15)$$

Where ϵ is at the SPR peak ($\lambda=520$ nm), d is the diameter of the AuNP in nm. For spherical CdSe QDs, the extinction coefficient is dependent on diameter, as shown in Equation 1.16.¹⁴⁰

$$\epsilon = 5857 d^{2.65} \quad (1.16)$$

Where ϵ is at the first absorption peak, the diameter (d) is in nm and measured using TEM or the first absorption peak. The relationship between the first absorption peak and QD diameter is found in Equation 1.17.¹⁴⁰

$$d = (1.6122 \times 10^{-9}) \lambda^4 - (2.6575 \times 10^{-6}) \lambda^3 + (1.6242 \times 10^{-3}) \lambda^2 - 0.4277 \lambda + 4157 \quad (1.17)$$

Where d is the QD diameter in nm and λ is the wavelength of the first absorption peak.¹⁴⁰

For anisotropic CdSe QR cores, the extinction coefficient is found in Equation 1.18.¹⁴⁶

$$\epsilon = 0.38 \times 10^{26} V \quad (1.18)$$

Where ϵ is at $\lambda=350$ nm, V is the volume of the QR in cm^3 , which can be measured using TEM.

Other optical techniques that were used to characterize nanomaterials are dynamic light scattering, fluorescence polarization and confocal microscopy. The size and shape of NCs can be

determined using microscopic techniques including transmission electron microscopy (TEM) and atomic force microscopy (AFM).

1.6 Research

This thesis focuses on the preparation of AuNPs, QDs and QRs to create useful materials for self-assembly and energy transfer applications. In Chapter 2, hydrophobic CdSe/ZnS QDs were synthesized and encapsulated in an amphiphilic polymer to create hydrophilic QD polymer conjugates. The outer polymer shell was further functionalized with oligonucleotides through EDC/NHS coupling and click chemistry to create QD/DNA conjugates. QD/DNA with different emission wavelengths were then self-assembled on a magnetic colloidal support using DNA mediated interactions and the QD to QD energy transfer within these clusters was observed. In Chapter 3, CdSe/CdS QRs were synthesized and phase transferred using a histidine mediated phase transfer protocol. The QRs underwent further ligand exchange with hexahistidine tagged green emitting variant of firefly luciferase from *Photinus pyralis* (Ppy). The BRET was measured in the QR/Ppy conjugates, where Ppy molecules were energy donors and QRs were energy acceptors. The long-term stability of these conjugates was improved to make their incorporation into new technologies a more viable option. In Chapter 4, AuNPs were synthesized and functionalized with DNA duplexes that have a high affinity for the clinically approved chemotherapeutic drug idarubicin (IDA). The effect of drug loading on the duplex melting temperature was measured. A thermoresponsive polymer was also incorporated into this system and the drug release kinetics was measured to compare the effect of the polymer on drug release.

1.7 References

- (1) Yin, Y.; Alivisatos, A. P. Colloidal Nanocrystal Synthesis and the Organic–inorganic Interface. *Nature* **2005**, *437* (7059), 664–670.
- (2) Gong, K.; Zeng, Y.; Kelley, D. F. Extinction Coefficients, Oscillator Strengths, and Radiative Lifetimes of CdSe, CdTe, and CdTe/CdSe Nanocrystals. *J. Phys. Chem. C* **2013**, *117* (39), 20268–20279.
- (3) Liu, X.; Atwater, M.; Wang, J.; Huo, Q. Extinction Coefficient of Gold Nanoparticles with Different Sizes and Different Capping Ligands. *Colloids Surf. B Biointerfaces* **2007**, *58* (1), 3–7.
- (4) Rance, G. A.; Marsh, D. H.; Khlobystov, A. N. Extinction Coefficient Analysis of Small Alkanethiolate-Stabilised Gold Nanoparticles. *Chem. Phys. Lett.* **2008**, *460* (1-3), 230–236.
- (5) Maye, M. M.; Han, L.; Kariuki, N. N.; Ly, N. K.; Chan, W.-B.; Luo, J.; Zhong, C.-J. Gold and Alloy Nanoparticles in Solution and Thin Film Assembly: Spectrophotometric Determination of Molar Absorptivity. *Anal. Chim. Acta* **2003**, *496* (1-2), 17–27.
- (6) Kelly, K. L.; Coronado, E.; Zhao, L. L.; Schatz, G. C. The Optical Properties of Metal Nanoparticles: The Influence of Size, Shape, and Dielectric Environment. *J. Phys. Chem. B* **2003**, *107* (3), 668–677.
- (7) Burda, C.; Chen, X.; Narayanan, R.; El-Sayed, M. A. Chemistry and Properties of Nanocrystals of Different Shapes. *Chem. Rev.* **2005**, *105* (4), 1025–1102.
- (8) Daniel, M. C.; Astruc, D. Gold Nanoparticles: Assembly, Supramolecular Chemistry, Quantum-Size-Related Properties, and Applications toward Biology, Catalysis, and Nanotechnology. *Chem. Rev.* **2004**, *104* (1), 293–346.
- (9) Zhou, F.; Li, Z.-Y.; Liu, Y.; Xia, Y. Quantitative Analysis of Dipole and Quadrupole Excitation in the Surface Plasmon Resonance of Metal Nanoparticles. *J. Phys. Chem. C* **2008**, *112* (51), 20233–20240.
- (10) Moores, A.; Goettmann, F. The Plasmon Band in Noble Metal Nanoparticles: An Introduction to Theory and Applications. *New J. Chem.* **2006**, *30* (8), 1121.
- (11) Schasfoort, R. B. M.; Tudos, A. J. *Handbook of Surface Plasmon Resonance*; Royal Society of Chemistry, 2008.
- (12) Norris, D. J.; Bawendi, M. G. Measurement and Assignment of the Size-Dependent Optical Spectrum in CdSe Quantum Dots. *Phys. Rev. B* **1996**, *53* (24), 16338.
- (13) Krahne, R.; Morello, G.; Figuerola, A.; George, C.; Deka, S.; Manna, L. Physical Properties of Elongated Inorganic Nanoparticles. *Phys. Rep.* **2011**, *501* (3-5), 75–221.
- (14) Cademartiri, L.; Montanari, E.; Calestani, G.; Migliori, A.; Guagliardi, A.; Ozin, G. A. Size-Dependent Extinction Coefficients of PbS Quantum Dots. *J. Am. Chem. Soc.* **2006**, *128* (31), 10337–10346.
- (15) Leatherdale, C. A.; Woo, W.-K.; Mikulec, F. V.; Bawendi, M. G. On the Absorption Cross Section of CdSe Nanocrystal Quantum Dots. *J. Phys. Chem. B* **2002**, *106* (31), 7619–7622.
- (16) Hu, J.; Li, L.; Yang, W.; Manna, L.; Wang, L.; Alivisatos, A. P. Linearly Polarized Emission from Colloidal Semiconductor Quantum Rods. *Science* **2001**, *292* (5524), 2060–2063.
- (17) Scholes, G. D. Controlling the Optical Properties of Inorganic Nanoparticles. *Adv. Funct. Mater.* **2008**, *18* (8), 1157–1172.
- (18) Mulvaney, P. Surface Plasmon Spectroscopy of Nanosized Metal Particles. *Langmuir* **1996**, *12* (3), 788–800.
- (19) Huang, X.; El-Sayed, M. A. Gold Nanoparticles: Optical Properties and Implementations in Cancer Diagnosis and Photothermal Therapy. *J. Adv. Res.* **2010**, *1* (1), 13–28.

- (20) Navarro, J. R. G.; Werts, M. H. V. Resonant Light Scattering Spectroscopy of Gold, Silver and Gold–silver Alloy Nanoparticles and Optical Detection in Microfluidic Channels. *The Analyst* **2013**, *138* (2), 583–592.
- (21) Muskens, O. L.; Bachelier, G.; Fatti, N. D.; Vallée, F.; Brioude, A.; Jiang, X.; Pileni, M.-P. Quantitative Absorption Spectroscopy of a Single Gold Nanorod. *J. Phys. Chem. C* **2008**, *112* (24), 8917–8921.
- (22) Brus, L. Electronic Wave Functions in Semiconductor Clusters: Experiment and Theory. *J. Phys. Chem.* **1986**, *90* (12), 2555–2560.
- (23) Donegá, C. de M. Synthesis and Properties of Colloidal Heteronanocrystals. *Chem. Soc. Rev.* **2011**, *40* (3), 1512–1546.
- (24) Karel Čapek, R.; Moreels, I.; Lambert, K.; De Muynck, D.; Zhao, Q.; Van Tomme, A.; Vanhaecke, F.; Hens, Z. Optical Properties of Zincblende Cadmium Selenide Quantum Dots. *J. Phys. Chem. C* **2010**, *114* (14), 6371–6376.
- (25) Lakowicz, J. *Principles of Fluorescence Spectroscopy*, Second.; Kluwer Academic/Plenum Publishers: New York, NY, 1999.
- (26) De Mello Donegá, C.; Koole, R. Size Dependence of the Spontaneous Emission Rate and Absorption Cross Section of CdSe and CdTe Quantum Dots. *J. Phys. Chem. C* **2009**, *113* (16), 6511–6520.
- (27) Sitt, A.; Salant, A.; Menagen, G.; Banin, U. Highly Emissive Nano Rod-in-Rod Heterostructures with Strong Linear Polarization. *Nano Lett.* **2011**, *11* (5), 2054–2060.
- (28) Hadar, I.; Hitin, G. B.; Sitt, A.; Faust, A.; Banin, U. Polarization Properties of Semiconductor Nanorod Heterostructures: From Single Particles to the Ensemble. *J. Phys. Chem. Lett.* **2013**, *4* (3), 502–507.
- (29) Peng, X. An Essay on Synthetic Chemistry of Colloidal Nanocrystals. *Nano Res.* **2010**, *2* (6), 425–447.
- (30) Liu, H.; Owen, J. S.; Alivisatos, A. P. Mechanistic Study of Precursor Evolution in Colloidal Group II–VI Semiconductor Nanocrystal Synthesis. *J. Am. Chem. Soc.* **2007**, *129* (2), 305–312.
- (31) Murphy, C. J.; Coffey, J. L. Quantum Dots: A Primer. *Appl. Spectrosc.* **2002**, *56* (1), 16A – 27A.
- (32) Xia, Y.; Xiong, Y.; Lim, B.; Skrabalak, S. E. Shape-Controlled Synthesis of Metal Nanocrystals: Simple Chemistry Meets Complex Physics? *Angew. Chem. Int. Ed.* **2009**, *48* (1), 60–103.
- (33) Ali, M. R. K.; Snyder, B.; El-Sayed, M. A. Synthesis and Optical Properties of Small Au Nanorods Using a Seedless Growth Technique. *Langmuir* **2012**, *28* (25), 9807–9815.
- (34) Straney, P. J.; Andolina, C. M.; Millstone, J. E. Seedless Initiation as an Efficient, Sustainable Route to Anisotropic Gold Nanoparticles. *Langmuir* **2013**, *29* (13), 4396–4403.
- (35) Knowles, K. E.; Frederick, M. T.; Tice, D. B.; Morris-Cohen, A. J.; Weiss, E. A. Colloidal Quantum Dots: Think Outside the (Particle-in-a-)Box. *J. Phys. Chem. Lett.* **2012**, *3* (1), 18–26.
- (36) Caragheorghopol, A.; Chechik, V. Mechanistic Aspects of Ligand Exchange in Au Nanoparticles. *Phys. Chem. Chem. Phys.* **2008**, *10* (33), 5029.
- (37) Pradhan, N.; Reifsnnyder, D.; Xie, R.; Aldana, J.; Peng, X. Surface Ligand Dynamics in Growth of Nanocrystals. *J. Am. Chem. Soc.* **2007**, *129* (30), 9500–9509.

- (38) Puzder, A.; Williamson, A. J.; Zaitseva, N.; Galli, G.; Manna, L.; Alivisatos, A. P. The Effect of Organic Ligand Binding on the Growth of CdSe Nanoparticles Probed by Ab Initio Calculations. *Nano Lett.* **2004**, *4* (12), 2361–2365.
- (39) Born, P.; Kraus, T. Ligand-Dominated Temperature Dependence of Agglomeration Kinetics and Morphology in Alkyl-Thiol-Coated Gold Nanoparticles. *Phys. Rev. E* **2013**, *87* (6).
- (40) Qu, L.; Peng, X. Control of Photoluminescence Properties of CdSe Nanocrystals in Growth. *J. Am. Chem. Soc.* **2002**, *124* (9), 2049–2055.
- (41) Häkkinen, H. The Gold-Sulfur Interface at the Nanoscale. *Nat. Chem.* **2012**, *4* (6), 443–455.
- (42) Moreels, I.; Justo, Y.; De Geyter, B.; Haestraete, K.; Martins, J. C.; Hens, Z. Size-Tunable, Bright, and Stable PbS Quantum Dots: A Surface Chemistry Study. *ACS Nano* **2011**, *5* (3), 2004–2012.
- (43) Ji, X.; Copenhaver, D.; Sichmeller, C.; Peng, X. Ligand Bonding and Dynamics on Colloidal Nanocrystals at Room Temperature: The Case of Alkylamines on CdSe Nanocrystals. *J. Am. Chem. Soc.* **2008**, *130* (17), 5726–5735.
- (44) Bullen, C.; Mulvaney, P. The Effects of Chemisorption on the Luminescence of CdSe Quantum Dots. *Langmuir* **2006**, *22* (7), 3007–3013.
- (45) Stewart, A.; Zheng, S.; McCourt, M. R.; Bell, S. E. J. Controlling Assembly of Mixed Thiol Monolayers on Silver Nanoparticles to Tune Their Surface Properties. *ACS Nano* **2012**, *6* (5), 3718–3726.
- (46) Cheng, H.; Yang, L.; Jiang, Y.; Huang, Y.; Sun, Z.; Zhang, J.; Hu, T.; Pan, Z.; Pan, G.; Yao, T.; Bian, Q.; Wei, S. Adsorption Kinetic Process of Thiol Ligands on Gold Nanocrystals. *Nanoscale* **2013**, *5* (23), 11795.
- (47) Coto-García, A. M.; Fernández-Argüelles, M. T.; Costa-Fernández, J. M.; Sanz-Medel, A.; Valledor, M.; Campo, J. C.; Ferrero, F. J. The Influence of Surface Coating on the Properties of Water-Soluble CdSe and CdSe/ZnS Quantum Dots. *J. Nanoparticle Res.* **2013**, *15* (1).
- (48) Tomczak, N.; Liu, R.; Vancso, J. G. Polymer-Coated Quantum Dots. *Nanoscale* **2013**, *5* (24), 12018–12032.
- (49) Anderson, R. E.; Chan, W. C. W. Systematic Investigation of Preparing Biocompatible, Single, and Small ZnS-Capped CdSe Quantum Dots with Amphiphilic Polymers. *ACS Nano* **2008**, *2* (7), 1341–1352.
- (50) Pellegrino, T.; Manna, L.; Kudera, S.; Liedl, T.; Koktysh, D.; Rogach, A. L.; Keller, S.; Rädler, J.; Natile, G.; Parak, W. J. Hydrophobic Nanocrystals Coated with an Amphiphilic Polymer Shell: A General Route to Water Soluble Nanocrystals. *Nano Lett.* **2004**, *4* (4), 703–707.
- (51) Lees, E. E.; Nguyen, T.-L.; Clayton, A. H. A.; Mulvaney, P. The Preparation of Colloidally Stable, Water-Soluble, Biocompatible, Semiconductor Nanocrystals with a Small Hydrodynamic Diameter. *ACS Nano* **2009**, *3* (5), 1121–1128.
- (52) Yu, W. W.; Chang, E.; Falkner, J. C.; Zhang, J.; Al-Somali, A. M.; Sayes, C. M.; Johns, J.; Drezek, R.; Colvin, V. L. Forming Biocompatible and Nonaggregated Nanocrystals in Water Using Amphiphilic Polymers. *J. Am. Chem. Soc.* **2007**, *129* (10), 2871–2879.
- (53) Zhang, F.; Lees, E.; Amin, F.; Rivera Gil, P.; Yang, F.; Mulvaney, P.; Parak, W. J. Polymer-Coated Nanoparticles: A Universal Tool for Biolabelling Experiments. *Small Weinheim, Bergstr. Ger.* **2011**, *7* (22), 3113–3127.
- (54) Sperling, R. A.; Parak, W. J. Surface Modification, Functionalization and Bioconjugation of Colloidal Inorganic Nanoparticles. *Philos. Trans. R. Soc. Math. Phys. Eng. Sci.* **2010**, *368* (1915), 1333–1383.

- (55) Lin, C.-A. J.; Sperling, R. A.; Li, J. K.; Yang, T.-Y.; Li, P.-Y.; Zanella, M.; Chang, W. H.; Parak, W. J. Design of an Amphiphilic Polymer for Nanoparticle Coating and Functionalization. *Small* **2008**, *4* (3), 334–341.
- (56) Jańczewski, D.; Tomczak, N.; Han, M.-Y.; Vancso, G. J. Synthesis of Functionalized Amphiphilic Polymers for Coating Quantum Dots. *Nat. Protoc.* **2011**, *6* (10), 1546–1553.
- (57) Palui, G.; Aldeek, F.; Wang, W.; Mattoussi, H. Strategies for Interfacing Inorganic Nanocrystals with Biological Systems Based on Polymer-Coating. *Chem. Soc. Rev.* **2014**, *44* (1), 193–227.
- (58) Harkness, K. M.; Hixson, B. C.; Fenn, L. S.; Turner, B. N.; Rape, A. C.; Simpson, C. A.; Huffman, B. J.; Okoli, T. C.; McLean, J. A.; Cliffel, D. E. A Structural Mass Spectrometry Strategy for the Relative Quantitation of Ligands on Mixed Monolayer-Protected Gold Nanoparticles. *Anal. Chem.* **2010**, *82* (22), 9268–9274.
- (59) Perumal, S.; Hofmann, A.; Scholz, N.; Rühl, E.; Graf, C. Kinetics Study of the Binding of Multivalent Ligands on Size-Selected Gold Nanoparticles. *Langmuir* **2011**, *27* (8), 4456–4464.
- (60) Guo, R.; Song, Y.; Wang, G.; Murray, R. W. Does Core Size Matter in the Kinetics of Ligand Exchanges of Monolayer-Protected Au Clusters? *J. Am. Chem. Soc.* **2005**, *127* (8), 2752–2757.
- (61) Spessard, G. O.; Miessler, G. L. *Organometallic Chemistry*; Oxford University Press, 2010.
- (62) Walsh, J. L.; Yancey, C. C. Acceleration of Ligand Exchange by Coordinated Nitrate in Polypyridyl Ruthenium Complexes. *Polyhedron* **1989**, *8* (9), 1223–1226.
- (63) Taube, H. Rates and Mechanisms of Substitution in Inorganic Complexes in Solution. *Chem. Rev.* **1952**, *50* (1), 69–126.
- (64) Di Michele, L.; Varrato, F.; Kotar, J.; Nathan, S. H.; Foffi, G.; Eiser, E. Multistep Kinetic Self-Assembly of DNA-Coated Colloids. *Nat. Commun.* **2013**, *4*.
- (65) Seker, U. O. S.; Zengin, G.; Tamerler, C.; Sarikaya, M.; Demir, H. V. Assembly Kinetics of Nanocrystals via Peptide Hybridization. *Langmuir* **2011**, *27* (8), 4867–4872.
- (66) Zhang, Y.; Lu, F.; Yager, K. G.; van der Lelie, D.; Gang, O. A General Strategy for the DNA-Mediated Self-Assembly of Functional Nanoparticles into Heterogeneous Systems. *Nat. Nanotechnol.* **2013**, *8* (11), 865–872.
- (67) Chhabra, R.; Sharma, J.; Liu, Y.; Rinker, S.; Yan, H. DNA Self-Assembly for Nanomedicine. *Adv. Drug Deliv. Rev.* **2010**, *62* (6), 617–625.
- (68) Taylor, R. W.; Lee, T.-C.; Scherman, O. A.; Esteban, R.; Aizpurua, J.; Huang, F. M.; Baumberg, J. J.; Mahajan, S. Precise Subnanometer Plasmonic Junctions for SERS within Gold Nanoparticle Assemblies Using Cucurbit[*n*]uril “Glue.” *ACS Nano* **2011**, *5* (5), 3878–3887.
- (69) Abbas, A.; Kattumenu, R.; Tian, L.; Singamaneni, S. Molecular Linker-Mediated Self-Assembly of Gold Nanoparticles: Understanding and Controlling the Dynamics. *Langmuir* **2013**, *29* (1), 56–64.
- (70) Sun, X.; Ding, K.; Hou, Y.; Gao, Z.; Yang, W.; Jing, L.; Gao, M. Bifunctional Superparticles Achieved by Assembling Fluorescent CuInS₂@ZnS Quantum Dots and Amphibious Fe₃O₄ Nanocrystals. *J. Phys. Chem. C* **2013**, *117* (40), 21014–21020.
- (71) Yusuf, H.; Kim, W.-G.; Lee, D. H.; Guo, Y.; Moffitt, M. G. Size Control of Mesoscale Aqueous Assemblies of Quantum Dots and Block Copolymers. *Langmuir* **2007**, *23* (2), 868–878.

- (72) Hawaldar, R. R.; Sathaye, S. D.; Harle, A.; Gholap, R. S.; Patil, K. R. Kinetics of PbCrO_4 Nanorod Growth by Oriented Attachment at the Air–Water Interface. *J. Phys. Chem. C* **2008**, *112* (20), 7557–7561.
- (73) Lattuada, M.; Furlan, M.; Harshe, Y. Field-Controlled Self-Assembly and Disassembly of Colloidal Nanoparticles. *Chim. Int. J. Chem.* **2011**, *65* (10), 792–798.
- (74) Ferdous, S.; Ioannidis, M. A.; Henneke, D. Adsorption Kinetics of Alkanethiol-Capped Gold Nanoparticles at the Hexane–water Interface. *J. Nanoparticle Res.* **2011**, *13* (12), 6579–6589.
- (75) Kutuzov, S.; He, J.; Tangirala, R.; Emrick, T.; Russell, T. P.; Böker, A. On the Kinetics of Nanoparticle Self-Assembly at Liquid/liquid Interfaces. *Phys. Chem. Chem. Phys.* **2007**, *9* (48), 6351–6358.
- (76) Mallavajula, R. K.; Archer, L. A. Nanocrystal Self-Assembly Assisted by Oriented Attachment. *Angew. Chem. Int. Ed.* **2011**, *50* (3), 578–580.
- (77) Grzelczak, M.; Vermant, J.; Furst, E. M.; Liz-Marzán, L. M. Directed Self-Assembly of Nanoparticles. *ACS Nano* **2010**, *4* (7), 3591–3605.
- (78) Park, S. Y.; Lytton-Jean, A. K. R.; Lee, B.; Weigand, S.; Schatz, G. C.; Mirkin, C. A. DNA-Programmable Nanoparticle Crystallization. *Nature* **2008**, *451* (7178), 553–556.
- (79) Nie, Z.; Petukhova, A.; Kumacheva, E. Properties and Emerging Applications of Self-Assembled Structures Made from Inorganic Nanoparticles. *Nat. Nanotechnol.* **2010**, *5* (1), 15–25.
- (80) Tikhomirov, G.; Hoogland, S.; Lee, P. E.; Fischer, A.; Sargent, E. H.; Kelley, S. O. DNA-Based Programming of Quantum Dot Valency, Self-Assembly and Luminescence. *Nat. Nanotechnol.* **2011**, *6* (8), 485–490.
- (81) Alam, R.; Zylstra, J.; Fontaine, D. M.; Branchini, B. R.; Maye, M. M. Novel Multistep BRET-FRET Energy Transfer Using Nanoconjugates of Firefly Proteins, Quantum Dots, and Red Fluorescent Proteins. *Nanoscale* **2013**, *5* (12), 5303–5306.
- (82) Alam, R.; Fontaine, D. M.; Branchini, B. R.; Maye, M. M. Designing Quantum Rods for Optimized Energy Transfer with Firefly Luciferase Enzymes. *Nano Lett.* **2012**, *12* (6), 3251–3256.
- (83) Han, H.; Valle, V.; Maye, M. M. Probing Resonance Energy Transfer and Inner Filter Effects in Quantum Dot–Large Metal Nanoparticle Clusters Using a DNA-Mediated Quench and Release Mechanism. *J. Phys. Chem. C* **2012**, *116* (43), 22996–23003.
- (84) Freeman, R.; Li, Y.; Tel-Vered, R.; Sharon, E.; Elbaz, J.; Willner, I. Self-Assembly of Supramolecular Aptamer Structures for Optical or Electrochemical Sensing. *The Analyst* **2009**, *134* (4), 653.
- (85) Van Oss, C. *Interfacial Forces in Aqueous Media, Second Edition*; CRC Press, 2006.
- (86) Lin, M. Y.; Lindsay, H. M.; Weitz, D. A.; Ball, R. C.; Klein, R.; Meakin, P. Universal Reaction-Limited Colloid Aggregation. *Phys. Rev. A* **1990**, *41* (4), 2005.
- (87) Meakin, P. Aggregation Kinetics. *Phys. Scr.* **1992**, *46* (4), 295.
- (88) Cobbe, S.; Connolly, S.; Ryan, D.; Nagle, L.; Eritja, R.; Fitzmaurice, D. DNA-Controlled Assembly of Protein-Modified Gold Nanocrystals. *J. Phys. Chem. B* **2003**, *107* (2), 470–477.
- (89) Kisak, E. T.; Kennedy, M. T.; Trommshauser, D.; Zasadzinski, J. A. Self-Limiting Aggregation by Controlled Ligand–Receptor Stoichiometry. *Langmuir* **2000**, *16* (6), 2825–2831.

- (90) Ziff, R. M.; McGrady, E. D.; Meakin, P. On the Validity of Smoluchowski's Equation for Cluster-cluster Aggregation Kinetics. *J. Chem. Phys.* **1985**, *82* (11), 5269–5274.
- (91) Kryven, I.; Lazzari, S.; Storti, G. Population Balance Modeling of Aggregation and Coalescence in Colloidal Systems. *Macromol. Theory Simul.* **2014**, *23* (3), 170–181.
- (92) Connolly, S.; Cobbe, S.; Fitzmaurice, D. Effects of Ligand-Receptor Geometry and Stoichiometry on Protein-Induced Aggregation of Biotin-Modified Colloidal Gold. *J. Phys. Chem. B* **2001**, *105* (11), 2222–2226.
- (93) Fullam, S.; Rao, S. N.; Fitzmaurice, D. Noncovalent Self-Assembly of Silver Nanocrystal Aggregates in Solution. *J. Phys. Chem. B* **2000**, *104* (26), 6164–6173.
- (94) Tawa, K.; Knoll, W. Mismatching Base-pair Dependence of the Kinetics of DNA-DNA Hybridization Studied by Surface Plasmon Fluorescence Spectroscopy. *Nucleic Acids Res.* **2004**, *32* (8), 2372–2377.
- (95) Aldeek, F.; Safi, M.; Zhan, N.; Palui, G.; Mattoussi, H. Understanding the Self-Assembly of Proteins onto Gold Nanoparticles and Quantum Dots Driven by Metal-Histidine Coordination. *ACS Nano* **2013**, *7* (11), 10197–10210.
- (96) Hamner, K. L.; Alexander, C. M.; Coopersmith, K.; Reishofer, D.; Provenza, C.; Maye, M. M. Using Temperature-Sensitive Smart Polymers to Regulate DNA-Mediated Nanoassembly and Encoded Nanocarrier Drug Release. *ACS Nano* **2013**, *7* (8), 7011–7020.
- (97) Maye, M. M.; Nykypanchuk, D.; van der Lelie, D.; Gang, O. A Simple Method for Kinetic Control of DNA-Induced Nanoparticle Assembly. *J. Am. Chem. Soc.* **2006**, *128* (43), 14020–14021.
- (98) Lee, O.-S.; Prytkova, T. R.; Schatz, G. C. Using DNA to Link Gold Nanoparticles, Polymers, and Molecules: A Theoretical Perspective. *J. Phys. Chem. Lett.* **2010**, *1* (12), 1781–1788.
- (99) Zhang, C.; Macfarlane, R. J.; Young, K. L.; Choi, C. H. J.; Hao, L.; Auyeung, E.; Liu, G.; Zhou, X.; Mirkin, C. A. A General Approach to DNA-Programmable Atom Equivalents. *Nat. Mater.* **2013**, *12* (8), 741–746.
- (100) Hurst, S. J.; Lytton-Jean, A. K. R.; Mirkin, C. A. Maximizing DNA Loading on a Range of Gold Nanoparticle Sizes. *Anal. Chem.* **2006**, *78* (24), 8313–8318.
- (101) Sun, D.; Gang, O. DNA-Functionalized Quantum Dots: Fabrication, Structural, and Physicochemical Properties. *Langmuir* **2013**, *29* (23), 7038–7046.
- (102) Nykypanchuk, D.; Maye, M. M.; van der Lelie, D.; Gang, O. DNA-Based Approach for Interparticle Interaction Control. *Langmuir* **2007**, *23* (11), 6305–6314.
- (103) Nykypanchuk, D.; Maye, M. M.; van der Lelie, D.; Gang, O. DNA-Guided Crystallization of Colloidal Nanoparticles. *Nature* **2008**, *451* (7178), 549–552.
- (104) Clegg, R. Fluorescence Resonance Energy Transfer. *Curr. Opin. Biotechnol.* **1995**, *6*, 103–110.
- (105) Clapp, A. R.; Medintz, I. L.; Mattoussi, H. Förster Resonance Energy Transfer Investigations Using Quantum-Dot Fluorophores. *ChemPhysChem* **2006**, *7* (1), 47–57.
- (106) So, M. C.; Wiederrecht, G. P.; Mondloch, J. E.; Hupp, J. T.; Farha, O. K. Metal-organic Framework Materials for Light-Harvesting and Energy Transfer. *Chem Commun* **2015**, *51* (17), 3501–3510.
- (107) Branchini, B. R.; Ablamsky, D. M.; Rosenman, J. M.; Uzasci, L.; Southworth, T. L.; Zimmer, M. Synergistic Mutations Produce Blue-Shifted Bioluminescence in Firefly Luciferase†. *Biochemistry (Mosc.)* **2007**, *46* (48), 13847–13855.

- (108) Branchini, B. R.; Ablamsky, D. M.; Rosenberg, J. C. Chemically Modified Firefly Luciferase Is an Efficient Source of Near-Infrared Light. *Bioconjug. Chem.* **2010**, *21* (11), 2023–2030.
- (109) So, M.-K.; Xu, C.; Loening, A. M.; Gambhir, S. S.; Rao, J. Self-Illuminating Quantum Dot Conjugates for in Vivo Imaging. *Nat. Biotechnol.* **2006**, *24* (3), 339–343.
- (110) Xu, X.; Soutto, M.; Xie, Q.; Servick, S.; Subramanian, C.; Arnim, A. G. von; Johnson, C. H. Imaging Protein Interactions with Bioluminescence Resonance Energy Transfer (BRET) in Plant and Mammalian Cells and Tissues. *Proc. Natl. Acad. Sci.* **2007**, *104* (24), 10264–10269.
- (111) Lee, J. O.; Lim, B.; Kim, Y.-P. Bioluminescence Resonance Energy Transfer Nanoprobes for Imaging. *IEEE J. Sel. Top. Quantum Electron.* **2014**, *20* (3), 57–66.
- (112) Pflieger, K. D. G.; Eidne, K. A. Illuminating Insights into Protein-Protein Interactions Using Bioluminescence Resonance Energy Transfer (BRET). *Nat. Methods* **2006**, *3* (3), 165–174.
- (113) De, A.; Gambhir, S. S. Noninvasive Imaging of Protein–protein Interactions from Live Cells and Living Subjects Using Bioluminescence Resonance Energy Transfer. *FASEB J.* **2005**, *19* (14), 2017–2019.
- (114) Hsu, C.-Y.; Chen, C.-W.; Yu, H.-P.; Lin, Y.-F.; Lai, P.-S. Bioluminescence Resonance Energy Transfer Using Luciferase-Immobilized Quantum Dots for Self-Illuminated Photodynamic Therapy. *Biomaterials* **2013**, *34* (4), 1204–1212.
- (115) Yao, H.; Zhang, Y.; Xiao, F.; Xia, Z.; Rao, J. Quantum Dot/bioluminescence Resonance Energy Transfer Based Highly Sensitive Detection of Proteases. *Angew. Chem. Int. Ed Engl.* **2007**, *46* (23), 4346–4349.
- (116) Huang, X.; Li, L.; Qian, H.; Dong, C.; Ren, J. A Resonance Energy Transfer between Chemiluminescent Donors and Luminescent Quantum-Dots as Acceptors (CRET). *Angew. Chem.* **2006**, *118* (31), 5264–5267.
- (117) Noor, M. O.; Petryayeva, E.; Tavares, A. J.; Uddayasankar, U.; Algar, W. R.; Krull, U. J. Building from the “Ground” Up: Developing Interfacial Chemistry for Solid-Phase Nucleic Acid Hybridization Assays Based on Quantum Dots and Fluorescence Resonance Energy Transfer. *Coord. Chem. Rev.* **2014**, *263–264*, 25–52.
- (118) Wilson, T.; Hastings, J. W. Bioluminescence. *Annu. Rev. Cell Dev. Biol.* **1998**, *14*, 197–230.
- (119) Yue, L.; Liu, Y.-J.; Fang, W.-H. Mechanistic Insight into the Chemiluminescent Decomposition of Firefly Dioxetanone. *J. Am. Chem. Soc.* **2012**, *134* (28), 11632–11639.
- (120) Marques, S. M.; Esteves da Silva, J. C. G. Firefly Bioluminescence: A Mechanistic Approach of Luciferase Catalyzed Reactions. *IUBMB Life* **2009**, *61* (1), 6–17.
- (121) Navizet, I.; Liu, Y.-J.; Ferré, N.; Roca-Sanjuán, D.; Lindh, R. The Chemistry of Bioluminescence: An Analysis of Chemical Functionalities. *Chemphyschem Eur. J. Chem. Phys. Phys. Chem.* **2011**, *12* (17), 3064–3076.
- (122) White, E. H.; Steinmetz, M. G.; Miano, J. D.; Wildes, P. D.; Morland, R. Chemi- and Bioluminescence of Firefly Luciferin. *J. Am. Chem. Soc.* **1980**, *102* (9), 3199–3208.
- (123) Pinto da Silva, L.; Esteves da Silva, J. C. G. Firefly Chemiluminescence and Bioluminescence: Efficient Generation of Excited States. *ChemPhysChem* **2012**, *13* (9), 2257–2262.
- (124) Hoffman, J. B.; Choi, H.; Kamat, P. V. Size-Dependent Energy Transfer Pathways in CdSe Quantum Dot–Squaraine Light-Harvesting Assemblies: Förster versus Dexter. *J. Phys. Chem. C* **2014**, *118* (32), 18453–18461.

- (125) Alexander, C. M.; Maye, M. M.; Dabrowiak, J. C. DNA-Capped Nanoparticles Designed for Doxorubicin Drug Delivery. *Chem. Commun.* **2011**, 47 (12), 3418–3420.
- (126) Alexander, C. M.; Hamner, K. L.; Maye, M. M.; Dabrowiak, J. C. Multifunctional DNA-Gold Nanoparticles for Targeted Doxorubicin Delivery. *Bioconjug. Chem.* **2014**, 25 (7), 1261–1271.
- (127) Hwu, J. R.; Lin, Y. S.; Josephrajan, T.; Hsu, M.-H.; Cheng, F.-Y.; Yeh, C.-S.; Su, W.-C.; Shieh, D.-B. Targeted Paclitaxel by Conjugation to Iron Oxide and Gold Nanoparticles. *J. Am. Chem. Soc.* **2009**, 131 (1), 66–68.
- (128) Alexander, C. M.; Dabrowiak, J. C.; Maye, M. M. Investigation of the Drug Binding Properties and Cytotoxicity of DNA-Capped Nanoparticles Designed as Delivery Vehicles for the Anticancer Agents Doxorubicin and Actinomycin D. *Bioconjug. Chem.* **2012**, 23 (10), 2061–2070.
- (129) Zhang, X.-Q.; Xu, X.; Lam, R.; Giljohann, D.; Ho, D.; Mirkin, C. A. Strategy for Increasing Drug Solubility and Efficacy through Covalent Attachment to Polyvalent DNA–Nanoparticle Conjugates. *ACS Nano* **2011**, 5 (9), 6962–6970.
- (130) Giljohann, D. A.; Seferos, D. S.; Daniel, W. L.; Massich, M. D.; Patel, P. C.; Mirkin, C. A. Gold Nanoparticles for Biology and Medicine. *Angew. Chem. Int. Ed.* **2010**, 49 (19), 3280–3294.
- (131) Choi, H. S.; Liu, W.; Liu, F.; Nasr, K.; Misra, P.; Bawendi, M. G.; Frangioni, J. V. Design Considerations for Tumour-Targeted Nanoparticles. *Nat. Nanotechnol.* **2010**, 5 (1), 42–47.
- (132) Paulo, C. S. O.; Pires das Neves, R.; Ferreira, L. S. Nanoparticles for Intracellular-Targeted Drug Delivery. *Nanotechnology* **2011**, 22 (49), 494002.
- (133) Ferrari, M. Cancer Nanotechnology: Opportunities and Challenges. *Nat. Rev. Cancer* **2005**, 5 (3), 161–171.
- (134) Zhang, G.; Shi, L.; Selke, M.; Wang, X. CdTe Quantum Dots with Daunorubicin Induce Apoptosis of Multidrug-Resistant Human Hepatoma HepG2/ADM Cells: In Vitro and in Vivo Evaluation. *Nanoscale Res. Lett.* **2011**, 6 (1), 418.
- (135) Yavuz, M. S.; Cheng, Y.; Chen, J.; Cogley, C. M.; Zhang, Q.; Rycenga, M.; Xie, J.; Kim, C.; Song, K. H.; Schwartz, A. G.; Wang, L. V.; Xia, Y. Gold Nanocages Covered by Smart Polymers for Controlled Release with near-Infrared Light. *Nat. Mater.* **2009**, 8 (12), 935–939.
- (136) De la Fuente, J. M.; Berry, C. C. Tat Peptide as an Efficient Molecule To Translocate Gold Nanoparticles into the Cell Nucleus. *Bioconjug. Chem.* **2005**, 16 (5), 1176–1180.
- (137) Modi, S.; Anderson, B. D. Determination of Drug Release Kinetics from Nanoparticles: Overcoming Pitfalls of the Dynamic Dialysis Method. *Mol. Pharm.* **2013**, 10 (8), 3076–3089.
- (138) Skoog, D. A.; Holler, F. J.; Crouch, S. R. *Principles of Instrumental Analysis*; Thomson Brooks/Cole, 2007.
- (139) Dai, Q.; Wang, Y.; Li, X.; Zhang, Y.; Pellegrino, D. J.; Zhao, M.; Zou, B.; Seo, J.; Wang, Y.; Yu, W. W. Size-Dependent Composition and Molar Extinction Coefficient of PbSe Semiconductor Nanocrystals. *ACS Nano* **2009**, 3 (6), 1518–1524.
- (140) Yu, W. W.; Qu, L.; Guo, W.; Peng, X. Experimental Determination of the Extinction Coefficient of CdTe, CdSe, and CdS Nanocrystals. *Chem. Mater.* **2003**, 15 (14), 2854–2860.
- (141) Link, S.; Wang, Z. L.; El-Sayed, M. A. Alloy Formation of Gold–Silver Nanoparticles and the Dependence of the Plasmon Absorption on Their Composition. *J. Phys. Chem. B* **1999**, 103 (18), 3529–3533.

- (142) Mulvaney, P.; Giersig, M.; Henglein, A. Electrochemistry of Multilayer Colloids: Preparation and Absorption Spectrum of Gold-Coated Silver Particles. *J. Phys. Chem.* **1993**, *97* (27), 7061–7064.
- (143) Jain, P. K.; Lee, K. S.; El-Sayed, I. H.; El-Sayed, M. A. Calculated Absorption and Scattering Properties of Gold Nanoparticles of Different Size, Shape, and Composition: Applications in Biological Imaging and Biomedicine. *J. Phys. Chem. B* **2006**, *110* (14), 7238–7248.
- (144) Haiss, W.; Thanh, N. T. K.; Aveyard, J.; Fernig, D. G. Determination of Size and Concentration of Gold Nanoparticles from UV–Vis Spectra. *Anal. Chem.* **2007**, *79* (11), 4215–4221.
- (145) Khlebtsov, N. G. Optics and Biophotonics of Nanoparticles with a Plasmon Resonance. *Quantum Electron.* **2008**, *38* (6), 504.
- (146) Shaviv, E.; Salant, A.; Banin, U. Size Dependence of Molar Absorption Coefficients of CdSe Semiconductor Quantum Rods. *ChemPhysChem* **2009**, *10* (7), 1028–1031.

Chapter 2

Probing the QD-QD Energy Transfer in Self-Assembled Quantum Dot Clusters

In this chapter, I describe the self-assembly of multi-color quantum dot (QD) clusters via a DNA-mediated stepwise approach. After QD assembly and disassembly at the solid support, the cluster's optical characteristics were measured using fluorescence spectroscopy. This technique obtained purified clusters that participated in fluorescence resonance energy transfer (FRET).

2.1 Introduction

Discrete nanocrystal (NC) components have been spontaneously assembled into higher ordered structures for a variety of applications in chemical or biological sensing,¹ fluorescence imaging,² plasmonics³ and nanomedicine.⁴⁻⁶ Oligonucleotides can be used as a soft template to direct NC self-assembly due to their inherent molecular recognition capabilities from sequence specific interactions.²⁻¹⁶ Interparticle spacing and geometry can be tuned by tailoring the DNA sequence, length and rigidity. This is important in energy transfer applications, because non-radiative energy transfer is highly dependent on interparticle distances, donor and acceptor ratios and relative nanoparticle sizes.^{12,17,18}

Although an abundance of research has focused on the self-assembly of DNA functionalized gold nanoparticles,^{8,10,19,20} quantum dots (QDs) can also be incorporated into self-assembled structures. QD surfaces can be modified with various ligands to impart them with different functionalities, allowing for a high degree of engineering flexibility.²¹ Interesting synergistic effects arise from coupled nanomaterials, including charge and energy transfer.¹⁷ In energy transfer applications, QD size dependent emission, long lifetimes and broad absorption spectra make them ideal energy transfer donors.^{12,18,22-28} The DNA mediated self-assembly of QDs

and fluorescent dyes has been used for the optical detection of analytes.¹⁸ In one study, oligonucleotides formed duplexes in the presence of a molecular target, which resulted in a FRET process between the QD and dye.¹⁸ When two QDs are coupled, long-range dipole-dipole interactions can lead to Förster resonance energy transfer (FRET).¹⁶ The same qualities that cause QDs to be efficient energy donors limits their use as energy acceptors. For example, their long lifetimes can decrease the chances of energy transfer due to competition between energy transfer and radiative emission of the donor. The relative lifetimes between a donor and acceptor is an important consideration, where QDs have been found to be inefficient energy acceptors when coupled to organic dyes but efficient energy acceptors when coupled to dye complexes with long radiative lifetimes.²⁹

High quality QDs are typically synthesized in non-polar solvents and capped with organic aliphatic ligands, leading to non-polar solubility. Since biomolecules are stable in polar conditions, the QDs must be prepared to increase their buffer solubility. To accomplish this, different phase transferring procedures have been employed, including ligand exchange or polymer encapsulation.^{21,29-36} Direct ligand exchange involves the displacement of hydrophobic ligands with hydrophilic ligands to increase solubility in water. In this approach, QD quantum yield (QY) values tend to decrease significantly and weakly binding ligands can dissociate from the NC and cause aggregation, leading to long-term instability.³³⁻³⁵ In the polymer encapsulation technique, an amphiphilic polymer is adsorbed onto the surface of the QD to encapsulate the hydrophobic ligands of the particle and expose hydrophilic ligands to the solvent.^{29-32,35} The interdigitation between the hydrophobic polymer ligands and the hydrophobic QD ligand shell is driven by electrostatic van der Waals forces.³⁷ This is advantageous because it can impart aqueous solubility of the QDs while maintaining their spectral properties and protecting the organic ligands from the

environment. Since polymer encapsulation is dependent on the surface ligands, this approach can be extended to other inorganic nanomaterials regardless of core composition.³⁷ The polymer also prevents direct access to the QD surface, which can be advantageous with DNA, which has multiple functional groups that can bind to the metal atoms in the QD.^{21,38,39} Limiting access to the surface can prevent unwanted nonspecific interactions between the DNA and QD surface. In this chapter, QDs were functionalized with an amphiphilic co-polymer and functionalized with DNA through carbodiimide crosslinking chemistry (EDC/NHS coupling) or azide alkyne Huisgen cycloaddition (click chemistry). The direct attachment of oligonucleotides was also investigated using an aqueous shell growth procedure to encapsulate the DNA into the QD shell and decrease the distance between the donor and acceptor.⁴⁰

Another challenge that is faced during the self-assembly of clusters is the need to tailor the stoichiometry of the donor and acceptor. This can be accomplished by purification via HPLC or gel electrophoresis after bulk assembly or by crafting the surfaces with a specific stoichiometry of linkers.^{9,41-43} In this chapter, stoichiometric control is achieved using a stepwise self-assembly approach at a magnetic solid support that allows unreacted QDs to be removed after each assembly step, leading to highly purified clusters. The resulting two-color QD clusters can be used as smart biosensors that work at the single molecule level, where multiple sensing events can be performed in tandem with high sensitivity and efficiency.

2.2 Experimental

2.2.1 Chemicals

Cadmium oxide (CdO, 99.99%), sulfur (S, 100 mesh), zinc acetate (ZnAc, 99.99%), trioctylphosphine oxide (TOPO, 90%), 1-octadecene (ODE, 90%), oleylamine (OAm, 90%), oleic acid (OAc, 90%), tributylphosphine (TBP, 97%), dodecylamine (DDA, >98%), poly(styrene maleic anhydride) cumene terminated (PSMA, $M_n=1600$), ethanolamine (EA, >99.5%), sodium phosphate monobasic monohydrate (98%), sodium phosphate dibasic heptahydrate (98%), chloroform (CHCl_3 , >99.8%), methanol (MeOH >99.8%), acetone (99.5%), were obtained from Sigma-Aldrich and used without further purification. Selenium (Se, 99%) was purchased from Alfa Aesar. 1-Ethyl-3-(3-dimethylaminopropyl) carbodiimide HCl (EDC), N-hydroxysulfosuccinimide (sulfo-NHS) and MagnaBind Streptavidin magnetic bead (MB) were purchased from Thermo Scientific. Jeffamine Polyetheramine M1000 (NH_2 -PEG, $M_n=1000$) was obtained from Huntsman Int. LLC. 2-(N-morpholino) ethanesulfonic acid (MES) and Agarose were obtained from Acros organics. CdSe cores were purchased from NN-Labs, LLC. Oligonucleotides with various functional groups were purchased from IDT Inc. A Vacuum Atmospheres Omni glovebox provided an inert atmosphere for synthesis. Ultrapure water (18.2 M Ω) was provided from a Sartorius Stedim Arium 61316 reverse osmosis unit combined with an Arium 611DI polishing unit.

2.2.2 Synthesis and Functionalization of Quantum Dots.

Quantum Dot Synthesis. CdSe/ZnS QDs that were synthesized in house followed traditional methods.⁴⁴ In a typical synthesis of a CdSe core, 0.025 g (0.2 mmol) of CdO was dissolved in 3.0 mL of OAc by heating at 230 °C under Ar. Next, 0.9 g (5 mmol) of DDA and 0.5 g of TOPO were dissolved in 5.0 mL of ODE and heated to 270 °C. At 270 °C, 0.118 g (1.5

mmoles) of Se dissolved in 1.0 mL of TBP was injected to induce nucleation and growth. The growth was quenched after a few seconds by injecting 10 mL ODE at room temperature. The resulting CdSe QDs were then purified free of excess ligands by multiple methanol extractions, and finally by precipitation in acetone.⁴⁵ The DDA/TOPO-capped CdSe QDs were dried under N₂ and dispersed in chloroform. The ZnS shell was deposited via SILAR,⁴⁴ in which a known amount of CdSe core was dispersed in ODE after evaporating chloroform and heated to 200 °C under Ar and 0.05-0.1 mL zinc precursor (200 mM ZnAc dissolved in OAm) and the sulfur precursor (200 mM elemental S dissolved in ODE) were injected sequentially in order to tailor ZnS growth, allowing a minimum of 10 min between injections to allow for shell annealing. After enough precursors were added to obtain the desired shell thickness, a final 0.1 mL injection of zinc was added to ensure a Zn²⁺ cation at the outermost surface of the QD. After the final injection, the QDs were annealed for an additional 30 min to ensure shell quality. The reaction mixture was allowed to cool to room temperature and cleaned in the same manner as the core.

Polymer Encapsulation and ssDNA functionalization. In a typical polymer wrapping and phase transfer experiment, 5-15 nmoles of synthesized CdSe/ZnS QDs were ligand exchanged with TOP by heating a QD solution in ODE to 70 °C under Ar overnight. The QD/TOP was cleaned via acetone precipitation and resuspended in chloroform. Next, the QDs were gently mixed with 0.5-1.5 μmoles of PSMA ([QD] : [PSMA] = 1 : 100-300) overnight in chloroform at room temperature followed by the addition of PEG ([PSMA] : [PEG] = 1 : 5.4) which resulted in the conjugation of the PEG to the maleic anhydride rings of PSMA, forming an amide linkage and a free carboxyl group.²⁹ The mixture stirred for 1 h before 50-100 μL of EA and 1 mL ultrapure water were added and stirred for another 1 h. The EA serves as both a base to deprotonate the carboxyl as well as to saturate any free MA moieties remaining in the PSMA.²⁹ Next, the

chloroform was removed through rotary evaporation forming a dry film. Then, 1 mL of 10 mM phosphate buffer (pH = 7.3) was added and the reaction mixture was back-extracted with fresh chloroform three times, improving the clarity and stability of the solution. The final aqueous dispersed QD was obtained after mild centrifugation at 3000 rpm for 2 min to remove extra chloroform-dissolved residues and precipitates. The resulting PEG/COOH/PSMA-QDs were washed with 10 mM pH = 7.3 phosphate buffer using 100K molecular weight cut-off spin filter, as well as a 2 μ m and 200 nm size filter or they were purified in a sucrose based density gradient. Next, ssDNA coupling to the QDs proceeded via the EDC/sulfo-NHS route.⁴⁶ For the CdSe/ZnS emitting at 520 or 570 nm (QD(520) or QD(570)), two different ssDNA were used, namely **A**-type and **B**-type (**A** = 5'-ATT GGA TTG GAA GTA(TTT)₁₅-NH₂-3'; **B** = 5'-TTC TCT ACA CTG TCT(TTT)₁₅-NH₂-3'). During the EDC/NHS reaction, EDC and sulfo-NHS were added to the QD ([EDC] = [sulfo-NHS] = 2000 x [QD]) followed by a 1 : 1 ratio of **A** and **B** with the QD ([**A**] + [**B**] = 100 x [QD]). A stepwise salting technique was applied over the course of 1 h to bring the NaCl concentration to 0.1 M. The mixture was reacted for an additional hour before the QD/DNA conjugates were purified by precipitating QD/DNA at 4 C at 171,500 rcf for 2 hours. The supernatant was removed and the purified QD/DNA conjugates were resuspended in BBS (pH = 7.4, [NaCl] = 0.05 M). A similar approach was used to functionalize the **B'**-type ssDNA (**B'** = 5'-AGA CAG TGT AGA GAA(TTT)₁₅-NH₂-3') to the surface of the QD(630). The concentration of resulting **AB**/QD(570) and **B'**/QD(630) were determined by measuring the first absorption maxima and comparing it to the calculated extinction coefficient.⁴⁵

DNA Quantification. The number of DNA duplexes bound to the surface of **A**/QD(570) was determined using a fluorescence technique.^{46,47} In this procedure, the **A'**-type ssDNA modified with CY3 (**A'**-**CY3** = CY3-5'-CTT GTG TCT ACT TCC AAT CCA ATT TTT-3') was used. In a

typical experiment, $A/QD(570)$ was incubated with 100 molar excess of $A'-CY3$, in PBS overnight. The conjugate was then centrifuged at 140,000 rpm for 1 hour to form a visible aggregate, and the fluorescence of the unhybridized oligonucleotides in the supernatant was measured. Fluorescence intensities were compared to a calibration curve, and the number of bound $A'-CY3$ was calculated.

2.2.3 DNA Modification of a Solid Support

ssDNA Modified Magnetic Support. The ssDNA modified colloidal magnetic beads (MB) were prepared using 300-500 μL of streptavidin-functionalized MB in 200 mM PBS. The MBs were first washed via magnetic separation in 100 mM PBS to remove any preservation agent or free streptavidin in the commercial stock. After three washing steps, 50 μL of 100 μM of A' -type ($A' = 5'-\text{CTT GTG TCT ACT TCC AAT CCA ATT (TTT)}_4\text{-Biotin-3}'$) was added and incubated for 2-3 hr. The A' uptake was monitored by UV-vis at 260 nm. Finally, the supernatant was removed after collecting the A'/MB via magnetic separation and dispersed in 0.5-1.0 mL of 100 mM BBS.

2.2.4 Cluster Assembly and Release. In a typical stepwise assembly experiment, 30-100 pmoles of $AB/QD(570)$ were incubated with 200-300 μL of 4-7 μM A'/MB solution ($[A']/[A/QD] = 8-15$) for 2-3 hr in 0.5 M PBS. Here, A'/MB concentration is based on the measured A' absorbed. Assembly was observed by measuring the decrease of the supernatant's PL intensity. The bound $AB/QD(570)$ were separated from unreacted ones via magnetic separation of the MB support and decanting the supernatant, followed by replenishment of the buffer volume. Next, the $B'/QD(630)$ was added in excess (or controlled stoichiometry, see text) and incubated with the bound $AB/QD(570)$. Similarly to the first step, the PL spectral change was monitored. Finally, the bound $AB/QD(570)+B'/QD(630)$ was again purified from excess or unreacted materials by magnetic separation, followed by the addition of fresh buffer. The clusters were then released from the

support by addition of A'' -type ssDNA fuel strands ($A'' = 5'$ -ATTGGATTGGAAGTAGACACAAG-3') at $[A'']/[AB/QD(570)] = 80$ -100. Cluster release was observed by an increase in PL intensity. Finally, the solid support was removed via magnetic separation, and the supernatant containing the released clusters was collected and stored in the refrigerator.

2.2.5 Instrumentation

UV Visible Spectroscopy (UV-Vis). A Varian Cary100 Bio UV-Vis spectrophotometer equipped with high precision Peltier heating controller and 8-cell automated holder was used in the range of 200-900 nm with baseline correction.

Photoluminescence Spectroscopy (PL). QD PL emission and cy3 experiments were performed on a Horiba Jobin Yvon Fluoromax-4 photon counting spectrophotometer equipped with a 150 W xenon white light excitation source, computer controlled monochromator and a polarizer. The detector is a R928P high sensitivity photon counting detector that is calibrated to emission wavelength. QD QY measurements were measured using 2 nm excitation and emission slits with an excitation wavelength of 400 nm.

Dynamic Light Scattering (DLS). DLS measurements were collected on a Malvern Zetasizer Nano ZS equipped with 633 nm laser source and backscattering detector at 173° for hydrodynamic diameter (d_h) measurements using CONTIN analysis. All samples were filtered using a 0.22 μm syringe filter prior to analysis and measurements were averaged over 6-20 data points.

Fourier Transform Infrared Spectroscopy (FTIR). FTIR measurements were performed on a Thermo Scientific Nicolet 6700 instrument with a diamond ATR accessory and a liquid N_2 cooled MCT detector. Spectra were averaged over 128 scans and baseline corrected.

Organic soluble QDs in toluene were drop casted onto the diamond and the solvent was evaporated for the measurements. Aqueous soluble QDs were acetone precipitated and resuspended in methanol. The solutions were drop casted and the solvent was evaporated prior to the measurements.

Gel Electrophoresis. A VWR 89032-292 model gel box was equipped with VWR 300 V model power source. Gels were photographed using a digital camera on a VWR UV transilluminator.

Ultracentrifugation. All sucrose gradient ultracentrifugation measurements were performed on a Beckman Coulter Optima Max XP Ultracentrifuge at 4 °C for 30-60 minutes at 131,000 rcf. In a typical experiment, an ultracentrifuge tube was loaded with 15%-65% sucrose gradient (w/v) solutions by successively adding heavier solutions from the bottom of the tube up. The solutions were allowed to set overnight at 4 °C to form a continuous gradient. The tubes were imaged using a Canon EOS Rebel T5 EOS 1200D digital camera under UV excitation. After ultracentrifugation, the separated regions were collected with a pipette.

Time Correlated Single Photon Counting Measurements (TCSPC). All TCSPC measurements were obtained by Dr. Mircea Cotlet at Brookhaven National Laboratory in Upton, NY and fit to biexponential decay fits.

2.2.6 Calculations

Quantum Dot Concentration. QD concentration was calculated by finding the extinction coefficient using Equation 2.1 as previously described.⁴⁵

$$\epsilon = 5857d^{2.65} \quad (2.1)$$

where ϵ is the extinction coefficient and d is the diameter of the nanoparticle. The extinction coefficient was used to find the concentration through Beer's Law in Equation 2.2.

$$\text{Abs}=\epsilon bc \quad (2.2)$$

where Abs is the absorbance at 400 nm, b is the path length (1 cm) and c is the concentration of the quantum dot.

Quantum Yield. QD photoluminescence quantum yields (QY) were calculated using Equation 2.3 based on comparison to a reference dye.⁴⁸

$$QY_{QD} = QY_R \left(\frac{Abs_R}{Abs_{QD}} \right) \left(\frac{PL_{QD}}{PL_R} \right) \left(\frac{\eta_{QD}}{\eta_R} \right)^2 \quad (2.3)$$

where QY is quantum yield, QY_R is quantum yield of the reference (rhodamine 6G = 0.95), A_R is the absorbance at 400 nm of the reference, A is the absorbance at 400 nm of the QD. PL and PL_R are the PL for QD and of the reference, respectively, η is the refractive index of the QD or QR solvent and η_R is the refractive index of the reference solvent. The samples were prepared with an optical absorption below 0.10 to limit inner filter effects.

Förster Resonance Energy Transfer (FRET) Calculations. The Förster distance (R₀) is calculated using Equation 2.4.⁴⁸

$$R_0 = 9.78 \times 10^3 (\kappa^2 n^{-4} Q_D J(\lambda))^{1/6} \quad (2.4)$$

where κ is the dipole orientation factor (κ = 2/3), η is the refractive index of the medium (η = 1.334), Q_D is the donor QY and J(λ) is the spectral overlap integral with units of M⁻¹cm³. The value for J(λ) is calculated using Equation 2.5.

$$J(\lambda) = \int PL_D(\lambda) \epsilon_A(\lambda) \lambda^4 d\lambda \quad (2.5)$$

where λ is the wavelength of the donor-acceptor spectral overlap, PL_D(λ) is the integrated donor emission normalized to unity and ε_A is the acceptor extinction coefficient at the particular wavelength. The FRET efficiency (E) is calculated using Equation 2.6.⁴⁹

$$E = 1 - \frac{\tau_{DA}}{\tau_D} = 1 - \frac{PL_{DA}}{PL_D} = \frac{R_0^6}{R_0^6 + r} \quad (2.6)$$

where τ_{DA} is the fluorescence lifetimes of the donor in the presence of the acceptor, τ_D is the lifetime in the absence of the acceptor, PL_{DA} is the steady state fluorescence of the donor in the presence of the acceptor, PL_D is the fluorescence of the donor in absence of the acceptor and r is the distance between the donor and the acceptor. The overlap integral and Förster distance was calculated with the optical spectra using the software PhotoChemCad.

Fluorescence Lifetime (τ) Calculations. Fluorescence lifetime measurements were fit to biexponential decays, as expressed in Equation 2.7.⁴⁹

$$I(t) = A_1 e^{-t/\tau_1} + A_2 e^{-t/\tau_2} \quad (2.7)$$

where $I(t)$ is the time domain intensity decay, A_1 and A_2 are the preexponential factors and τ_1 and τ_2 are the fluorescence lifetimes.

Average fluorescence lifetimes (τ_{avg}) were calculated using the preexponential factors (A_i) and lifetimes (τ_i) that were obtained from the biexponential decay fit as shown in Equation 2.8 and it is proportional to the area under the decay curve.⁴⁹

$$\tau_{avg} = \sum_i A_i \tau_i \quad (2.8)$$

The energy transfer efficiency was calculated from the fluorescence lifetimes using Equation 2.6.

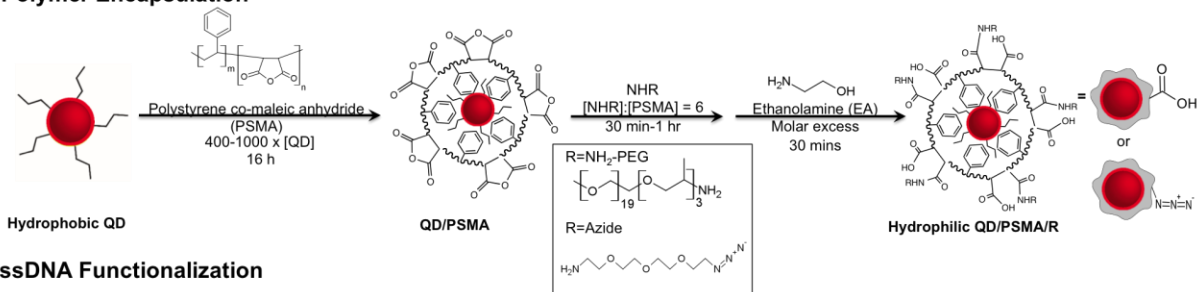
2.3 Results and Discussion

2.3.1 DNA Functionalization via Polymer Encapsulation

The CdSe/ZnS core/shell QDs used in these studies were synthesized with varied core diameters to obtain tunable emission colors to control the energy transfer acceptor or donor character. As shown in Scheme 2.1, non-polar QDs were transferred into buffers using a polymer encapsulation procedure that used an amphiphilic copolymer, polystyrene-co-maleic anhydride (PSMA).²⁹ The maleic anhydride rings in the PSMA were conjugated with different amine terminated molecules to form an amide linkage at each monomer and to introduce various functional groups for further DNA functionalization. For QDs that were functionalized with DNA via EDC/NHS coupling, an amine terminated polyethyleneglycol macromolecule (NH₂-PEG) was used. To obtain the necessary functional groups on the polymer surface for click chemistry, 11-azido-3,6,9-trioxaundecan-1-amine (azide) was used. In both systems, excess ethanolamine (EA) was also used to saturate the remaining anhydride groups and to protonate the carboxylic acids that were produced during the ring opening step. This process creates a combination of PSMA-, NH₂-PEG-, EA-capped QDs or PSMA-, Azide-, EA-capped QDs. Next, multiple 30 bp DNA strands were conjugated to the polymer wrapped QDs using EDC/NHS coupling or click chemistry approaches. EDC/NHS coupling is susceptible to hydrolysis,⁴⁹ so QD biofunctionalization using click chemistry was explored because it provides comparable functional group selectivity and is not as susceptible to hydrolysis.³⁵ For the QD assembly, the QDs that emitted at lower wavelengths acted as the energy donors (D) and were functionalized with equal molar mixtures of **A** (5'-ATT GGA TTG GAA GTA-3') and **B** (5'-TTC TCT ACA CTG TCT-3') type DNA strands to create **AB**/QD_D. The QDs that emitted at higher wavelengths acted as the energy acceptors (A) and were modified with **B'** type DNA strands (5'-AGA CAG TGT AGA GAA-3') to create **B'**/QD_A. The

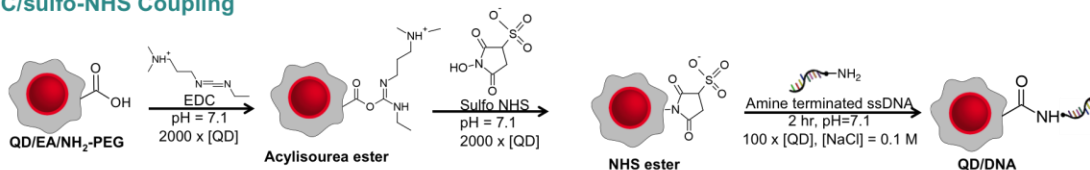
DNA/QD conjugates were purified from excess unreacted DNA by precipitating the DNA/QD and removing the supernatant.

Step 1: Polymer Encapsulation

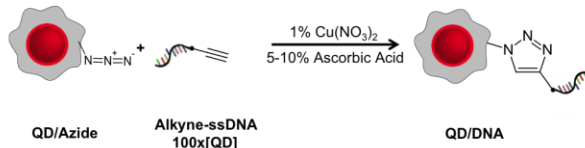


Step 2: ssDNA Functionalization

EDC/sulfo-NHS Coupling

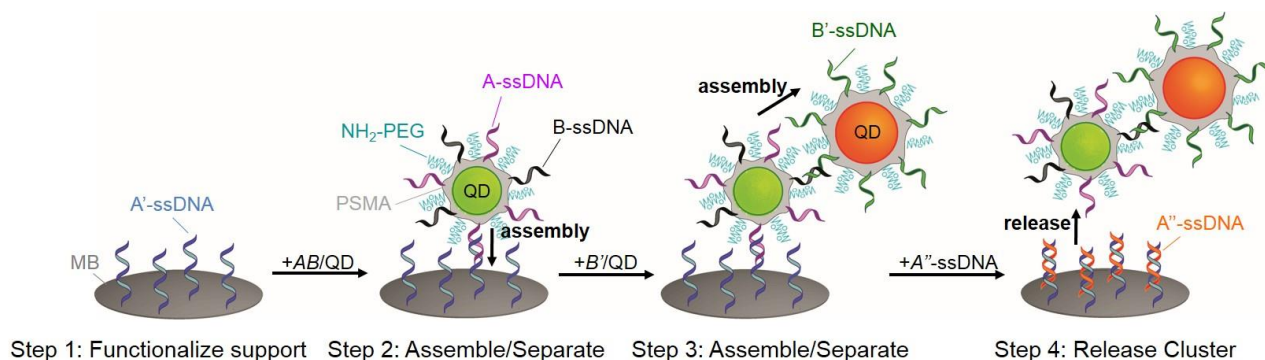


Click Chemistry



Scheme 2.1: Overview of the QD Polymer encapsulation procedure employed for phase transferring QDs into aqueous environments.

Next, the QD/DNA conjugates were assembled and disassembled on a solid support (MB), as shown in Scheme 2.2. In these experiments, AB/QD_D was coupled to the magnetic support, A'/MB , through 15 complementary bp. Next, the magnetic support was collected and unreacted QDs were removed. A second QD, B'/QD_A , was assembled at the AB/QD_D through 15 complementary bp and reacted for 2 hours before the solution was magnetically collected and purified of unreacted QDs. Finally, the multicolor QD cluster, QD_D-QD_A , was released from the support through the addition of a fuel strand (A''), which had a 30 bp complementarity to A'/MB .



Scheme 2.2: High throughput DNA-mediated assembly of two color QD clusters on a solid support.

DLS was used to probe the change in hydrodynamic diameter (d_h) at each functionalization step, as shown in Figure 2.1. For AB/QD_D , there is an increase in d_h from 7.8 nm to 12.9 nm after polymer encapsulation and an increase to 17.3 nm after DNA functionalization. This corresponds to a total increase of 9.5 nm. For B'/QD_A , the total increase in d_h was 24 nm. This data indicates that the polymer encapsulation and ssDNA functionalization leads to a significant increase in the shell capping layer. This is important because FRET is highly dependent on donor-acceptor distances. The released cluster showed a d_h of 170 nm with a large broad peak, which is more than triple the summation of the d_h for the individual ssDNA/QD conjugates. The large increase in d_h can be attributed to the high repulsions between clusters due to the highly negatively charged unhybridized DNA strands.

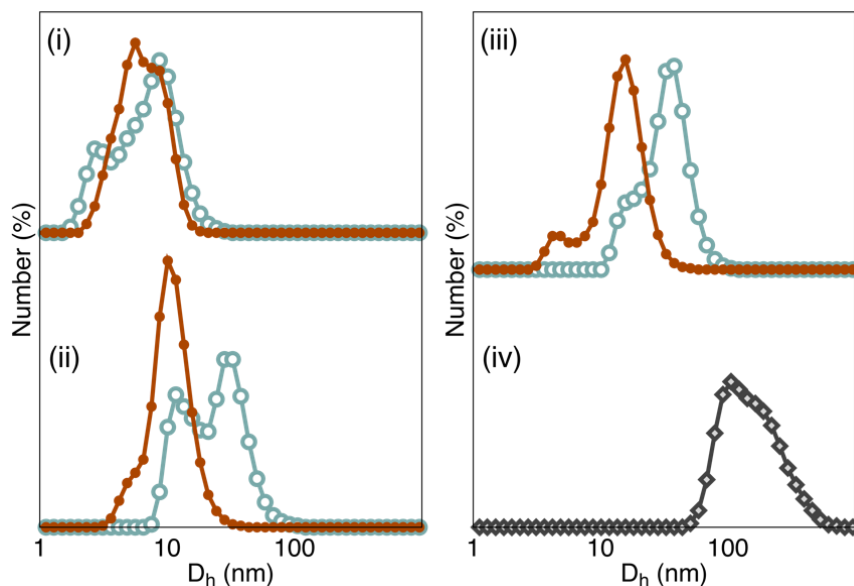


Figure 2.1: Representative number weighted DLS results for QD_D (blue circles) and QD_A (red circles) of QDs after polymer encapsulation, DNA conjugation and assembly. (i) QD/TOP (QD_D $d_h = 7.8 \pm 2.8$ nm; QD_A $d_h = 6.4 \pm 2.9$ nm); (ii) NH₂-PEG/EA/QD (NH₂-PEG/EA/QD_D ($d_h = 12.9 \pm 3.0$ nm); NH₂-PEG/EA/QD_A $d_h = 22.1 \pm 9.0$ nm); (iii) ssDNA/QD (**AB**/QD_D $d_h = 17.3 \pm 5.5$ nm; **B'**/QD_A $d_h = 30.0 \pm 8.1$ nm); (iv) Released **AB**/QD_D + **B'**/QD_A cluster from solid support ($d_h = 169.1 \pm 36.8$ nm).

The PSMA wrapped QDs were also analyzed using FTIR to confirm the presence of the necessary functional groups, as shown in Figure 2.2 for the QD/PEG/EA conjugates and in Figure 2.3 for the QD/Azide/EA. In the final PSMA wrapped QD spectra, the characteristic peaks for the carbonyl groups on the maleic anhydride ($\nu = 1850$ cm⁻¹ for the C=O symmetric stretch and $\nu = 1775$ cm⁻¹ for the C=O asymmetric stretch) disappeared. This indicates successful maleic anhydride conjugation during the PSMA wrapping procedure. Another indication for successful functionalization is the appearance of the characteristic methoxy peaks for PEG at $\nu_1 = 2860$ cm⁻¹ in Figure 2.2 and the characteristic stretch for the azide group ($\nu = 2100$ cm⁻¹) in Figure 2.3. The appearance of the broad peak at $\nu_4 = 3250$ cm⁻¹ is at the typical location for both the OH and NH stretches that are associated with the creation of the carboxylic acid amide group that formed as a

result of opening the maleic anhydride rings. The peak at $\nu = 1630 \text{ cm}^{-1}$ is indicative of the amide formation at the carboxylic acid after the PEG and azide conjugation.

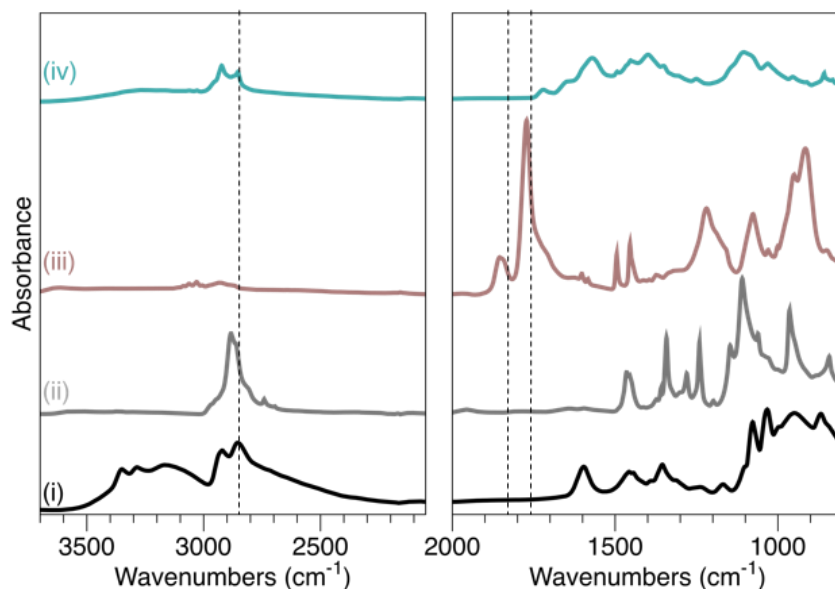


Figure 2.2: FTIR for surface linking through EDC/NHS coupling: (i) EA, (ii) NH_2 -PEG, (iii) PSMA, (iv) QD/PEG/EA

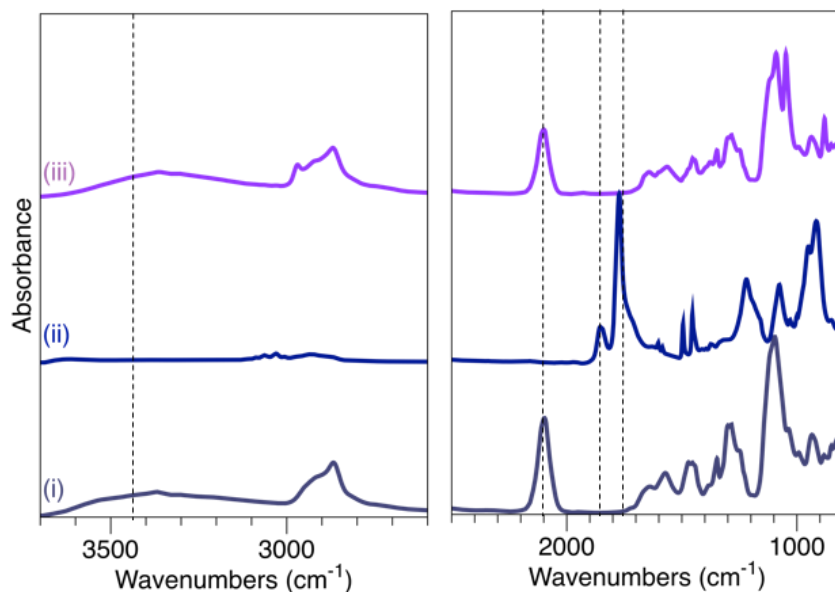


Figure 2.3: FTIR for surface linking through click chemistry: (i) Azide, (ii) PSMA, (iii) QD/Azide.

The effects of the different ring opening agents on QD optical properties and gel mobility are shown in Figure 2.4. After PSMA encapsulation and modification with PEG or azide alone, there was a significant drop in QY. When EA was used in conjunction with these molecules, the QY retention was higher. Although the QY decreased with these molecules, it was beneficial to use these molecules to impart functional groups that were reactive towards the DNA as well as the increased buffer stability that is associated with PEG molecules. Gel electrophoresis of PSMA encapsulated QDs (QD/PSMA) with different surface modifications is also shown in Figure 2.4. When azide or PEG was used as the nucleophile there was a streak in the gel instead of a band, indicating that the dots were either wrapped unevenly or precipitation occurred. An increase in gel mobility with EA compared to QDs functionalized with azide or PEG is consistent with the smaller size of the EA.

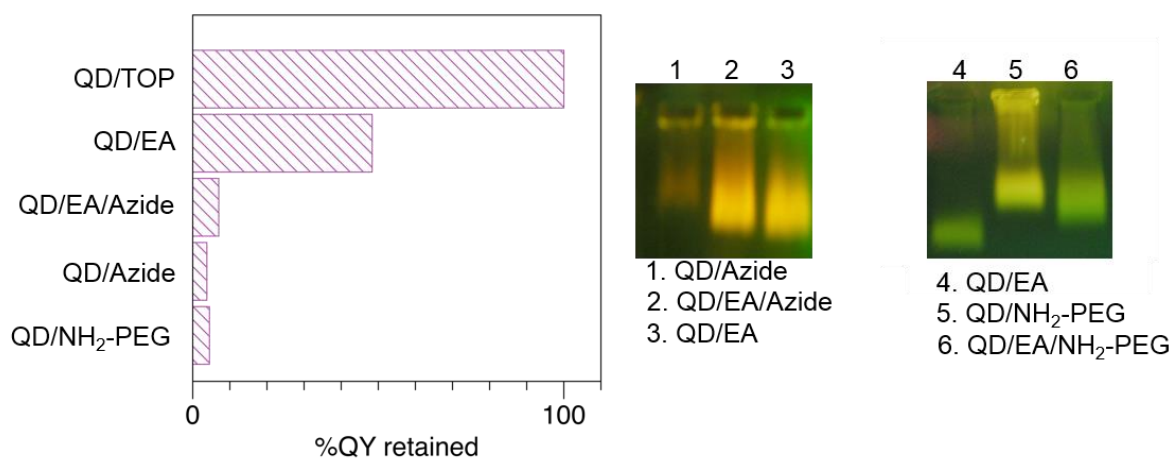


Figure 2.4: Effect of polymer encapsulation and functionalization on QD QY and gel mobility. (0.8-1% Agarose gel, 70-75 V, 40-45 mins)

In order to optimize the phase transfer protocol for the PSMA wrapping, the effect of QD concentration during the polymer encapsulation is shown in Figure 2.5. For these experiments, 2.5 nmoles of QDs were diluted with chloroform to different concentrations ($[QD] = 0.5 \mu M, 1 \mu M, 5 \mu M, 10 \mu M$) before the polymer wrapping procedure was carried out. The transfer efficiency (%t

= $[QD/EA]/[QD] \times 100\%$) was used to quantify the success of the different samples. QDs polymer wrapped in a 0.5 μM solution had the lowest yield (%t = 4.5%) and a featureless absorbance spectrum. As the [QD] increased, the absorption features associated with the QD were more defined. The highest %t was at 1 μM and the highest QY was obtained with 5 μM solution. The PSMA wrapping that occurred in the 5 μM also had the lowest scattering out of all of the samples. The low %t at the higher QD concentrations is most likely due to the precipitation of QDs from the solution. When the density of QDs is too high, then the polymer can encapsulate multiple QDs in one PSMA micelle, creating a large and unstable aggregate. At the lower concentration, the low %t is most likely a result of fewer QDs coming into contact with the PSMA.

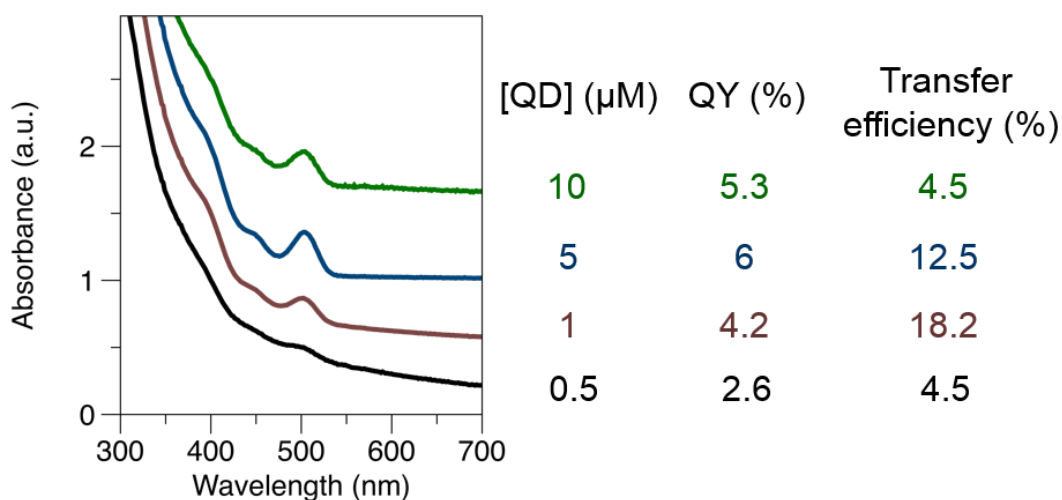


Figure 2.5: Effect of QD concentration on the final QD/PSMA conjugate.

The effect of encapsulating the QD with different polymers was also investigated. For these studies, QDs were phase transferred using three different co-polymers: poly(styrene-alt-maleic anhydride) (PSMA), poly(isobutylene-alt-maleic anhydride) (PIMA) and poly(maleic anhydride-alt-octadecene) (PMAO). The absorbance spectra, gel mobility and d_h for the different QD polymer conjugates were compared. As shown in Figure 2.6, QDs wrapped with PMAO had the smallest d_h and faster gel mobility compared to the QDs with the other polymers. The smaller QD polymer

conjugate can be attributed to the stronger dispersion forces between the linear hydrocarbon chains of the polymer and the linear hydrocarbon chains of the TOP on the QD surface. QDs with PIMA had the largest d_h , due to the weaker dispersion forces between the isobutylene on the polymer and the hydrocarbon chains of the TOP on the QD surface. Overall, the QD/PMAO species had the highest transfer efficiency, best quantum yield retention, the smallest d_h and the most well defined absorption spectra.

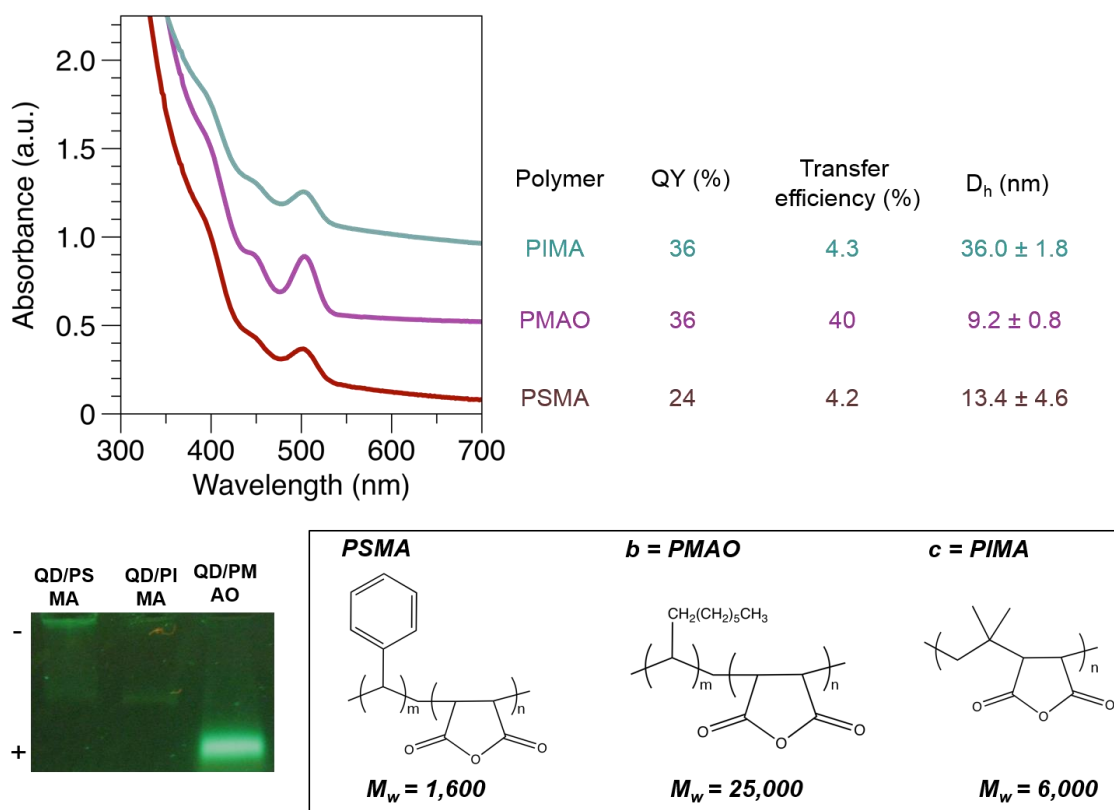


Figure 2.6: Effect of different polymers on polymer encapsulation product. UV-Vis: (a) QD(520)/PSMA, (b) QD(520)/PMAO, and (c) QD(520)/PIMA; gel electrophoresis and structures of the different polymers used in this study. [QD] = 1 μ M; gel conditions: 0.8% Agarose, 70 V, 45 mins.

The effect of changing the polymer encapsulation from chloroform to the more polar THF was investigated. When the polymer encapsulation took place in THF, the %t was 6.7%, compared to 4.2% in CHCl_3 . These conjugates also had higher QY (24% compared to 18.2% in CHCl_3) and

smaller d_h (6.8 ± 2.4 nm in THF, 13.4 ± 4.6 nm in CHCl_3). THF is a more polar solvent, which could help ease the transition of QDs from a non-polar to a polar solvent and help prevent photoluminescence quenching. These results suggest that the most successful polymer encapsulation requires PMAO encapsulation in THF with $[\text{QD}] = 1 \mu\text{M}$.

One of the largest challenges of this project was an inconsistent batch-to-batch MB-QD coupling efficiency. It was found that the optical scattering affected the QD coupling on the MB, where samples with higher UV-vis baselines had lower MB coupling success. As shown in Figure 2.7, the UV-Vis of the polymer encapsulated QDs (QD/PSMA) generally had a high absorbance scattering, which varied between samples. The solution after polymer encapsulation was also very opaque.

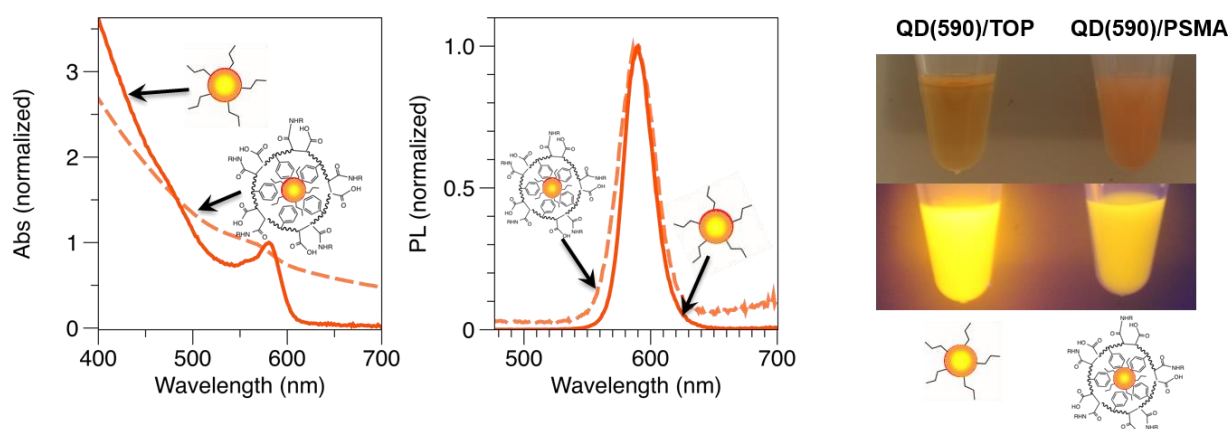


Figure 2.7: Effect of polymer encapsulation on the optical spectra and clarity of the QD sample.

The high baseline and decreased coupling efficiency was attributed to excess polymer in the system, which would affect assembly by reacting with the solid support in place of the QDs. To remove the excess polymer, the QDs were purified in an ultracentrifuge (UC) using a sucrose density gradient. This purification procedure decreased the optical scattering, as shown in Figure 2.8.

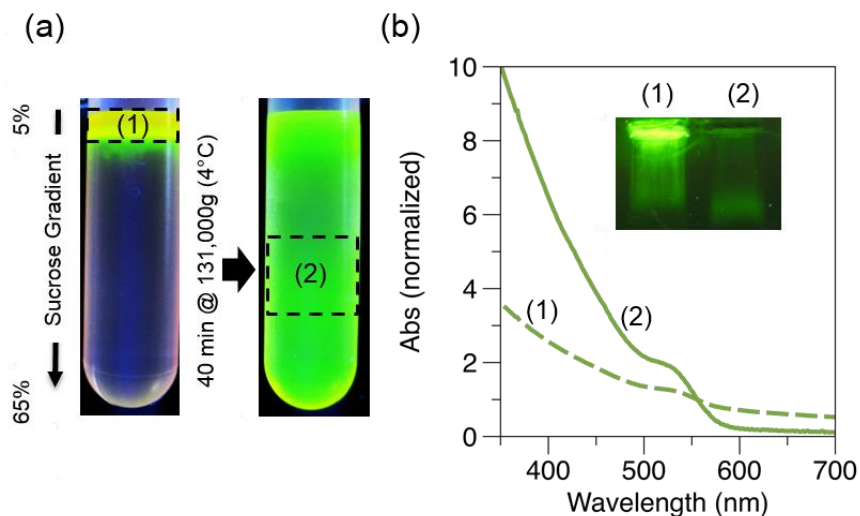


Figure 2.8: Sucrose ultracentrifugation results for the purification of QD(570) after PSMA/NH₂-PEG/EA wrapping and phase transfer: (a) image of QD/PSMA/NH₂-PEG/EA conjugates before (1) and after (2) centrifugation under UV light illumination and (b) optical changes in UV-Vis of the QDs before (1) and after (2) purification. Inset: Gel electrophoresis of QD conjugates before (1) and after (2) purification.

The decreased scattering in the absorption spectra and a more defined band in gel electrophoresis after purification indicate the removal of excess polymer conjugates. The change in d_h as a result of sucrose purification was investigated. As shown in Figure 2.9, the d_h was measured for the QD/PSMA conjugates before and after moving through the sucrose gradient. Although there was a high QD density in the top layer, the QD band that moved through the sucrose layer was considered the purified product. A decrease in d_h by 17 nm indicates the removal of excess polymer micelles and QD aggregates following the polymer wrapping procedure.

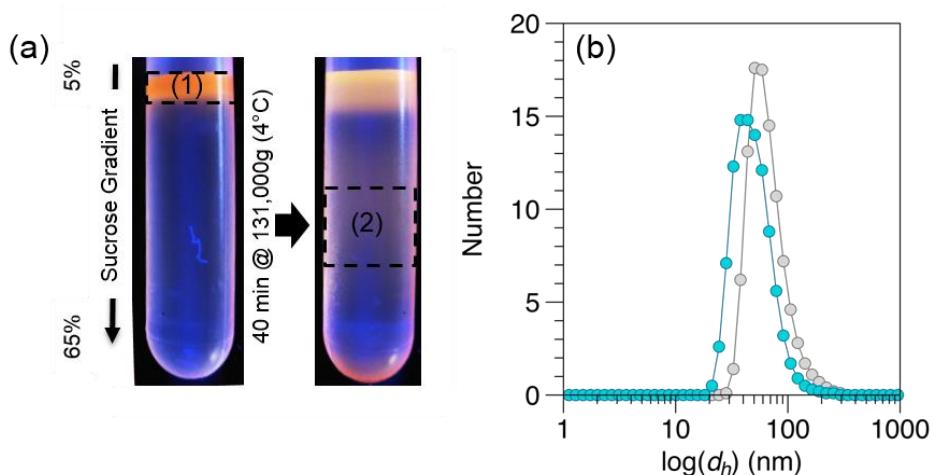


Figure 2.9: (a) UV-illuminated image of the sucrose gradient (1) before and (2) after purification and (b) dynamic light scattering results before sucrose purification (grey circles, $d_h = 68.6 \pm 4.3$ nm) and after sucrose purification (blue circles, $d_h = 51.9 \pm 9.9$ nm).

To verify that the sucrose purification removed excess PSMA, the DNA coupling efficiency for the purified and unpurified samples were compared. The number of DNA duplexes on the QD surface was quantified using fluorescent hybridization studies. As shown in table 2.1, the number of DNA duplexes per QD in the purified sample increased by more than twofold, from 6.0 ± 3.3 DNA/QD to 15.6 ± 1.5 DNA/QD. This indicates the removal of excess polymer that, if present during the DNA conjugation, would be modified with DNA and bind to the support or the QDs, decreasing the ssDNA coupling efficiency.

Sample	# DNA/QD
Unpurified QD/PSMA	6.0 ± 3.3
Purified QD/PSMA	15.6 ± 1.5

Next, the purified QDs were conjugated with DNA. As shown in Figure 2.10, QDs and quantum rods (QRs) conjugated with DNA using click chemistry showed a decrease in PL but

release was not observed. It was hypothesized that this lack of assembly in the copper mediated click chemistry DNA modification was due to the presence of copper (II) ions after DNA modification that can mediate DNA damage⁵⁰ and quench QD emission.⁵¹ Both of these processes will affect coupling efficiency.

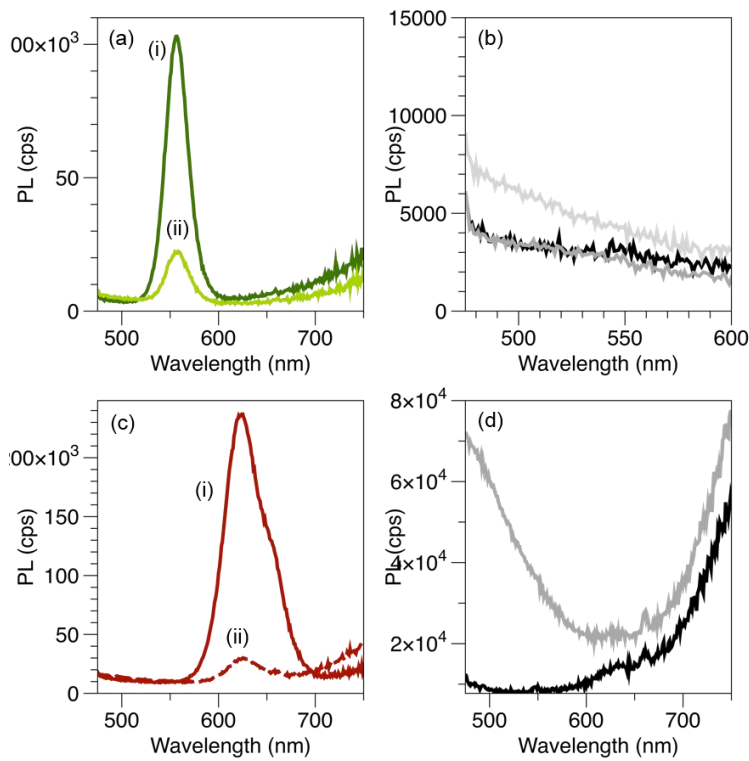


Figure 2.10: The PL monitoring of the MB supernatant for QDs and QRs incubated with the A' /MB solid support: AB (QD(570)) (a) before (i) and after 2 hours of incubation with A' /MB (ii), (b) after the addition of A'' and AB /QR(625) (c) before (i) and after 2 hours of incubation with A' /MB (ii) and (d) after the addition of A'' .

Figure 2.11a and 2.11b compare the PL decrease upon addition to the solid support for QRs with and without DNA, respectively. Since no release was observed, the PL decrease can be a result of non-specific absorption or PL decay. To determine the nature of the PL decrease, the PL decrease in QRs were measured over time. In the absence of the MB, the PL did not decrease as much as in the presence of the MB. This data indicates that the QRs are non-specifically adsorbing.

In future experiments, QDs can undergo DNA biofunctionalization using cyclooctane click chemistry that doesn't require the use of a copper catalyst³⁵ to determine if this non-specific adsorption is due to the copper ions.

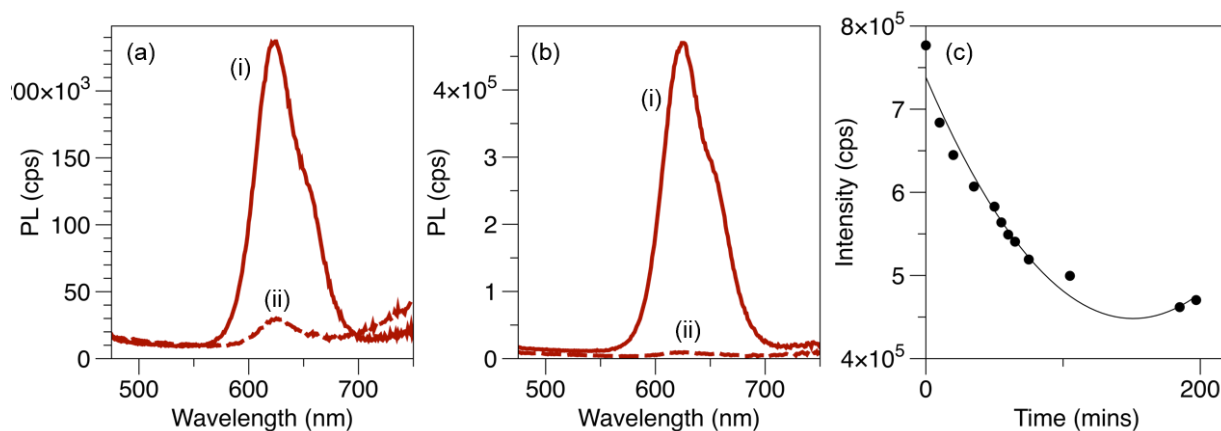


Figure 2.11: (a) *AB*/QR(625) (i) before and (ii) after 2 hours of incubation with *A'*/MB and (b) azide/QR(625) (i) before and (ii) after 2 hours of incubation with *A'*/MB; (c) PL decrease for azide/QR(625) in solution.

The assembly and disassembly of QDs modified with DNA via EDC/NHS coupling was investigated, as shown in Figure 2.12. In these experiments, the assembly and disassembly of equal molar amounts of the donor (*AB*/QD(590)) and acceptor (*B'*/QD(630)) QDs ($r = [\text{QD}(590)]/[\text{QD}(630)] = 1$) were quantitatively measured using PL. In Figure 2.12a, the decrease in *AB*/QD(590) indicated assembly and the remaining unreacted QDs were magnetically separated from the MB solution. Figure 2.12b shows the assembly of *B'*/QD(630) at *AB*/QD(590) on the solid support through the decrease in emission. In Figure 2.12c, the addition of *A''* resulted in the appearance of an emission peak, indicating the release of QD clusters from the support. The appearance of one emission peak is most likely due to the emission overlap between the two QDs.

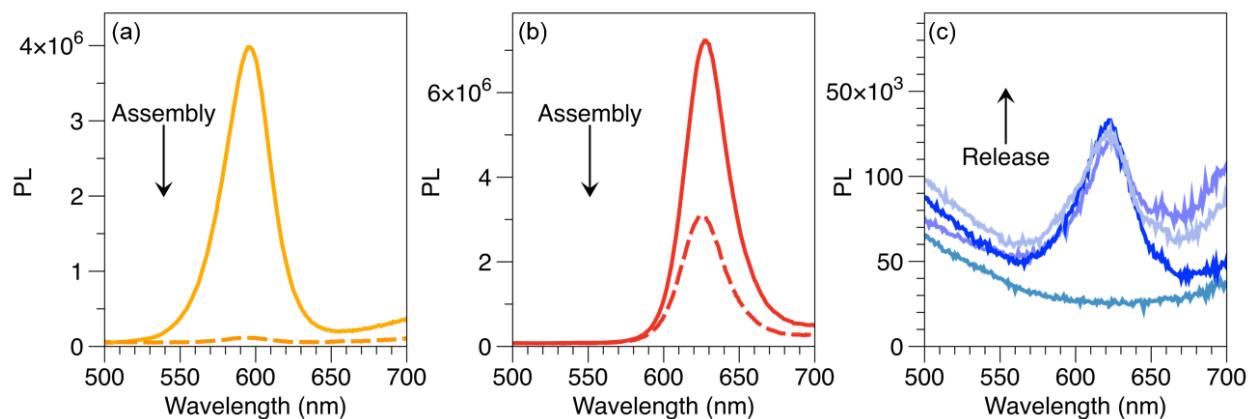


Figure 2.12: The PL monitoring of the MB supernatant during the assembly of (a) $AB/QD(590)$ at the A'/MB support, (b) $B'/QD(630)$ at the immobilized $AB/QD(590)$ and (c) the release of the DNA-linked $AB/QD(590)+B'/QD(630)$ cluster upon addition of A'' with release times of (iii) 5, (iv) 14, and (v) 24 h. ($r = [QD(630)]/[QD(590)] = 1$; $QY_D = 2\%$, $QY_A = 1\%$).

Although the released emission peak only shows one peak, peak deconvolution software calculated PL_A/PL_D of 4.2, which is higher than PL_A/PL_D of 1.8 prior to cluster assembly. The peak deconvolution results and FRET parameters are found in Figure 2.13. Current literature values report an R_0 around 5-7 nm for QD thin films⁵² and 5-6.5 nm for colloidal QD and QR systems⁵³ and 3-6 nm for QDs coupled to organic dyes⁵⁴ so this value is a little smaller than other measured R_0 values involving QD FRET. The low calculated Förster distance for the cluster is due to the low QY of the donor (2%) and the small overlap between the absorbance of the donor and the PL of the acceptor. As shown in Figure 2.13c, a 5 nm separation corresponds to an efficiency of 12%. The diameters of QD(590) and QD(630) are about 3.6 and 5 nm, respectively, based on the absorption maximum,⁴⁵ are polymer encapsulated and then are functionalized with 20 bp oligonucleotides, where the 15 hybridized bps in the cluster have a distance of about 5 nm (0.34 nm/bp).⁵⁵ Taking these distances into account, the QDs are separated by a distance of over 10 nm, which corresponds to FRET efficiency around 0.2%. Since the relative PL ratios increased more than 0.2%, the FRET efficiency in this cluster is larger than that predicted by the Förster distance.

This may give insight into the geometry of the cluster, where the QDs are in a bent rather than a linear configuration. This would decrease the distance between them and lead to a greater FRET efficiency.

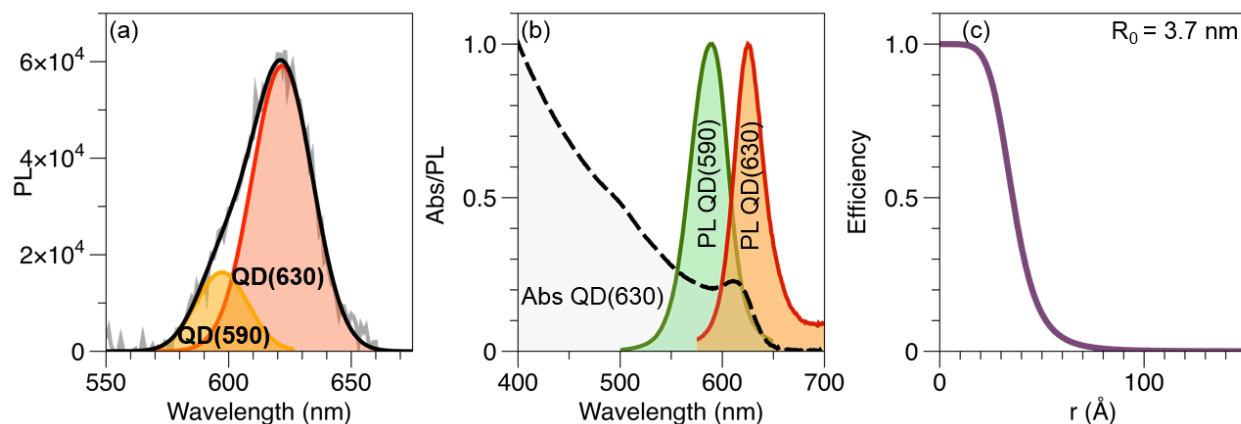


Figure 2.13: (a) Peak deconvolution for the released cluster after 24 hours of measured release ($PL_A/PL_D = 4.2$), (b) Spectral overlap of the absorbance of the acceptor (QD(630)) with the PL of the donor (QD(590)) and acceptor and (c) FRET efficiency plot for the released cluster ($R_0 = 3.7$ nm).

A control experiment was performed to investigate the non-specific binding of the QDs on the solid support. As shown in Figure 2.14, QD/PEG/EA incubated with A'MB did not show a decrease in PL, indicating the lack of non-specific adsorption onto the solid support. This confirms that the decreased emission in the assembly experiment was a result of assembly at the solid support and not non-specific adsorption or PL decay.

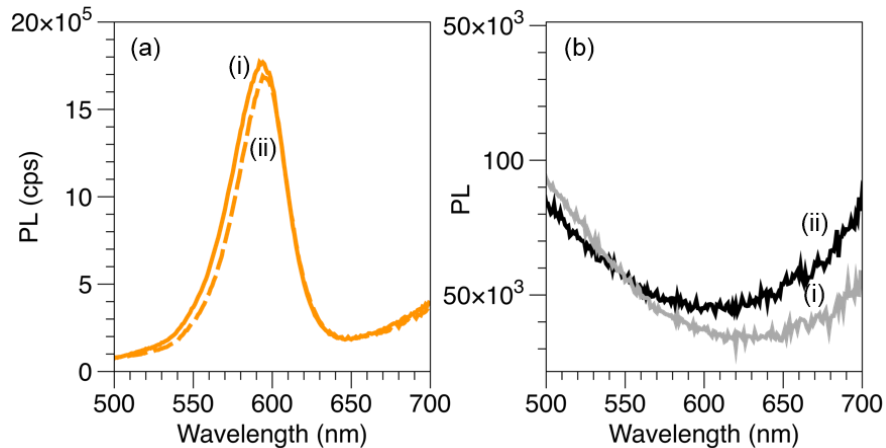


Figure 2.14: (a) QD/PEG/EA before (i) and after (ii) incubation with A'/MB and (b) after the addition of a fuel strand for (i) 2 hours and (ii) 14 hours.

The assembly and disassembly was measured for QDs with a larger separation in emission wavelengths. Figure 2.15 shows the assembly and disassembly of $AB/QD(570)$ and $B'/QD(635)$ ($r = [QD(635)]/[QD(570)] = 1$). As shown in Figure 2.15a, $AB/QD(570)$ was assembled onto the support and the remaining unreacted 3% was removed from the MB solution using a magnetic purification. In Figure 2.15b, about 80% of the $B'/QD(635)$ conjugates were assembled onto the support at the $AB/QD(570)$. After the addition of A'' to release the QD cluster, the PL emission increased at 570 nm and 635 nm, indicating the release of both QDs. The PL increase over time in Figure 2.15c indicates an increasing concentration of clusters over time.

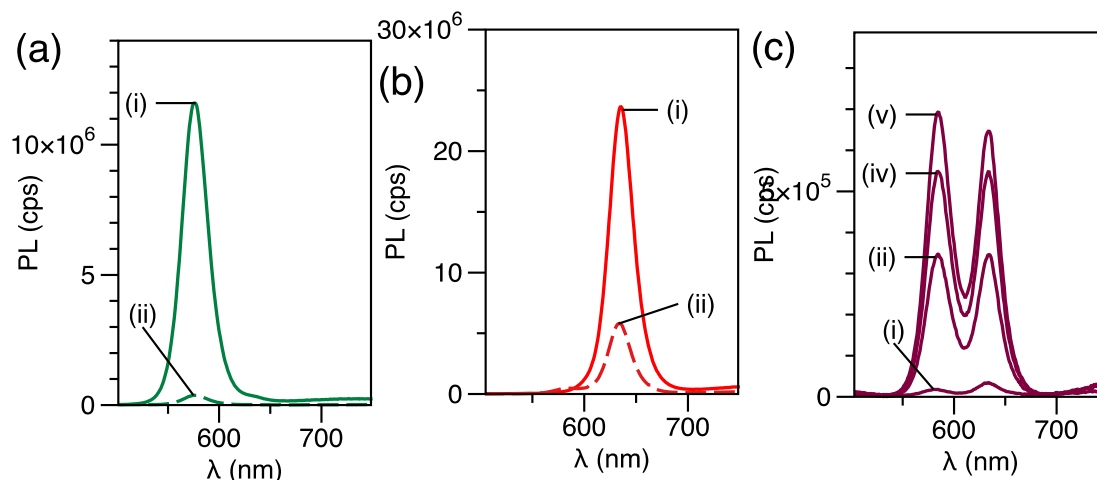


Figure 2.15: The PL monitoring of the supernatant during the assembly of *AB*/QD(570) at the *A'*/MB support (a), the *B'*/QD(635) at the *AB*/QD(570) immobilized on the *A'*/MB (b), and the release of the DNA-linked *AB*/QD(570)+*B'*/QD(635) cluster upon addition of *A''*-F (c), with release times of 2, 5, and 14 h.

Using this approach, the release of clusters with different acceptor and donor stoichiometries ($r = [\text{QD}(630)]/[\text{QD}(570)] = 0-1.3$) were prepared. As shown in Figure 2.16, the different PL emission ratios (PL_A/PL_D) of the released clusters at the different r values indicate the release of different types of clusters. The only way for the increase in PL for *B'*/QD(635) is if it is bound to *AB*/QD(570), so this data shows that the release of clusters with different stoichiometries was successful.

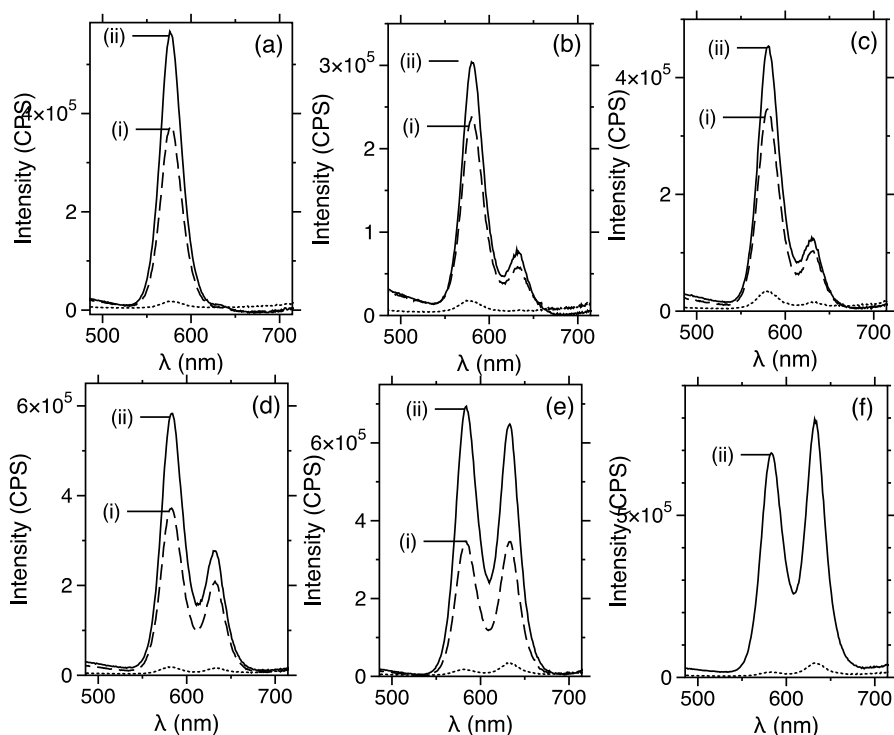


Figure 2.16: PL spectral changes for release of $AB/QD(570) + B'/QD(635)$ clusters after introducing fuel strand A'' at assembly ratios, $r = [B'/QD(635)] / [AB/QD(570)] = 0$ (a), 0.1 (b), 0.25 (c), 0.50 (d), 0.95 (e), and ~ 1.3 (f). Arrow indicates release times of 2, 5, and 14 h. ($QY_D = 6.7\%$, $QY_A = 1.8\%$).

The $AB/QD(570) + B'/QD(635)$ cluster was calculated to have a Förster distance (R_0) of 5.2 nm (figure 2.17c inset), which is low considering the use of the QD acceptor because of QD(635)'s low quantum yield. Figure 2.17c shows the PL_A/PL_D ratios of the QD(635) acceptor (PL_A), and QD(570) donor (PL_D) from the released clusters and the PL_A/PL_D control ratio based on the QY values ($QY(570) = 6.7\%$, $QY(635) = 1.8\%$) for each experimental r . A comparison of the two indicates a considerable increase in PL_A/PL_D for the assembled clusters, suggesting improved emission from the QD(635), possibly due from QD-to-QD FRET. This FRET efficiency is similar to previously reported values of QD conjugates.⁴³ In an ideal model, DNA-linkage between each QD should account for ~ 5 nm from the 15bp double-stranded region (0.34nm/bp), with additional length and

flexibility from the two separate 15bp poly-T spacers, and the additional TOPO and PSMA wrapping. Considering also the radii of each QD (1.8, 2.5 nm), one can expect donor-to-acceptor distances (center-to-center) to be at least on the order of ~12 nm.

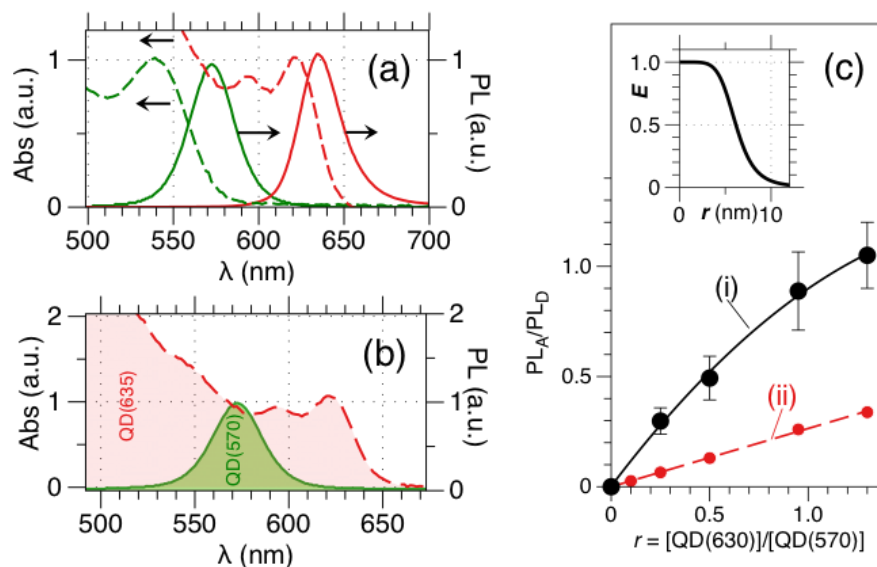


Figure 2.17: (a) The PL and UV-vis spectra for QD(570) (green) and QD(635) red. (b) Spectra overlap of QD(570) energy donor and QD(635) energy acceptor. (c) Observed PL intensity changes between the QD(570) donor (PL_D) and QD(635) acceptor (PL_A) for the released $AB/QD(570) + B'/QD(635)$ clusters at increasing r (i). Red dashed line (ii) represents simulated PL_A/PL_D based on individual QY values. Inset: Corresponding FRET efficiency plot.

In Figure 2.18, the assembly and disassembly of $AB/QD(570)$ and $B'/QD(630)$ at $r = 0.3$ was investigated where the QY of $B'/QD(630)$ was higher than the QY for $AB/QD(570)$. This is the reverse QY trend from Figure 2.16. Figure 2.18a shows the PL of the supernatant before and after the addition of $AB/QD(570)$, where the PL decrease indicates assembly at the A'/MB support. In this step, about 40% of the QDs remained unreactive. The PL decrease of $B'/QD(630)$ indicates assembly at the immobilized $AB/QD(570)$. In this step, about 64% of the QDs remained unreactive. After addition of the fuel strand, A'' , an increase in PL of both QD(570) and QD(630) was observed, indicating the release of a cluster. In this released cluster, the PL of the acceptor is higher than the PL of the donor, which is most likely due to the higher QY of the acceptor. In

Figure 2.16b, the PL of the donor ($QY_D = 6.7\%$) was higher than the PL for the acceptor ($QY_A = 1.8$) at the same r , so the reverse trend observed here is due to the higher QY of the acceptor ($QY_A = 5\%$) compared to the donor ($QY_D = 2\%$). This data suggests that the PL is not a reliable way to measure the QD stoichiometry.

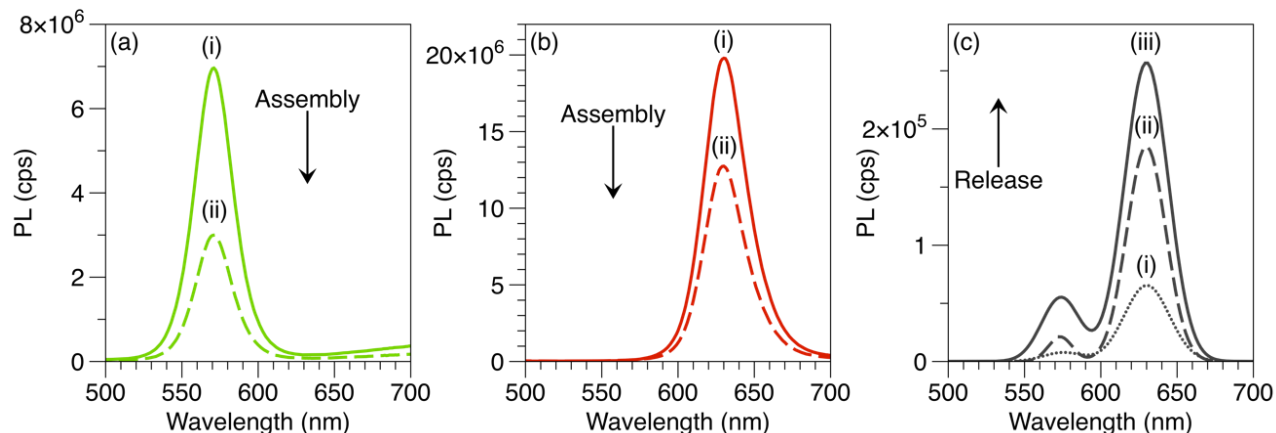


Figure 2.18: The PL monitoring of the MB supernatant during the assembly of (a) $AB/QD(570)$ at the A'/MB support, (b) $B'/QD(630)$ at the immobilized $AB/QD(570)$ and (c) the release of the DNA-linked $AB/QD(570)+B'/QD(630)$ cluster upon addition of A'' with release times of (i) 2, (ii) 5, and (iii) 14 h. ($r = [QD(630)]/[QD(570)] = 0.3$; $QY_D = 2\%$, $QY_A = 5\%$).

In Figure 2.18c, the PL_A/PL_D in the cluster is 3.1 before assembly and 5.3 after assembly, which corresponds to about 40% energy transfer efficiency. The relative increase in acceptor PL after assembly is indicative of QD-QD FRET, so the FRET parameters for this cluster were calculated, as shown in Figure 2.19. A Förster distance (R_0) of 5.3 nm was calculated for the coupled QDs from the spectral overlap and optical properties of the individual QDs.

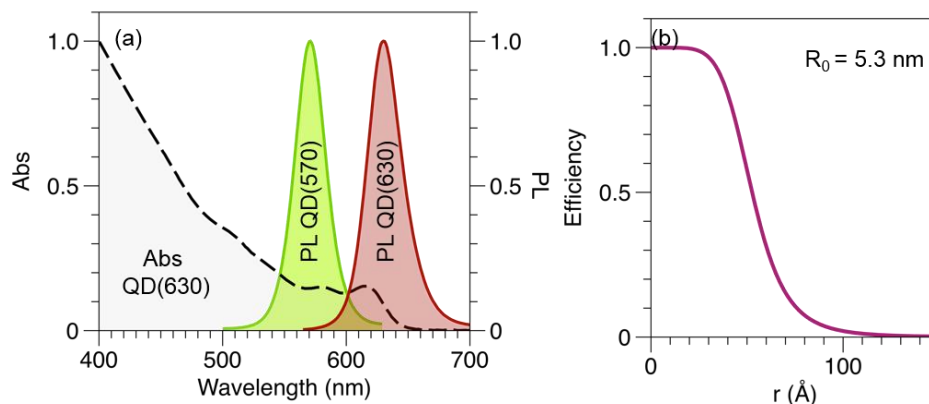


Figure 2.19: FRET parameters for the assembled cluster: (a) Spectral overlap of the absorbance of the acceptor (QD(630)) with the PL of the donor (QD(570)) and acceptor.

As shown in Figure 2.20, the lifetime was measured for a QD donor-acceptor pair ($r = [\text{QD}(630)]/[\text{QD}(530)] = 1$). The decrease in the donor lifetime in the absence ($\tau_D = 6.08$ ns) and presence of the acceptor ($\tau_{DA} = 4.05$ ns) verifies that energy transfer is occurring with an efficiency of 26%.

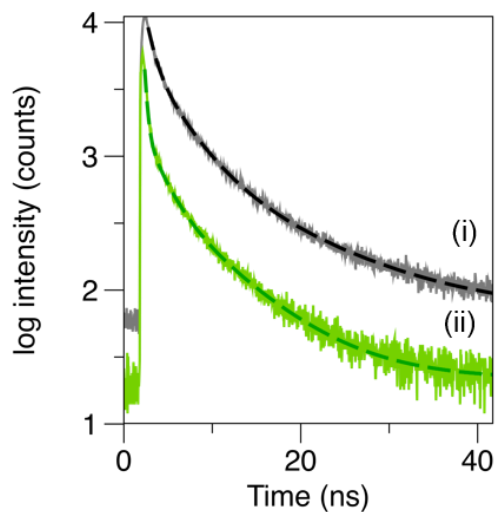


Figure 2.20: Fluorescence lifetime measurements for (i) QD(530) in the absence of the acceptor (τ_D) and (ii) donor in the presence of the acceptor (τ_{DA}). Data was fit to a biexponential fit.

This data was fit to a biexponential decay to obtain lifetime measurements, as shown in table 2.2.

Table 2.2: Biexponential fit results for lifetime measurements

	A ₁	τ_1 (ns)	A ₂	τ_2 (ns)	τ_{avg} (ns)
Donor	3816.03	3.296	976.66	10.967	6.08
Donor in the presence of the acceptor	2832.3	0.287	509.56	6.855	4.50

This data demonstrates the ability to control QD assembly at a solid support with a variety of different donor acceptor pairs and cluster stoichiometries. Lifetime measurements verified that the the enhancement in acceptor PL after QD cluster release is due to QD-QD FRET which may be due to structural changes in the QD cluster.

2.3.2 DNA functionalization via Aqueous Shell Growth

FRET is highly dependent on donor and acceptor distance,⁵⁶ so the large spatial distribution between the PSMA functionalized QDs leads to a decreased FRET efficiency. To decrease the donor acceptor distance, the direct attachment of oligonucleotides during aqueous shell growth using a phosphorothiolate modified DNA strand (pt-ssDNA) was investigated.⁴⁰ The direct attachment eliminates the large PSMA shell so distance between coupled QDs should be smaller than QD/PSMA conjugates. The aqueous shell growth procedure has also been found to embed the DNA into the QD shell, which should lead to an increased conjugate stability since the DNA is unable to dynamically bind off of the surface.⁴⁰ For this approach, QDs were phase transferred using a histidine mediated direct ligand exchange^{33,36} and a ZnS shell was epitaxially grown in the presence of pt-ssDNA.⁴⁰ First, the spectral changes were investigated during the shell growth procedure in the presence of mercaptopropionic acid only (MPA). As shown in Figure 2.21a and 2.21b, the absorbance peak became less defined and the fluorescence peak became broader and red shifted with increasing time, respectively. These spectral changes indicate an increase in QD

size with increasing shell growth times. The QY also increased during shell growth from 2.5% to 10.1% after 4 hours but decreased back to 2.8% after 24 hours. The increase in QY is very beneficial because there is usually a significant QY loss during phase transfer, which will affect energy transfer efficiency in the final assembled QD clusters.

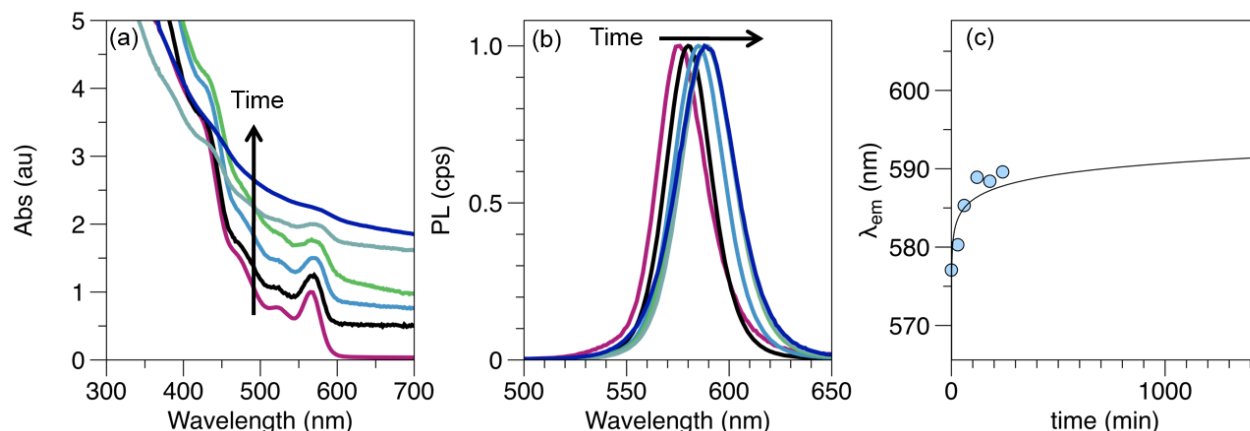


Figure 2.21: Spectral change with time of ZnS shell growth on CdSe/CdS-His conjugates in the presence of MPA: (a) UV-Vis, (b) PL and (c) emission wavelength as a function of time.

The shell growth in the presence of different ratios ($r = [\text{pt-ssDNA}]/[\text{QD}]$) was investigated via UV-Vis, PL and gel electrophoresis, as shown in Figure 2.22. As the ratio increased, the mobility of the QDs in the gel decreased, indicating an increase in QD size due to a higher loading of DNA on the surface. The emission peak also red shifted from 597 to 620 nm during the shell growth, but the addition of more pt-ssDNA did not change the red shifted emission, indicating that the red shifted emission is not from the presence of pt-ssDNA, but only from the deposition of ZnS onto the CdSe/CdS QD.

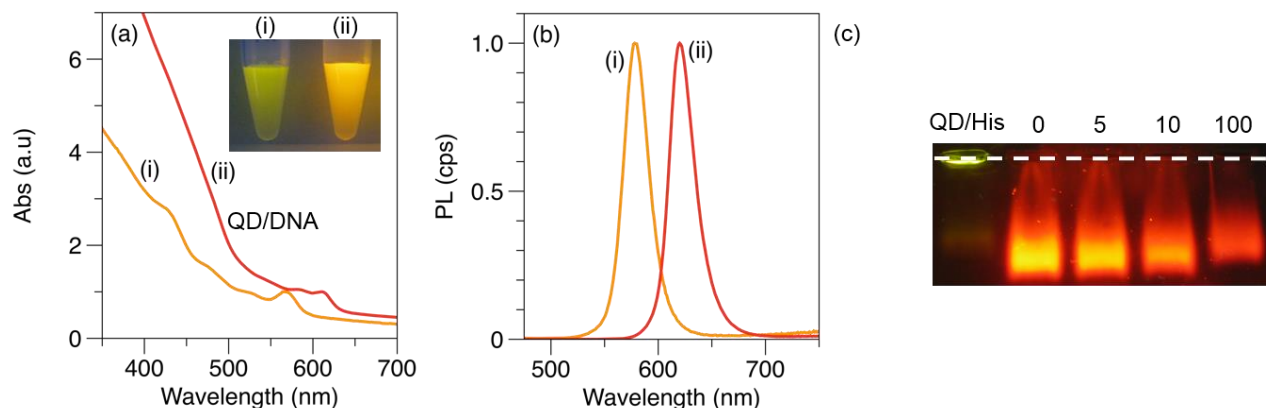


Figure 2.22: (a) UV-vis and (b) PL of (i) QD/His (CdSe/CdS-His) and (ii) QD/DNA (CdSe/CdS/ZnS-DNA) after ZnS shell growth in the presence of DNA (r [DNA] / [QD] = 100); (c): Gel electrophoresis of CdSe/CdS/ZnS-DNA conjugates after ZnS shell growth in the presence of DNA with different DNA/QD ratios ($r = 0-100$). Inset: UV-illuminated image of QD/His and QD/DNA ($r = 100$).

The QD/pt-ssDNA conjugates were assembled and disassembled on a solid support, as shown in Figure 2.23. A decrease in photoluminescence after incubation with the solid support is indicative of DNA hybridization with the support. After the addition of a fuel strand, the cluster was released, which is shown by an increase in PL over time. The PL is at the emission location of the acceptor and, based on DNA hybridization, the acceptor emission will only be present after the addition of A'' is through coupling with the donor. The absence of the donor emission could be due to the large overlap in emission wavelengths of the donor and acceptor, the energy transfer and the low QY of the donor (QY = 0.4%).

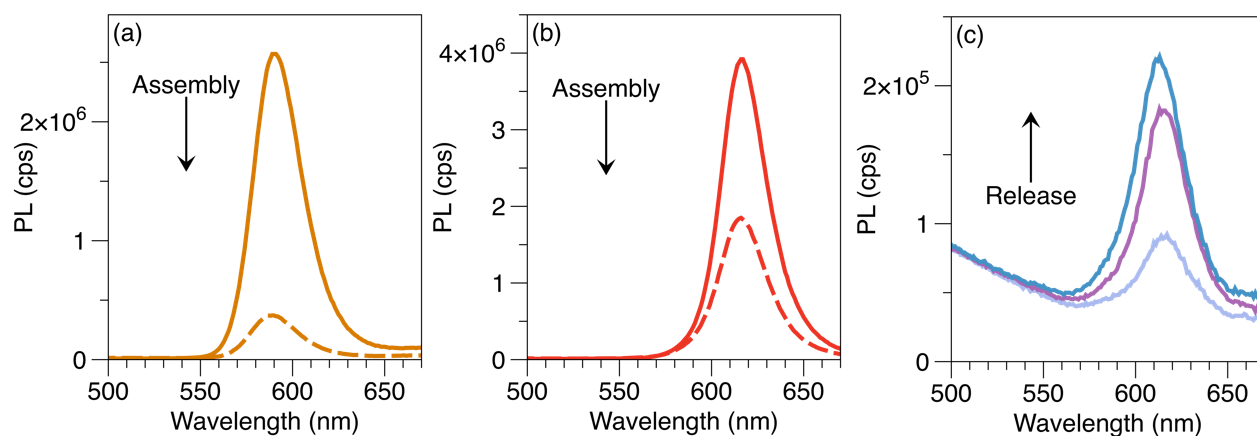


Figure 2.23: The PL monitoring of the MB supernatant during the assembly of (a) *AB*/QD(590) at the *A'*/MB support, (b) *B'*/QD(620) at the immobilized *AB*/QD(590) and (c) the release of the DNA-linked *AB*/QD(590)+*B'*/QD(620) cluster upon addition of *A''* with release times of (iii) 2, (iv) 5, and (v) 22 h. ($r = [\text{QD}(630)]/[\text{QD}(590)] = 1$; $QY_D = 0.4\%$, $QY_A = 1.7\%$).

The FRET parameters and deconvolution of the released cluster PL are shown in Figure 2.24. This assembly is comparable to the assembly of polymer wrapped *AB*/QD(590) and *B'*/QD(630) in Figure 2.13. The polymer wrapped conjugates (QD/PSMA/DNA) had an R_0 of 3.7 nm, which is comparable to the R_0 of 3.8 nm in Figure 2.24c for QD/pt-DNA conjugates. The QDs are closer together compared to the previous experiments, where they are separated by about 10 nm from the QD radii ($r = 1.8$ nm for QD(590) and $r = 2.3$ nm for QD(615))⁴⁵ and length of the DNA strands (5 nm),⁵⁵ which corresponds to an energy transfer efficiency of 3%.

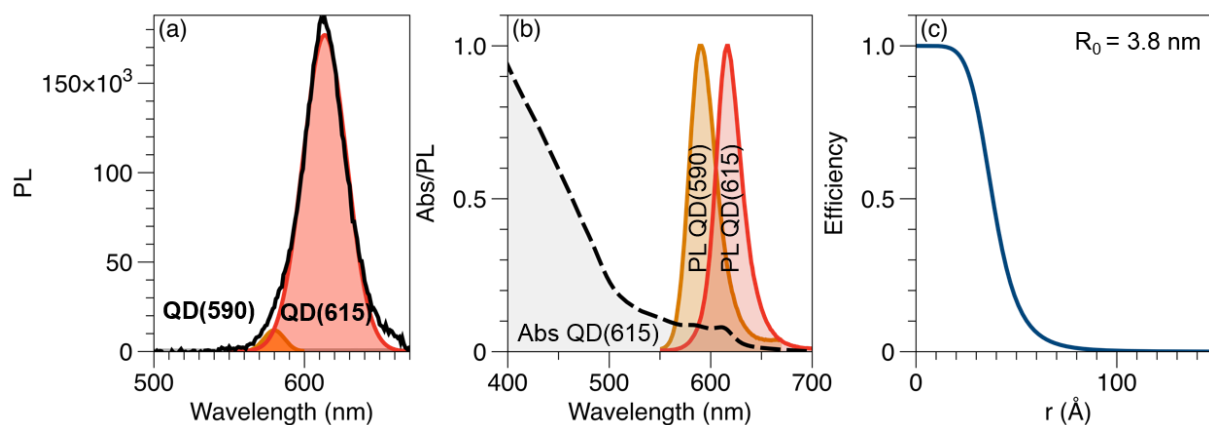


Figure 2.24: (a) Peak deconvolution for the released cluster after 22 hours of measured release ($PL_A/PL_D = 32$), (b) spectral overlap of the absorbance of the acceptor (QD(615)) with the PL of the donor (QD(590)) and acceptor and (b) FRET efficiency plot for the released cluster.

The released cluster is compared for the assembly of the QD/PSMA/DNA conjugates (figure 2.25a) and the QD/pt-DNA (figure 2.25b). The QD/PSMA/DNA and QD/pt-DNA conjugates had similar PL intensities before assembly, but the PL for released cluster for the QD/pt-DNA conjugates were 100 times higher, despite the lower donor QY values. This is indicative of increased energy transfer efficiency and the release of a higher concentration of QD clusters. The enhanced the PL_A/PL_D ratio for the QD/pt-DNA conjugates ($PL_A/PL_D = 32$) compared to the QD/PSMA/DNA conjugates ($PL_A/PL_D = 4.2$) suggests that there is an increased energy transfer efficiency. This is expected because FRET is highly dependent on distance⁴⁸ and the direct DNA attachment is expected to lead to smaller donor-acceptor distances.

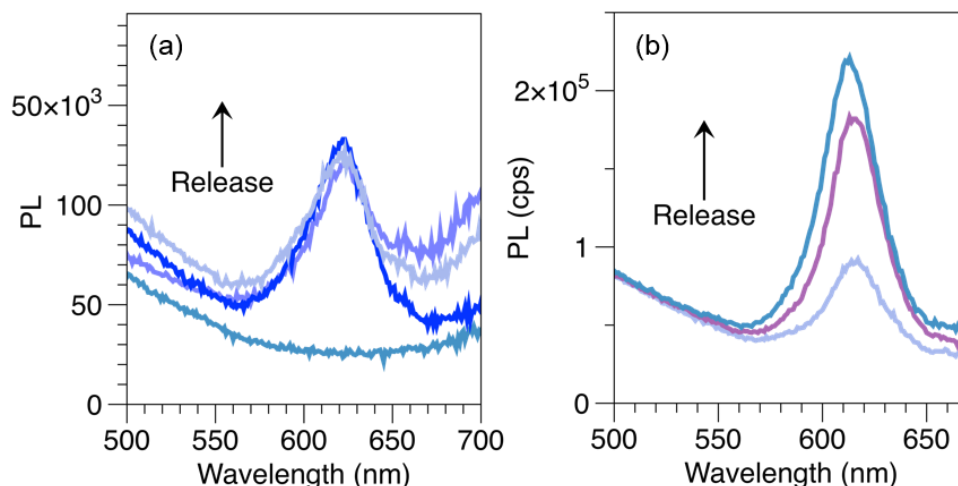


Figure 2.25: PL of the QD cluster release at the solid support for (a) QDs functionalized with DNA via polymer wrapping procedure (QD/PSMA/DNA) and (b) QDs functionalized with DNA via the direct attachment procedure (QD/pt-DNA).

This data suggests that there is an enhancement of energy transfer when the DNA is attached directly to the QD surface from the shorter donor-acceptor distances.

2.4 Conclusions

In conclusion, the stepwise DNA-mediated assembly of two color QD clusters was demonstrated. QDs were phase transferred using a polymer wrapping procedure and purified in a sucrose density gradient to remove impurities (QD aggregates, unreacted polymer conjugates) that can bind to the MB support. QDs were functionalized with DNA through EDC/NHS and click chemistry routes and assembled and released at a magnetic colloid. The QD/DNA conjugates that were prepared using click chemistry did not show release at the MB. This may be due to Cu (II) ions that were not removed during QD purification. QDs that were functionalized with DNA using the EDC/NHS coupling route were successfully assembled and released. The released QD stoichiometry could be controlled by the assembly ratios and the clusters PL intensity suggested evidence of QD-to-QD energy transfer.

To improve the energy transfer efficiency in the QD clusters, the direct attachment of DNA to the QD surface using an aqueous shell growth procedure was investigated. The shell growth and DNA functionalization was measured using gel electrophoresis, UV-Vis and PL. The cluster assembly and release at the solid support for the final conjugates was quantitatively measured using PL. The R_0 and FRET efficiency was compared for the QDs functionalized with DNA via polymer wrapping procedure (QD/PSMA/DNA) and QDs functionalized with DNA via the direct attachment procedure (QD/pt-DNA). The enhanced acceptor PL for the QD/pt-DNA conjugates indicate an increase in energy transfer efficiency. Since the DNA was directly attached to the QD surface in the QD/pt-DNA conjugates, smaller donor-acceptor distances can be achieved. These final clusters are candidates to perform as smart biosensors that can perform multiple sensing events in tandem with high sensitivity and efficiency. The clusters can also be used as unique models to probe QD-to-QD energy transfer. For all of these applications, a higher energy transfer efficiency is desired.

2.5 References

- (1) Medintz, I. L.; Uyeda, H. T.; Goldman, E. R.; Mattoussi, H. Quantum Dot Bioconjugates for Imaging, Labelling and Sensing. *Nat. Mater.* **2005**, *4* (6), 435–446.
- (2) Pinaud, F.; Clarke, S.; Sittner, A.; Dahan, M. Probing Cellular Events, One Quantum Dot at a Time. *Nat. Methods* **2010**, *7* (4), 275–285.
- (3) Han, H.; Valle, V.; Maye, M. M. Probing Resonance Energy Transfer and Inner Filter Effects in Quantum Dot–Large Metal Nanoparticle Clusters Using a DNA-Mediated Quench and Release Mechanism. *J. Phys. Chem. C* **2012**, *116* (43), 22996–23003.
- (4) Chhabra, R.; Sharma, J.; Liu, Y.; Rinker, S.; Yan, H. DNA Self-Assembly for Nanomedicine. *Adv. Drug Deliv. Rev.* **2010**, *62* (6), 617–625.
- (5) Lee, H.; Lytton-Jean, A. K. R.; Chen, Y.; Love, K. T.; Park, A. I.; Karagiannis, E. D.; Sehgal, A.; Querbes, W.; Zurenko, C. S.; Jayaraman, M.; Peng, C. G.; Charisse, K.; Borodovsky, A.; Manoharan, M.; Donahoe, J. S.; Truelove, J.; Nahrendorf, M.; Langer, R.; Anderson, D. G. Molecularly Self-Assembled Nucleic Acid Nanoparticles for Targeted in Vivo siRNA Delivery. *Nat. Nanotechnol.* **2012**, *7* (6), 389–393.
- (6) Alexander, C. M.; Maye, M. M.; Dabrowiak, J. C. DNA-Capped Nanoparticles Designed for Doxorubicin Drug Delivery. *Chem. Commun.* **2011**, *47* (12), 3418–3420.
- (7) Grzelczak, M.; Vermant, J.; Furst, E. M.; Liz-Marzán, L. M. Directed Self-Assembly of Nanoparticles. *ACS Nano* **2010**, *4* (7), 3591–3605.
- (8) Park, S. Y.; Lytton-Jean, A. K. R.; Lee, B.; Weigand, S.; Schatz, G. C.; Mirkin, C. A. DNA-Programmable Nanoparticle Crystallization. *Nature* **2008**, *451* (7178), 553–556.
- (9) Tikhomirov, G.; Hoogland, S.; Lee, P. E.; Fischer, A.; Sargent, E. H.; Kelley, S. O. DNA-Based Programming of Quantum Dot Valency, Self-Assembly and Luminescence. *Nat. Nanotechnol.* **2011**, *6* (8), 485–490.
- (10) Nykypanchuk, D.; Maye, M. M.; van der Lelie, D.; Gang, O. DNA-Guided Crystallization of Colloidal Nanoparticles. *Nature* **2008**, *451* (7178), 549–552.
- (11) Chen, C.; Wang, W.; Ge, J.; Zhao, X. S. Kinetics and Thermodynamics of DNA Hybridization on Gold Nanoparticles. *Nucleic Acids Res.* **2009**, *37* (11), 3756–3765.
- (12) Boeneman, K.; Deschamps, J. R.; Buckhout-White, S.; Prasuhn, D. E.; Blanco-Canosa, J. B.; Dawson, P. E.; Stewart, M. H.; Susumu, K.; Goldman, E. R.; Ancona, M.; Medintz, I. L. Quantum Dot DNA Bioconjugates: Attachment Chemistry Strongly Influences the Resulting Composite Architecture. *ACS Nano* **2010**, *4* (12), 7253–7266.
- (13) Tao, Y.; Lin, Y.; Ren, J.; Qu, X. Self-Assembled, Functionalized Graphene and DNA as a Universal Platform for Colorimetric Assays. *Biomaterials* **2013**, *34* (20), 4810–4817.
- (14) Medintz, I. L.; Mattoussi, H. Quantum Dot-Based Resonance Energy Transfer and Its Growing Application in Biology. *Phys. Chem. Chem. Phys.* **2008**, *11* (1), 17–45.
- (15) Liu, Y. Nanomaterials: DNA Brings Quantum Dots to Order. *Nat. Nanotechnol.* **2011**, *6* (8), 463–464.
- (16) Nie, Z.; Petukhova, A.; Kumacheva, E. Properties and Emerging Applications of Self-Assembled Structures Made from Inorganic Nanoparticles. *Nat. Nanotechnol.* **2010**, *5* (1), 15–25.
- (17) Wang, Q.; Wang, H.; Lin, C.; Sharma, J.; Zou, S.; Liu, Y. Photonic Interaction between Quantum Dots and Gold Nanoparticles in Discrete Nanostructures through DNA Directed Self-Assembly. *Chem. Commun.* **2009**, *46* (2), 240–242.

- (18) Freeman, R.; Li, Y.; Tel-Vered, R.; Sharon, E.; Elbaz, J.; Willner, I. Self-Assembly of Supramolecular Aptamer Structures for Optical or Electrochemical Sensing. *The Analyst* **2009**, *134* (4), 653.
- (19) Maye, M. M.; Nykypanchuk, D.; van der Lelie, D.; Gang, O. DNA-Regulated Micro- and Nanoparticle Assembly. *Small* **2007**, *3* (10), 1678–1682.
- (20) Mirkin, C. A.; Letsinger, R. L.; Mucic, R. C.; Storhoff, J. J. A DNA-Based Method for Rationally Assembling Nanoparticles into Macroscopic Materials. *Nature* **1996**, *382* (6592), 607–609.
- (21) Sapsford, K. E.; Algar, W. R.; Berti, L.; Gemmill, K. B.; Casey, B. J.; Oh, E.; Stewart, M. H.; Medintz, I. L. Functionalizing Nanoparticles with Biological Molecules: Developing Chemistries That Facilitate Nanotechnology. *Chem. Rev.* **2013**, *113* (3), 1904–2074.
- (22) Donegá, C. de M. Synthesis and Properties of Colloidal Heteronanocrystals. *Chem. Soc. Rev.* **2011**, *40* (3), 1512–1546.
- (23) Smith, A. M.; Nie, S. Semiconductor Nanocrystals: Structure, Properties, and Band Gap Engineering. *Acc. Chem. Res.* **2010**, *43* (2), 190–200.
- (24) Yue, Z.; Lisdat, F.; Parak, W. J.; Hickey, S. G.; Tu, L.; Sabir, N.; Dorfs, D.; Bigall, N. C. Quantum-Dot-Based Photoelectrochemical Sensors for Chemical and Biological Detection. *ACS Appl. Mater. Interfaces* **2013**, *5* (8), 2800–2814.
- (25) Kim, S. M.; Kyhm, K.; Yang, H.-S.; Hong, K. S. Optical Properties and Surface Conditions of CdSe Quantum Dots. *J. Korean Phys. Soc.* **2006**, *49*.
- (26) Alivisatos, A. P. Perspectives on the Physical Chemistry of Semiconductor Nanocrystals. *J. Phys. Chem.* **1996**, *100* (31), 13226–13239.
- (27) Sadhu, S.; Patra, A. A Brief Overview of Some Physical Studies on the Relaxation Dynamics and Förster Resonance Energy Transfer of Semiconductor Quantum Dots. *Chemphyschem Eur. J. Chem. Phys. Phys. Chem.* **2013**, *14* (12), 2641–2653.
- (28) Chou, L. Y. T.; Zagorovsky, K.; Chan, W. C. W. DNA Assembly of Nanoparticle Superstructures for Controlled Biological Delivery and Elimination. *Nat. Nanotechnol.* **2014**, *9* (2), 148–155.
- (29) Clapp, A. R.; Medintz, I. L.; Fisher, B. R.; Anderson, G. P.; Mattoussi, H. Can Luminescent Quantum Dots Be Efficient Energy Acceptors with Organic Dye Donors? *J. Am. Chem. Soc.* **2005**, *127* (4), 1242–1250.
- (30) Lees, E. E.; Nguyen, T.-L.; Clayton, A. H. A.; Mulvaney, P. The Preparation of Colloidally Stable, Water-Soluble, Biocompatible, Semiconductor Nanocrystals with a Small Hydrodynamic Diameter. *ACS Nano* **2009**, *3* (5), 1121–1128.
- (31) Jańczewski, D.; Tomczak, N.; Han, M.-Y.; Vancso, G. J. Synthesis of Functionalized Amphiphilic Polymers for Coating Quantum Dots. *Nat. Protoc.* **2011**, *6* (10), 1546–1553.
- (32) Yu, W. W.; Chang, E.; Falkner, J. C.; Zhang, J.; Al-Somali, A. M.; Sayes, C. M.; Johns, J.; Drezek, R.; Colvin, V. L. Forming Biocompatible and Nonaggregated Nanocrystals in Water Using Amphiphilic Polymers. *J. Am. Chem. Soc.* **2007**, *129* (10), 2871–2879.
- (33) Anderson, R. E.; Chan, W. C. W. Systematic Investigation of Preparing Biocompatible, Single, and Small ZnS-Capped CdSe Quantum Dots with Amphiphilic Polymers. *ACS Nano* **2008**, *2* (7), 1341–1352.
- (34) Han, H.; Zylstra, J.; Maye, M. M. Direct Attachment of Oligonucleotides to Quantum Dot Interfaces. *Chem. Mater.* **2011**, *23* (22), 4975–4981.

- (35) Alam, R.; Fontaine, D. M.; Branchini, B. R.; Maye, M. M. Designing Quantum Rods for Optimized Energy Transfer with Firefly Luciferase Enzymes. *Nano Lett.* **2012**, *12* (6), 3251–3256.
- (36) Schieber, C.; Bestetti, A.; Lim, J. P.; Ryan, A. D.; Nguyen, T.-L.; Eldridge, R.; White, A. R.; Gleeson, P. A.; Donnelly, P. S.; Williams, S. J.; Mulvaney, P. Conjugation of Transferrin to Azide-Modified CdSe/ZnS Core–Shell Quantum Dots Using Cyclooctyne Click Chemistry. *Angew. Chem. Int. Ed.* **2012**, *51* (42), 10523–10527.
- (37) Zylstra, J.; Amey, J.; Miska, N. J.; Pang, L.; Hine, C. R.; Langer, J.; Doyle, R. P.; Maye, M. M. A Modular Phase Transfer and Ligand Exchange Protocol for Quantum Dots. *Langmuir* **2011**, *27* (8), 4371–4379.
- (38) Zhang, C.; Macfarlane, R. J.; Young, K. L.; Choi, C. H. J.; Hao, L.; Auyeung, E.; Liu, G.; Zhou, X.; Mirkin, C. A. A General Approach to DNA-Programmable Atom Equivalents. *Nat. Mater.* **2013**, *12* (8), 741–746.
- (39) Doane, T. L.; Alam, R.; Maye, M. M. Functionalization of Quantum Rods with Oligonucleotides for Programmable Assembly with DNA Origami. *Nanoscale* **2015**, *7* (7), 2883–2888.
- (40) Ma, N.; Kelley, S. O. DNA-Based Programming of Quantum Dot Properties. *Wiley Interdiscip. Rev. Nanomed. Nanobiotechnol.* **2013**, *5* (1), 86–95.
- (41) Deng, Z.; Samanta, A.; Nangreave, J.; Yan, H.; Liu, Y. Robust DNA-Functionalized Core/Shell Quantum Dots with Fluorescent Emission Spanning from UV–vis to Near-IR and Compatible with DNA-Directed Self-Assembly. *J. Am. Chem. Soc.* **2012**, *134* (42), 17424–17427.
- (42) Claridge, S. A.; Liang, H. W.; Basu, S. R.; Fréchet, J. M. J.; Alivisatos, A. P. Isolation of Discrete Nanoparticle–DNA Conjugates for Plasmonic Applications. *Nano Lett.* **2008**, *8* (4), 1202–1206.
- (43) Fu, A.; Micheel, C. M.; Cha, J.; Chang, H.; Yang, H.; Alivisatos, A. P. Discrete Nanostructures of Quantum Dots/Au with DNA. *J. Am. Chem. Soc.* **2004**, *126* (35), 10832–10833.
- (44) Pellegrino, T.; Sperling, R. A.; Alivisatos, A. P.; Parak, W. J. Gel Electrophoresis of Gold-DNA Nanoconjugates. *BioMed Res. Int.* **2008**, *2007*, e26796.
- (45) Li, J. J.; Wang, Y. A.; Guo, W.; Keay, J. C.; Mishima, T. D.; Johnson, M. B.; Peng, X. Large-Scale Synthesis of Nearly Monodisperse CdSe/CdS Core/Shell Nanocrystals Using Air-Stable Reagents via Successive Ion Layer Adsorption and Reaction. *J. Am. Chem. Soc.* **2003**, *125* (41), 12567–12575.
- (46) Yu, W. W.; Qu, L.; Guo, W.; Peng, X. Experimental Determination of the Extinction Coefficient of CdTe, CdSe, and CdS Nanocrystals. *Chem. Mater.* **2003**, *15* (14), 2854–2860.
- (47) Sun, D.; Gang, O. DNA-Functionalized Quantum Dots: Fabrication, Structural, and Physicochemical Properties. *Langmuir* **2013**, *29* (23), 7038–7046.
- (48) Hurst, S. J.; Lytton-Jean, A. K. R.; Mirkin, C. A. Maximizing DNA Loading on a Range of Gold Nanoparticle Sizes. *Anal. Chem.* **2006**, *78* (24), 8313–8318.
- (49) Lakowicz, J. *Principles of Fluorescence Spectroscopy*, Second.; Kluwer Academic/Plenum Publishers: New York, NY, 1999.
- (50) Gong, P.; Grainger, D. W. Comparison of DNA Immobilization Efficiency on New and Regenerated Commercial Amine-Reactive Polymer Microarray Surfaces. *Surf. Sci.* **2004**, *570* (1–2), 67–77.

- (51) Hepel, M.; Stobiecka, M.; Peachey, J.; Miller, J. Intervention of Glutathione in Pre-Mutagenic Catechol-Mediated DNA Damage in the Presence of copper(II) Ions. *Mutat. Res. Mol. Mech. Mutagen.* **2012**, 735 (1–2), 1–11.
- (52) Zhang, Y.; Zhang, H.; Guo, X.; Wang, H. L-Cysteine-Coated CdSe/CdS Core-Shell Quantum Dots as Selective Fluorescence Probe for copper(II) Determination. *Microchem. J.* **2008**, 89 (2), 142–147.
- (53) Mork, A. J.; Weidman, M. C.; Prins, F.; Tisdale, W. A. Magnitude of the Förster Radius in Colloidal Quantum Dot Solids. *J. Phys. Chem. C* **2014**, 118 (25), 13920–13928.
- (54) Halivni, S.; Sitt, A.; Hadar, I.; Banin, U. Effect of Nanoparticle Dimensionality on Fluorescence Resonance Energy Transfer in Nanoparticle–Dye Conjugated Systems. *ACS Nano* **2012**, 6 (3), 2758–2765.
- (55) Dennis, A. M.; Rhee, W. J.; Sotito, D.; Dublin, S. N.; Bao, G. Quantum Dot–Fluorescent Protein FRET Probes for Sensing Intracellular pH. *ACS Nano* **2012**, 6 (4), 2917–2924.
- (56) Mou, J.; Czajkowsky, D. M.; Zhang, Y.; Shao, Z. High-Resolution Atomic-Force Microscopy of DNA: The Pitch of the Double Helix. *FEBS Lett.* **1995**, 371 (3), 279–282.
- (57) Spillmann, C. M.; Buckhout-White, S.; Oh, E.; Goldman, E. R.; Ancona, M. G.; Medintz, I. L. Extending FRET Cascades on Linear DNA Photonic Wires. *Chem. Commun.* **2014**, 50 (55), 7246.

Chapter 3

Investigating the Colloidal Stability and Energy Transfer of Quantum Rod Bioconjugates

In Chapter 2, I discussed the self-assembly of QD clusters, where the QD energy acceptor ability is limited by the broad absorption profile that causes co-excitation in QD FRET pairs. In this chapter, a bioluminescent protein was attached to a quantum rod (QR) to generate QR emission through bioluminescence resonance energy transfer (BRET), which eliminated the need for an external excitation source. Previous experiments showed that quantum rods with rod-in-rod microstructures are the most efficient BRET acceptors; however, the colloidal stability was not optimized. Here, the colloidal stability was investigated and improved, and the nature of energy transfer was investigated.

3.1 Introduction

Many species have independently evolved to be bioluminescent, including bacteria, coelenterates, and beetles.^{1,2} Although the genes that are responsible for bioluminescence between the different species are unrelated, they all involve the reaction of molecular oxygen with a substrate, like luciferin (LH₂), and an enzyme, like luciferase, to produce photons.¹⁻⁸ The bioluminescence produced can be transferred to fluorescent proteins or inorganic fluorescent nanocrystals, such as quantum dots (QDs) and quantum rods (QRs) through bioluminescence resonance energy transfer (BRET).⁹⁻¹⁷ Thus, these inorganic materials are illuminated without an external light source, which is the common route. BRET to fluorescent proteins and QDs have been studied for self-illuminated photodynamic therapy,¹⁸ biological detection and imaging,^{19,20} and light-harvesting devices.²¹ For example, BRET was used to study the interactions between a

G protein coupled receptor and the neurotransmitter, norepinephrine, to determine if oligomerization occurred upon receptor binding.²⁰ The BRET was studied as a function of the stoichiometry between a fluorescently tagged G protein coupled receptor to the luciferase fused norepinephrine and a linear relationship indicated that oligomerization did not occur.²⁰ In another report by Yao et al, the sea pansy's bioluminescent protein, *Renilla* luciferase, was conjugated to QDs for the detection of matrix metalloproteinases, a peptide biomarker for in vivo cancer tumor detection.¹⁹ In these studies, a hexahistagged substrate for the metalloproteinase was genetically fused to a *Renilla* luciferase mutant. In the absence of the peptide, Ni²⁺ coordinated the hexahistagged protein to a carboxylate functionalized QD and BRET occurred. In the presence of the metalloproteinase, the hexahistag was cleaved off of the *Renilla* luciferase to prevent coordination to the QD and BRET did not occur.¹⁹

Using bioluminescence or BRET prevents photobleaching as well as issues that arise when light penetrates tissues during external excitation, including high light scattering and tissue autofluorescence.^{14,15,18,22,23} Another issue that BRET can overcome is the co-excitation that occurs with QR or QD energy acceptors in FRET pairs.¹² Coexcitation occurs when both the energy donor and acceptor are excited. This increases the complexity of energy transfer analysis since the acceptor emission is from radiative excitation and non-radiative energy transfer. A bioluminescent donor in a pure BRET system generate acceptor emission that is only possible through non-radiative energy transfer. The energy transfer efficiency for BRET and FRET has been found to be dependent on the donor-acceptor distances, QD shape, dimensionality and microstructure. For example, QRs with rod-in-rod morphology were found to be more efficient FRET acceptors than dot-in-dot QDs and dot-in-rod QRs when coupled to organic dye donors.²⁴ Previous experiments in our lab were consistent with this finding, where rod-in-rod QRs with an aspect ratio (l/w) of

around 3 were the most efficient BRET acceptors, with BRET ratios ($BR = PL_A/PL_D$) as high as 44.¹¹⁻¹³ The increased energy accepting abilities of rod-in-rod QRs were attributed to the higher QR surface area that can accommodate more protein molecules as long as the protein molecules remain relatively close to the core ($r \geq R_0$) where QR emission originates. Other QR properties that can contribute to their increased energy accepting abilities include the longer lifetimes, broader absorption profiles and aspect ratio tuneability.²⁵ Previous experiments also found that the optimum protein loading for the highest BR is at lower protein loading ($L = [Ppy] : [QR] = 5$). This is counter intuitive since QRs have a higher surface area to accommodate more donors, which should lead to an increase in energy transfer efficiency.^{24,26} It was hypothesized that the reduced BR was due to either preferential Ppy binding at defect rich interfaces close to the core, lower accessibility to the substrate at higher coverage or cooperative effects that quench bioluminescence.¹¹ Recently, it was reported that over-labeling biomolecules with chromophores leads to decreased sensitivity due to the resonance energy transfer migration between chromophores and background fluorescence.²⁷ In these studies, gold nanoparticles (AuNPs) were used to limit the FRET between a chromophore, fluorescein, and a biomolecule, cytochrome c, to prevent resonance energy transfer migration and autofluorescence, which resulted in lower detection limits for cytochrome c.²⁷ This work demonstrates the importance of keeping energy transfer an intramolecular process.

In this chapter, CdSe/CdS QRs were functionalized with a green thermally stable North American firefly luciferase, *Photinus pyralis* (Ppy).²⁸ Ppy bioluminescence is one of the brightest in nature, with QYs as high as 41%.²⁹ Native Ppy emits yellow-green light ($\lambda_{em} = 560$ nm) at pH = 7.8 but luciferase and luciferin can both be engineered to create emission at different wavelengths, increasing the breadth of energy donor capabilities.²⁸⁻³² In these studies, QRs

underwent a histidine (His) mediated phase transfer followed by an additional ligand exchange with N-terminus hexahistidine tagged (6xHis) Ppy, which has been shown to coordinate directly to QD surfaces.^{11–13,33} One challenge we encountered in previous studies was the long-term instability of the BRET nanoconjugates. Here, we address this by investigating the use of different QR capping ligands. By changing the ligand that imparted water solubility from His to glutathione (GSH), the BRET signal remained stable over the course of one week.

To investigate how the protein binds to the QR surface, QRs were immobilized onto glass substrates. Monolayers of QDs and QRs have been investigated for a wide range of applications in thin film and microchip technologies.^{34,35} Glass substrates are normally unreactive, hydrophilic inorganic surfaces, but different methods have been employed to chemically attach molecules to the surface, including the chemical vapor and liquid phase deposition of organosilanes. Organosilanes are organic compounds that contain carbon silicon bonds and can be used as coupling agents to glass to impart functionality and reactivity.^{36–38} Other deposition methods, such as the Langmuir Blodgett technique, result in monolayers that are physisorbed rather than chemically adsorbed on the surfaces. In this chapter, glass substrates were silanized with 3-mercaptopropyltrimethoxysilane (MPTS) through liquid phase deposition and QR/His conjugates were immobilized to the substrate through a thiol linkage. The QRs were then functionalized with Ppy and imaged under confocal and AFM.

3.2 Experimental

3.2.1 Chemicals

Cadmium oxide (CdO, 99.99%), sulfur (S, 100 mesh), Zn Acetate (ZnAc, 99.99%), Methylphosphonic acid (MPA, 98%), Trioctylphosphine oxide (TOP, 97%), 1-octadecene (ODE, 90%), oleylamine (OAm, 70%), oleic acid (OA, 99%), sodium phosphate monobasic monohydrate ($\text{NaH}_2\text{PO}_4 \cdot \text{H}_2\text{O}$, 98.0-102.0%), sodium phosphate dibasic hepta-hydrate ($\text{Na}_2\text{HPO}_4 \cdot 7\text{H}_2\text{O}$, 98.0-102.0%), L-Histidine (His, 99%), (11-Mercaptoundecyl)tetra(ethylene glycol) (PEG-SH), thioglycolic acid (TGA), reduced L-glutathione (GSH, 99%), and 3-mercaptopropyltrimethoxysilane (MPTS, 95%) were purchased from Sigma Aldrich. Trioctylphosphine Oxide (TOPO, 90%), Octadecylphosphonic acid (ODPA, 97%), Tetradecylphosphonic acid (TDPA, 97%), mercaptophosphonic acid (MPPS) and hexylphosphonic acid (HPA, 97%) were purchased from Strem Chemicals, Selenium Powder (Se, 200 mesh, 99.999%) was purchased from Alpha Aesar, Agarose NA was from GE Healthcare.

3.2.2 Synthesis and Functionalization of QRs

Synthesis of CdSe/CdS QRs. First, TOPO was purified through recrystallization in acetonitrile and dried under vacuum. CdSe rod cores were prepared by heating 0.5 mmoles CdO, 7.8 mmoles TOPO, 0.7 mmoles ODPA, 0.12 mmoles MPPA and 2 mL ODE to 150 °C under vacuum. After 1 hour, the solution was heated to 330 °C under Ar until clear. The temperature was increased to 365 °C, where 1 mL TOP was injected. Once the temperature stabilized, 0.07 g Se in 0.5 mL TOP was injected and the solution was annealed for 10 minutes. The final phosphonic acid capped QR cores were cleaned via acetone precipitation and resuspended in toluene. The CdSe core surface was passivated with a CdS shell using a seeded initiation route. Briefly, 8.7 nmoles of CdSe QR cores were resuspended in a warm solution of 1 mL TOP and 0.06 g Sulfur.

Meanwhile, 0.25 mmol CdO, 7.8 mmol TOPO, 0.25 mmol HPA, 0.4 mmol ODPA and 2 mL ODE were heated to 150 °C under vacuum for 1 hour. The solution was then heated under Ar to 330 °C until clear then the temperature was increased to 365 °C when 1 mL TOP was added. After the temperature stabilized at 365 °C, the core solution was swiftly injected and annealed for 10 minutes. The final CdSe/CdS QRs were cleaned via acetone precipitation and resuspended in toluene.

Histidine and Glutathione Mediated Phase Transfer. Organic soluble QRs were transferred to aqueous conditions using a ligand exchange procedure.^{39,40} The QRs were cleaned using an acetone precipitation and resuspended in chloroform. For histidine capped QRs, a 0.1 M His solution in a 1 : 4 water : basic methanol mixture was added to the QRs in 40,000-100,000 molar excess. The solution was vortexed and immediately separated into a clear and colorless chloroform layer and a colored aqueous solution at the top. The aqueous soluble QRs were removed from the solution and back extracted with chloroform 4-5 times. Excess ligands were removed by precipitating the QRs in a methanol/acetone mixture. The final QR/His conjugates were resuspended in borate buffer (pH = 8.4). For GSH capped QRs, a similar protocol was followed except the QR/GSH solution was reacted for 2 hours at room temperature.

QR conjugation with TGA or PEG-SH. To functionalize the QR surface with TGA or PEG-SH, QR/His was incubated with a 5000 molar excess of ligand (pH=12) at 50 °C for 2 hours. Excess ligands were removed using a 100 kDa spin filter and the final QR conjugates were suspended in borate buffer (pH=8.4).

QR/Ppy Conjugation. To assemble the QR/Ppy nanoconjugates, the 6x histagged Ppy was incubated with His-functionalized or GSH-functionalized QRs for 20 minutes on ice prior to BRET analysis.

3.2.3 BRET Measurement and Analysis. In a typical BRET experiment, the QR/Ppy nanoconjugates ($[QR]=150-500$ nM) were quickly added to a mixture of 100 μ L of 91 μ M LH₂ and 30 μ L of 8.66 mM Mg-ATP in 25 mM gly-gly buffer (pH 7.8) in a 96 well plate. For the control experiments involving imidazole, QR/GSH was incubated with 6xhistagged Ppy for 20 minutes. The BRET was measured for 5 scans. A 5 μ L aliquot of imidazole ($[imidazole]:[QR]=100,000$) was quickly added to the solution and the bioluminescence emission was measured immediately.

3.2.4 QR Immobilization on Glass Substrates. Glass slides were cleaned with a 1 : 1 mixture of HCl : Methanol for 30 minutes. The slides were washed with water and dried under Ar flow. The glass substrates were dipped in a Piranha solution (3 parts concentrated H₂SO₄ to 1 part 30% H₂O₂) and then washed copiously with deionized water and dried under Ar flow. To attach MPTS, dried glass slides were placed in a 2.5% (w/v) MPTS solution in toluene. After 2 hours, the slides were washed with toluene, dried under Ar flow and placed in an 80 °C oven for 15-18 hours.³⁶⁻³⁸ The glass slides were cleaned in toluene and dried under Ar flow. To attach organic soluble QDs, glass slides were incubated with 1.5×10^{-9} to 1.5×10^{-10} moles of QDs in toluene for 7-20 hours. The slides were then washed with toluene, dried under Ar flow and stored in toluene. For aqueous attachment of QDs, the glass was incubated in a 1.5×10^{-10} M QD/His solution in borate buffer (pH = 7.8) for 7-15 hours. The glass substrates were washed with deionized water, dried under Ar flow and stored in borate buffer in the refrigerator. To attach Ppy, the glass containing QD/His were submerged into a solution of Ppy overnight at 4 °C.

3.2.5 Instrumentation

UV-Vis Spectroscopy (UV-Vis). See section 2.2.5

Dynamic Light Scattering (DLS). See section 2.2.5

Fourier Transform Infrared Spectroscopy (FTIR). See section 2.2.5

Photoluminescence (PL). See section 2.2.5

Polarized Photoluminescence Excitation Spectroscopy. A photoselection experiment was performed where, in an ensemble solution of randomly oriented QRs, only fluorophores of the correct orientation are excited by a polarized excitation source.⁴¹⁻⁴³ Polarization experiments were performed on a Horiba Jobin Yvon Fluoromax-4 photon counting spectrophotometer equipped with a 150 W xenon white light excitation source, computer controlled monochromator and a polarizer. The polarization and anisotropy as a function of excitation wavelength was measured. The emission wavelength was held constant at a wavelength 5-10 nm red shifted from the QR emission maximum.

Bioluminescence (BL). All BRET measurements were obtained on a Varian Cary-Eclipse spectrophotometer in bioluminescence/chemiluminescence mode with a 96 well plate reading accessory with the emission source blocked. Bioluminescence scans were performed in a white well plate and spectra were collected every 15 seconds for 7.5 minutes. The emission spectra were manually corrected for source intensity and detector sensitivity by comparing the relative emission intensities with the corrected detector on the Fluoromax 4 spectrophotometer.

Atomic Force Microscopy (AFM). AFM images were acquired with a SiN₂ tip in tapping mode. The samples were placed on a mica substrate. First, mica substrates were cleaved with tape to obtain a clean, flat surface. Then, 100 mM MgCl₂ was drop casted and wicked off followed by the sample, which was also drop casted and wicked off.

Transmission Electron Microscopy (TEM). TEM measurements were performed on a JEOL 2000EX instrument operated at 100 kV with a tungsten filament (SUNY-ESF, N.C. Brown

Center for Ultrastructure Studies). TEM measurements were performed by Lili Karam. Particle size and aspect ratio were analyzed manually using CorelDraw on populations of at least 50 counts.

Confocal Microscopy. Confocal images were collected on a Zeiss LSM 710 Inverted Confocal Microscope with an argon laser with a 22 μm pinhole. The samples were excited at 405 nm (Diode laser, 30 mW), 488 nm (Ar laser, 25 W), 543 nm (HeNe laser, 1.2 mW) and 633 nm (HeNe laser, 5 mW) based on the QD emission. Light was focused through a Plan-Apochromat 1.4 NA/63x DIC M27 oil immersion objective.

3.2.6 Calculations

Quantum Dot Concentration. See section 2.2.4.

Quantum Rod Concentration. The extinction coefficient of the CdSe QRs based on the optical absorption at 350 nm was calculated using Equation 3.1 as determined by Shaviv *et al.*⁴⁴

$$\epsilon_{350} = (0.34 \times 10^{28})V \quad (3.1)$$

where ϵ_{350} is the extinction coefficient at 350 nm and V is the average volume of the CdSe cores (in cm^{-3}) as determined by TEM.

Quantum Yield (QY). See section 2.2.4

Förster Resonance Energy Transfer (FRET). See section 2.2.4.

BRET Ratios (BR). The BR was calculated by taking the ratio of the signal from the Ppy and the QR, as shown in Equation 3.2.

$$BR = \frac{PL_A}{PL_D} \quad (3.2)$$

Where PL_D and PL_A are the integrated emission of the Ppy and acceptor, respectively. The integrated emission was measured using a multi peak-fitting package in IgorPro.

Fluorescence Polarization. Polarization (pol) is calculated using Equation 3.3.⁴¹

$$pol = \frac{I_{\parallel} - I_{\perp}}{I_{\parallel} + I_{\perp}} \quad (3.3)$$

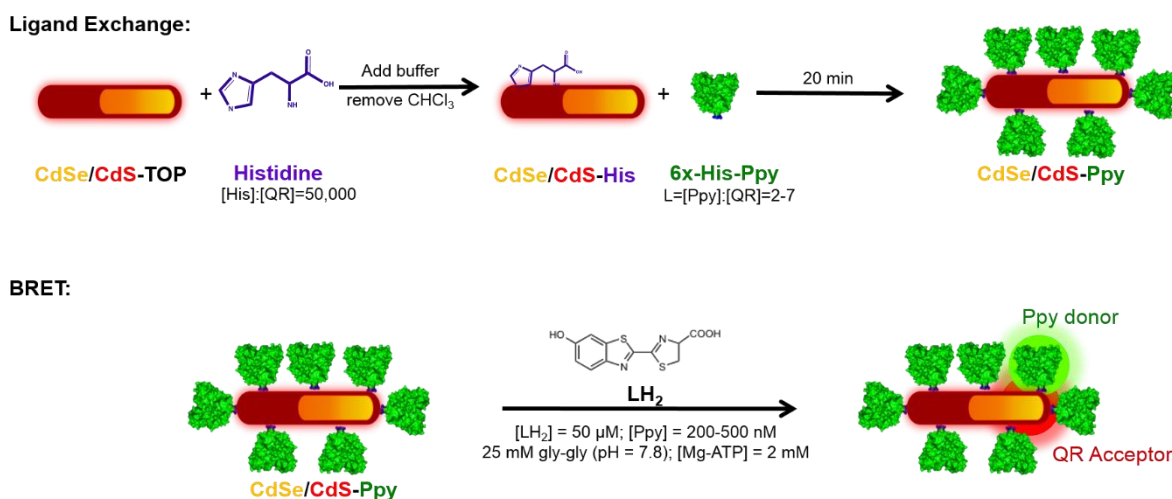
where I_{\parallel} and I_{\perp} are the parallel and perpendicular components of light, respectively.

Protein Charge and Hydrophobicity. MacPyMol was used to calculate the charge distribution and hydrophobicity for the North American firefly (PDB: 3IEP). The surface charge was calculated using vacuum electrostatics protein contact potential and the hydrophobicity was calculated using an open source code that changed the color of the amino acid residues based on the hydrophobicity.

3.3 Results and Discussion

3.3.1 Improving QR/Ppy Colloidal Stability

To create self-illuminating QR bioconjugates, hydrophobic CdSe/CdS QRs were phase transferred into buffers following a histidine mediated phase transfer protocol to create QR/His. The QRs were then conjugated with hexahistidine tagged Ppy to create QR/His/Ppy. The hexahistidine tag displaces the His layer and directly attaches the Ppy to the QR surface,¹³ providing short QR-Ppy distances for an increased energy transfer efficiency. Firefly luciferin (LH₂) and Mg-ATP is then added and the Ppy converts the chemical energy and non-radiatively transfers the energy to the QRs in the form of BRET, as shown in Scheme 3.1.¹¹



Scheme 3.1: Functionalization of QRs with Ppy for BRET studies

BRET efficiency was found to be highly dependent on QR microstructure,¹¹ so QRs with rod-in-rod morphology were synthesized using an organometallic route to synthesize the CdSe cores followed by seed-mediated growth approach to create CdSe/CdS. Figure 3.1 shows the TEM and optical spectra for a typical QR sample. As shown in the TEM micrographs, the QR length (*l*) increased from 17.1 to 44.8 nm and the width (*w*) increased from 4.3 to 8.7 nm after shell growth,

indicating there is CdS growth over the entire CdS seed. This is important because the CdS shell improves the fluorescence QY by protecting the core from the surrounding environment. The final CdSe/CdS QR(665) reveals an aspect ratio (l/w) of 5.2 ± 1.7 . The fluorescence polarization showed a slight increase in polarization (pol) from 0.17 to 0.20 upon growth of the CdS shell. Since the emission originates from the core, a slight increase in polarization after shell growth is possibly due to the slight change in exciton confinement. A control experiment of an unpolarized organic dye, rhodamine 6g (rh6g), had a measured pol ≈ 0 , as shown in Figure 3.1c. Both BRET and fluorescence polarization has been found to be strongly dependent on QR aspect ratio.^{11,41,42}

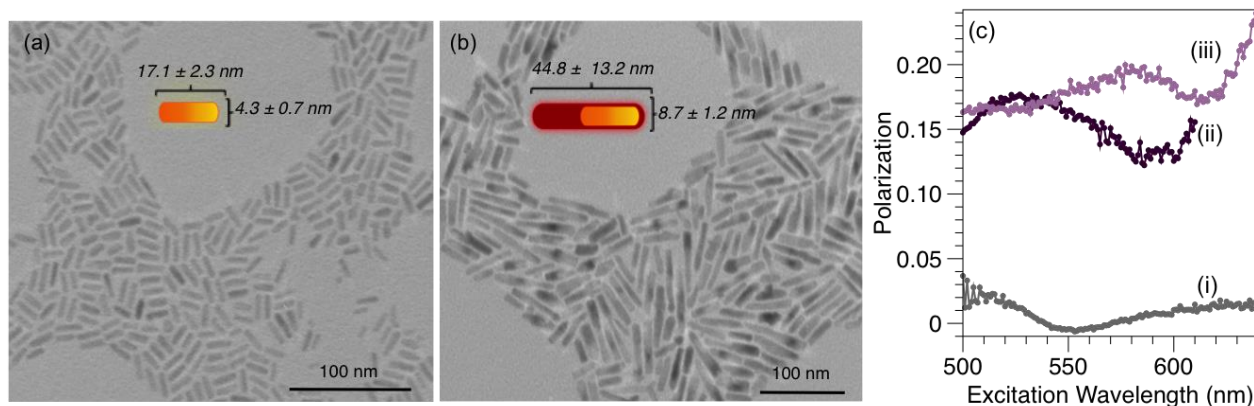


Figure 3.1: (a) TEM of CdSe QR core and (b) TEM of CdSe/CdS QR(665) core/shell; (c) ensemble fluorescence polarization measurements of (i) Rhodamine 6G, (ii) core and (iii) core/shell QRs.

Figure 3.2 shows the results from a typical BRET experiment for QR(665) that had a BR of 3 and a Förster distance of 10 nm. In this system, there is no direct external excitation, so the QR emission is due to the energy transfer from Ppy. The BR and signal intensity is dependent on the Ppy molar loading ratio, QD microstructure and acceptor QY.¹¹

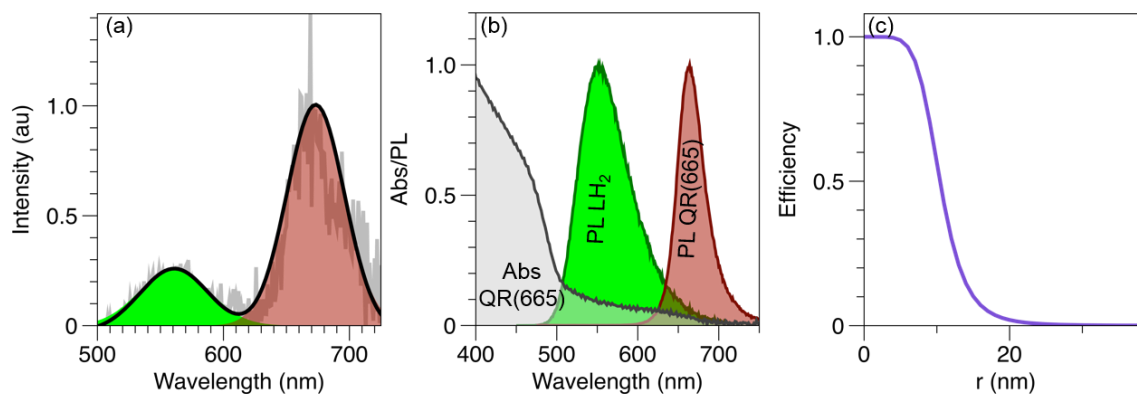


Figure 3.2: (a) BRET measurement for QR(665) (BR = 3); (b) spectral overlap ($J = 1.3 \times 10^{-11} \text{ cm}^{-6}$), (c) energy transfer efficiency plot ($R_0 = 10 \text{ nm}$).

The dependence of the long-term stability on the BR was investigated by measuring the BRET of QR/His/Ppy at different Ppy-QR incubation times. As shown in Figure 3.3, the BRET signal of these conjugates is almost completely quenched after 24 hours and the BR decreased from 27 after 20 minutes to 1.2 after 24 hours. The bioluminescence of Ppy alone retains about 65% of its original value, so the majority of the instability is most likely from the QR/His/Ppy conjugates.

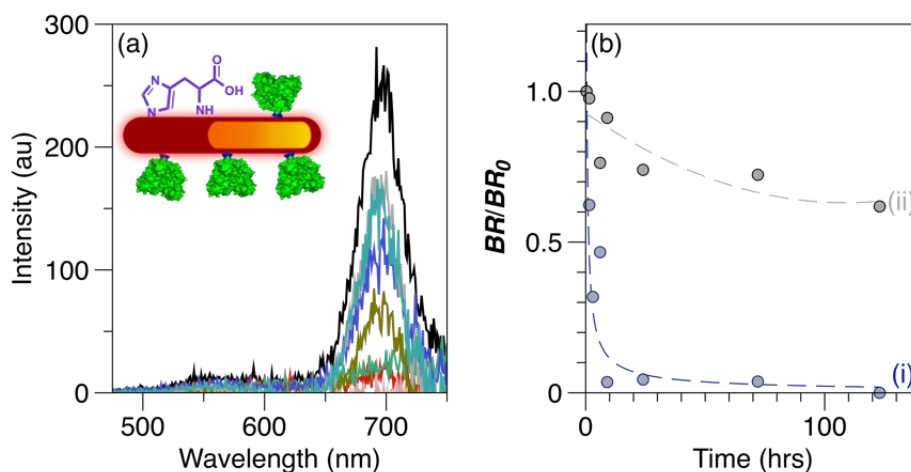


Figure 3.3: BRET stability of (a) QR/His/Ppy conjugates over time; (b) scatter plot of (i) QR/His/Ppy BRET stability and (ii) Ppy bioluminescence stability over time.

We hypothesize that this loss was due to decreased electrostatic repulsions between the QR/His/Ppy conjugates after the ligand exchange. Before Ppy conjugation, the carboxylate moieties on the His ligands provide the electrostatic repulsions between QRs to prevent them from aggregating. After Ppy conjugation, the solvent exposed amino acids on the Ppy provide the colloidal stability but there are many bulky, hydrophobic residues on the surface that can decrease stability.⁴⁵ To test this, the His layer was displaced by either thioglycolic acid (TGA) or glutathione (GSH) prior to Ppy conjugation, and the BRET was studied at 20 mins and 360 mins as shown in Figure 3.4.

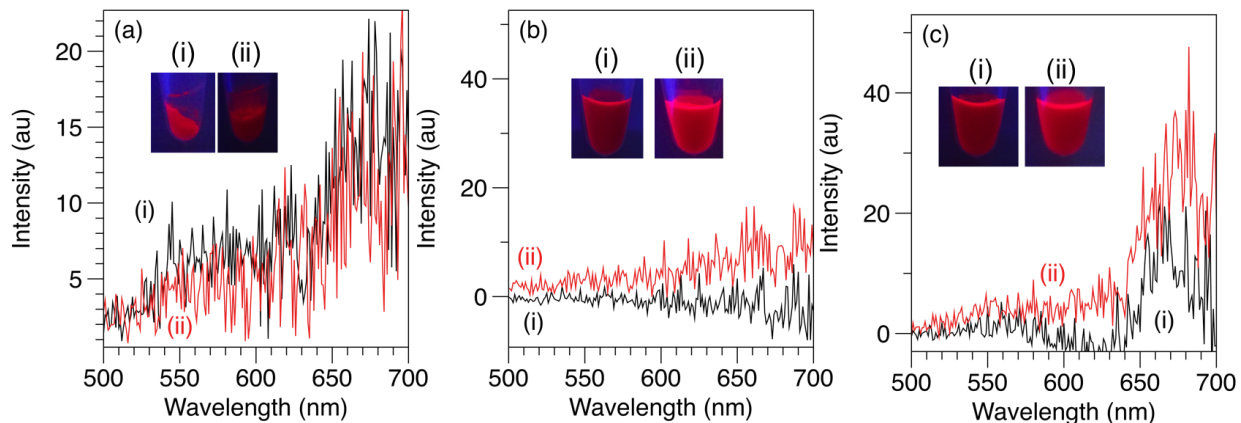


Figure 3.4: BRET at (i) 20 mins and (ii) 360 mins of (a) QR/His/Ppy, (b) QR/TGA/Ppy and (c) QR/GSH/Ppy. Inset: UV illuminated images of the solutions prior to BRET measurements.

Figure 3.4a shows that the QR/His/Ppy conjugate still had a BRET signal after 360 minutes but the QR conjugates crashed out of solution even prior to the 20 minute BRET scan. The QR/TGA/Ppy solution in Figure 3.4b never showed a BRET signal but the solution remained suspended for the entire experiment. In Figure 3.4c, the BRET signal for QR/GSH/Ppy remained stable for 360 minutes and the colloidal solution remained suspended. Since the QR/GSH/Ppy was the most stable nanoconjugate, the BRET for this system was further investigated.

The nature of the binding of GSH on the QR surface was investigated using FTIR, as shown in Figure 3.5.

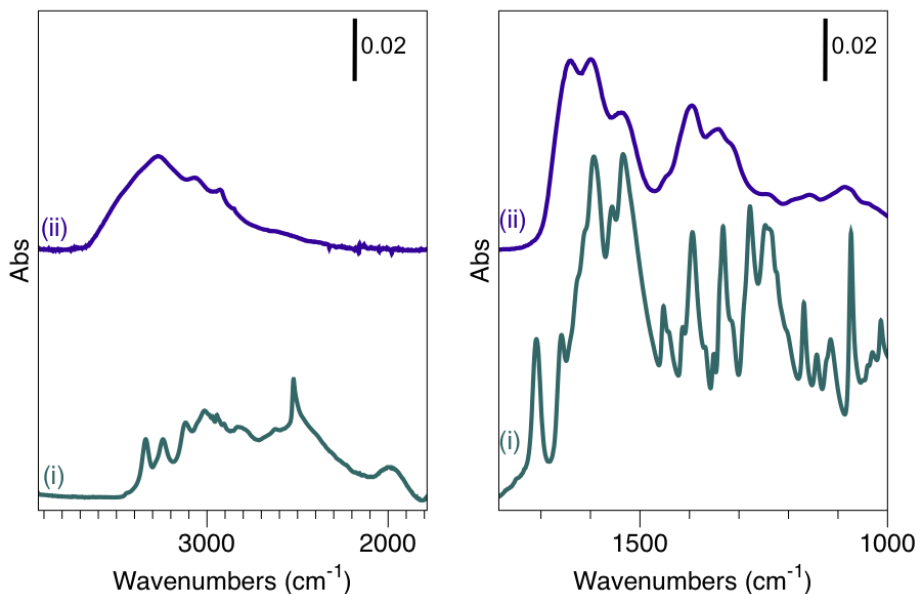


Figure 3.5: FTIR of (i) GSH and (ii) QR/GSH.

The FTIR of free GSH compared to QR/GSH shows that the peak for the thiol stretch, around $\nu = 2520 \text{ cm}^{-1}$, decreases, indicating that the GSH binds to the QR through the thiol. The disappearance of the peak around 1710 cm^{-1} for the carboxylic acid C-O stretch could be due to alcohol deprotonation at the basic pH or interactions with the QR surface. Amines have also been found to bind to the QR surface, but the characteristic amine peaks between $3350\text{-}3250 \text{ cm}^{-1}$ become convoluted, which is characteristic for molecules bound to a surface. Table 3.1 summarizes the characteristic FTIR vibrations for Figure 3.5.

Table 3.1: FTIR Vibrations	
Vibration	ν
N-H stretch	$3340 \text{ cm}^{-1}, 3240 \text{ cm}^{-1}$
OH stretch (COOH)	3120 cm^{-1}
S-H stretch	2520 cm^{-1}
C = O stretch (COOH)	1710 cm^{-1}
C = O stretch (amide)	1660 cm^{-1}

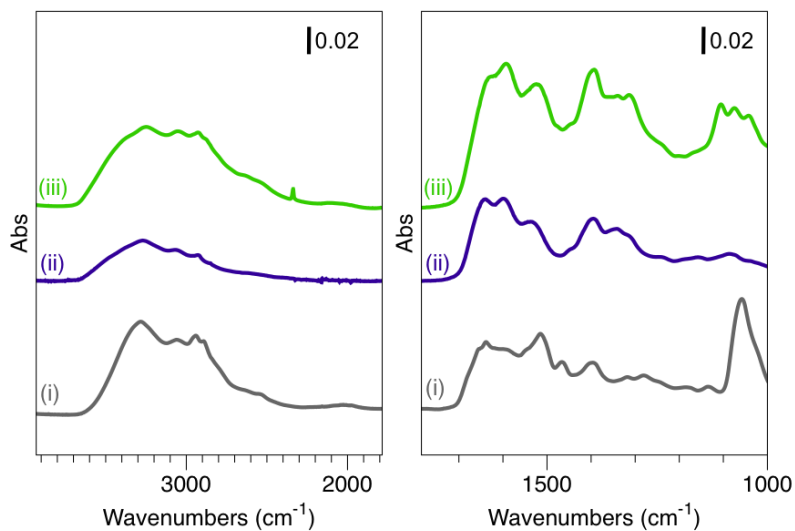


Figure 3.6: FTIR of (i) Ppy, (ii) QR/GSH, (iii) QR/GSH/Ppy

Figure 3.6 shows that after Ppy was bound to the QR/GSH nanoconjugates, the thiol peak in the FTIR around 2500 cm^{-1} reappears. This indicates that the Ppy displaces GSH on the QR surface. Table 3.2 shows the FTIR vibrations for the major peaks in Figure 3.6.

Table 3.2: FTIR Vibrations

Vibration	ν
N-H stretch	3340 cm^{-1} , 3240 cm^{-1}
OH stretch (COOH)	3120 cm^{-1}
S-H stretch	2520 cm^{-1}
C = O stretch (COOH)	1710 cm^{-1}
C = O stretch (amide)	1660 cm^{-1}

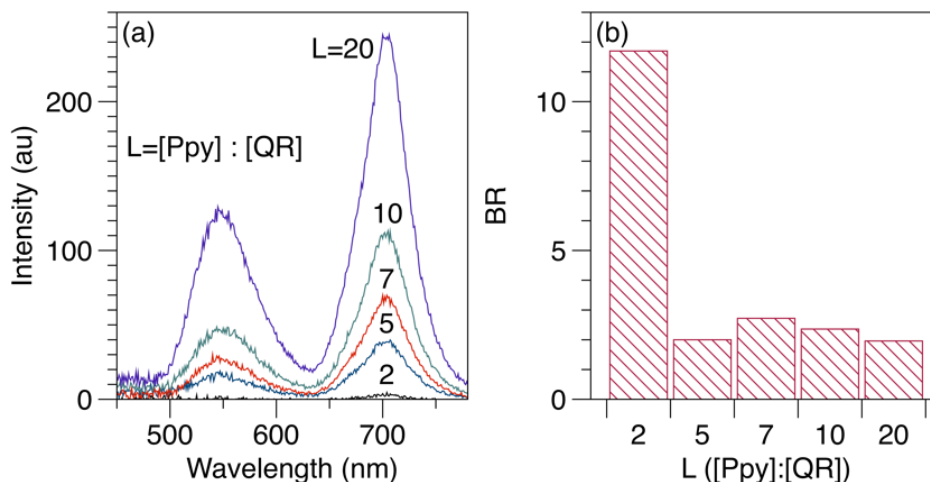


Figure 3.7: Effect of Ppy loading ($L = [\text{Ppy}]:[\text{QR}]$) on (a) the BRET signal and (b) BRET efficiency.

The effect of molar loading ratio ($L = [\text{Ppy}] : [\text{QR}]$) on the BRET efficiency for the new QR/GSH/Ppy conjugates was investigated as shown in Figure 3.7. The BR decreased with increasing Ppy loading but the BRET signal intensity increased. This is consistent with previous data for the QR/His/Ppy system, where an optimum L was attributed to the distance of the Ppy donor from the QR core acceptor.¹¹ The increase in BRET signal intensity and decrease in BRET efficiency with increasing Ppy loading is indicative of an increasing contribution of radiative energy transfer.

The stability of the BRET signal was measured for five days, as shown in Figure 3.8. The BR and signal intensity remained stable, around $\text{BR} = 26$, for the QR/GSH/Ppy conjugates for the duration of the experiment. The BRET signal showed a very small emission peak for the LH_2 compared to the QR emission, so it is hypothesized that the majority of the signal is from non-radiative energy transfer, however, it is possible that there is some radiative energy transfer occurring. The increased stability is hypothesized to be due to the zwitterionic nature of GSH, which has been found to lead to an increase in colloidal stability.⁴⁶

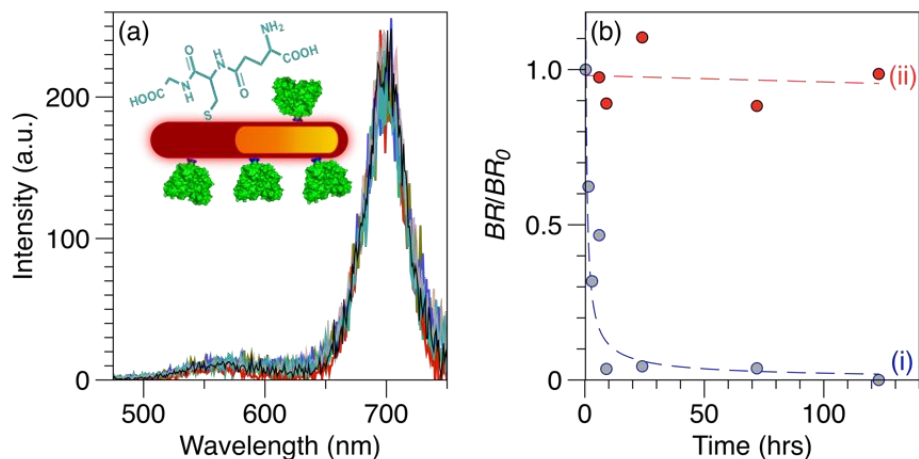


Figure 3.8: BRET stability of (a) QR/GSH/Ppy; (b) scatter plot of (i) QR/His/Ppy BRET stability and (ii) QR/GSH/PPy BRET stability over time.

Control experiments were performed to determine if the high QR emission intensity in the BRET signal was due to radiative or non-radiative energy transfer. First, a non-histagged protein was incubated with the QR solution. As shown in Figure 3.9, the ratio of the emission from the QR and from the LH₂ is much lower than in the QR/Ppy BRET experiments with the histagged protein. This is a good indication that radiative energy transfer is occurring in this sample, however, the bioluminescence of Ppy-LH₂ in the absence of QRs is much more intense than the Ppy-LH₂ peak in Figure 3.9, indicating non-radiative energy transfer. Since the protein is made up of amino acids, non-specific interactions can arise from the presence of surface reactive amine and thiol functional groups on the Ppy surface. The non-specific interactions can bring the Ppy close to the QR for non-radiative energy transfer to occur.

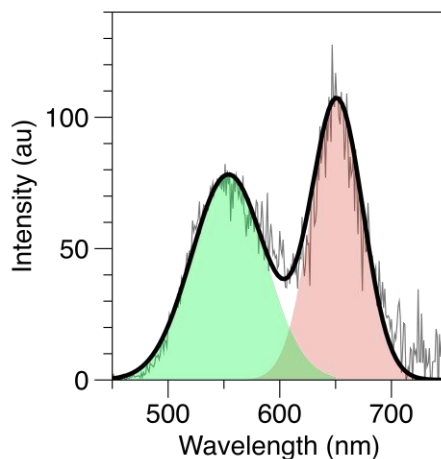


Figure 3.9: Bioluminescence of QR/His + non-histagged Ppy.

Figure 3.10 shows the molecular modeling results for the charge and hydrophobicity calculations of Ppy. The surface charge calculations for Figure 3.10a were performed using a protein contact potential calculation program in PyMOL. This is a qualitative, not quantitative, calculation because it calculates surface charge by averaging charges over a small region of space and ignores solvent screening effects. Assuming that only the thiol group of glutathione is bound to the QR, the QR/GSH conjugate should have a -2 charge in borate buffer so non-specific interactions would favor the positively charged locations on the protein. As shown in Figure 3.10a, there are a few positively charged regions that could interact. Figure 3.10b shows the hydrophobicity of the Ppy, which was measured by giving a false color to the amino acids based on their individual hydrophobicity. The Ppy surface appears to have a lot of hydrophobic regions, which would contribute to QR colloidal instability in buffers.

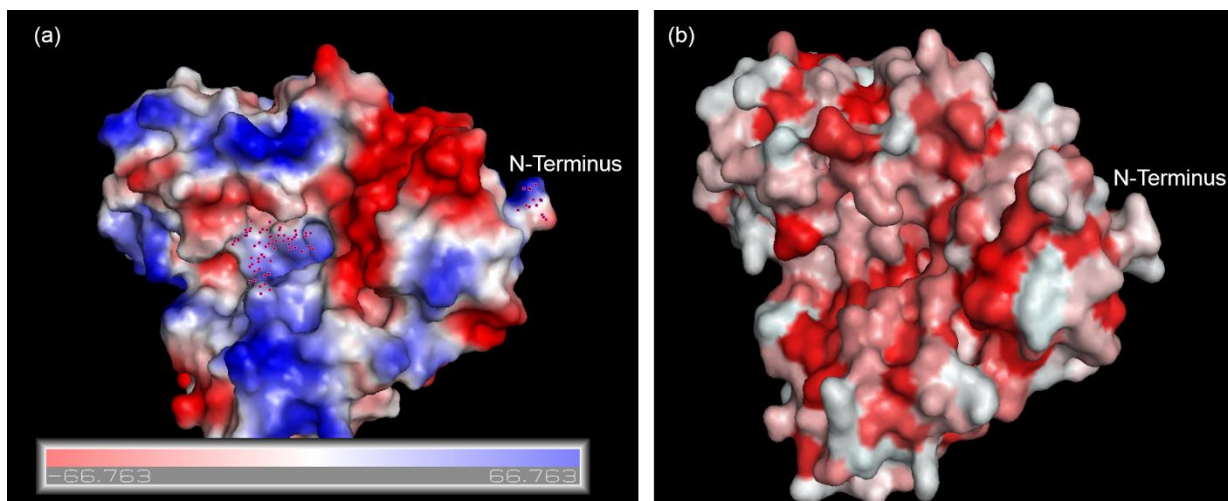


Figure 3.10: Qualitative molecular calculations for Ppy of (a) surface charge and (b) hydrophobicity (red regions are hydrophobic).

Two control experiments were performed to observe the signal intensity when the QR surface was inaccessible for the Ppy to adsorb. As shown in Figure 3.11, a bulky PEG-SH ligand was bound to the QR surface prior to protein conjugation to prevent Ppy binding. The Ppy emission in the QR/PEG-SH mixture has the same intensity in the bioluminescence of the protein alone, whereas in the QR/His/Ppy conjugates, the Ppy intensity is very low. Since non-radiative energy transfer is characterized by a decrease in donor emission, the retention of the Ppy intensity indicates that the QR emission is due to radiative energy transfer, where the Ppy acts as a light source for the QRs. The intensity of the QR is around 400 a.u, which is much higher than in previous BRET studies. Using these results, it is likely that the BRET from the stability experiments in Figures 3.3 and 3.8 is due to non-radiative energy transfer, since the Ppy emission is almost completely diminished. In those experiments, the QR intensity is due to the high QY of the sample (QY = 20%).

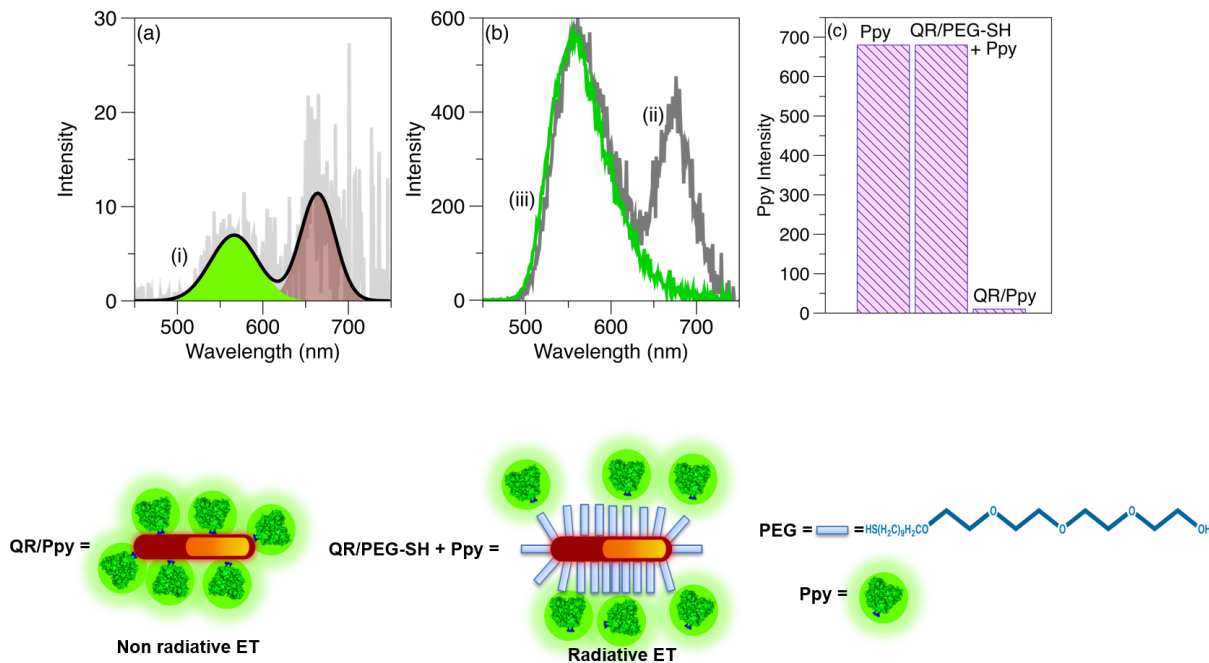


Figure 3.11: Probing the energy transfer of QR/Ppy conjugates (a) (i) BRET of QR/Ppy; (b) Bioluminescence of (ii) QR/PEG-SH+Ppy and (iii) Ppy alone; (c) Ppy intensity for the different conjugates to investigate the extent of energy transfer.

In Figure 3.12, imidazole was added to QR/Ppy conjugates after BRET was measured to observe the release of the surface bound Ppy. Protein attachment to the QR surface is driven by the polyhistag imidazole, so excess imidazole was chosen to displace the polyhistag. The decrease in the BR and the increase in the bioluminescence intensity indicates that the imidazole displaced Ppy molecules from the QR surface and the energy transfer has more non-radiative contributions to the signal. The LH₂ peak in the QR/GSH/Imidazole+Ppy is not as intense as LH₂-Ppy mixture alone, so it is likely that some of the signal contributions are still due to non-radiative energy transfer. This also indicates that it is difficult to displace the bound protein. When the same experiment was performed but with the imidazole added first to prevent Ppy from binding, the LH₂-Ppy intensity was higher than when imidazole was added after the Ppy conjugation, as shown in Figure 3.13. It still wasn't as intense as LH₂-Ppy bioluminescence alone and it wasn't as low as it was in the QR/Ppy conjugate, so there is both radiative and non-radiative energy transfer

occurring in Figure 3.13a. This data also indicates that it is hard to displace bound Ppy molecules from the QR surface.

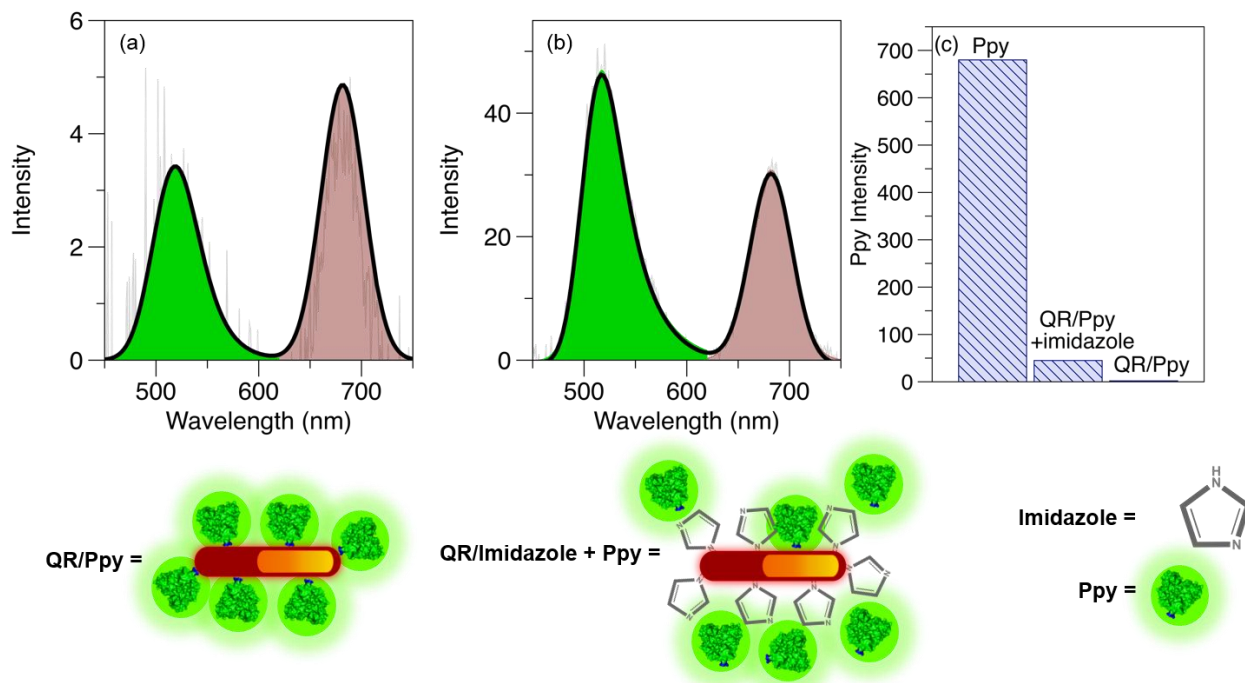


Figure 3.12: Bioluminescence of QR/GSH/Ppy (a) before and (b) after the addition of imidazole ([Imidazole] $^{-}$:[QR]=100,000); (c) change in LH₂+Ppy intensity for the different nanoconjugates.

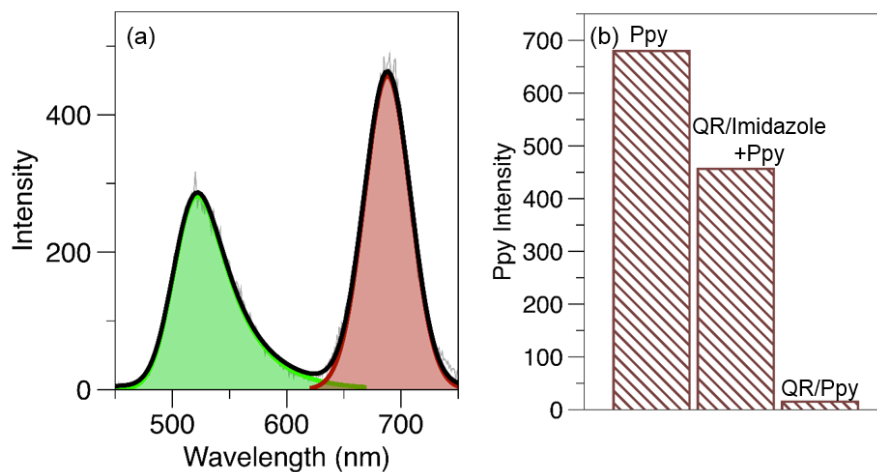
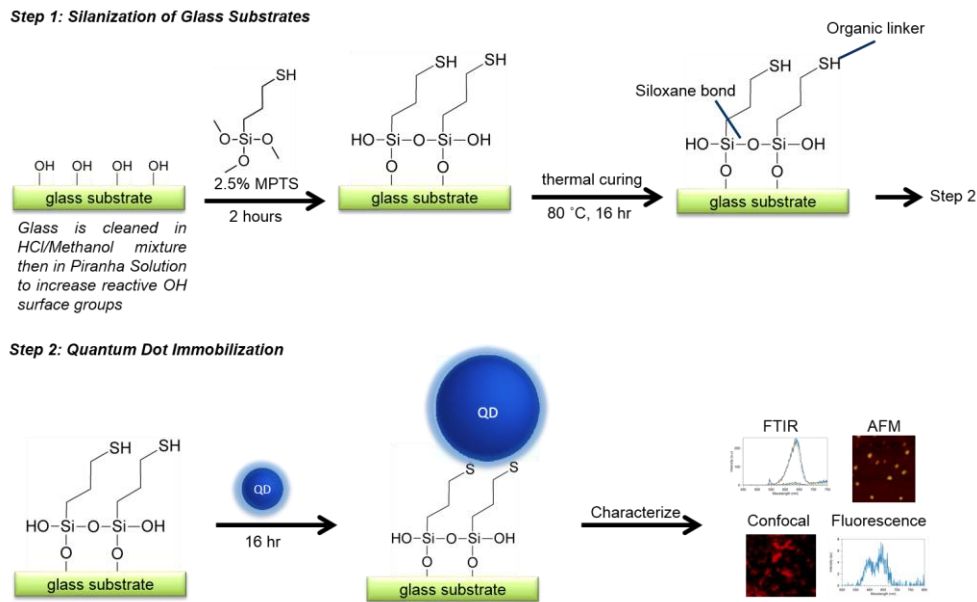


Figure 3.13: (a) Bioluminescence of QR/GSH/Imidazole+Ppy (b) Ppy intensity for the different nanoconjugates.

The only successful route to prevent non-radiative energy transfer was the addition of a large, bulky ligand that blocked the Ppy from the surface. In the next control study, a very high molar excess of imidazole was added to displace Ppy from the surface. Although this was successful, as indicated by the increase in signal intensity, the Ppy signal was still not completely recovered, indicating that non-radiative energy transfer occurred. When the imidazole was bound before the Ppy, the Ppy intensity was almost ten times higher. Since the non-radiative energy transfer was much higher when the Ppy was bound before the imidazole, the Ppy may preferentially bind to locations on the QR that lead to more efficient energy transfer. There are defect sites close to the core that can act as electron sinks,⁴⁷ so molecules that bind to this location will bind stronger.

3.3.2 Investigation of BRET of Immobilized QRs

It was previously hypothesized that the low optimum loading ratios is a result of preferential protein binding on the defects near the core or the inaccessibility of the substrate at higher Ppy loading.¹¹ To test the location of the protein binding as a function of BR, QR/Ppy conjugates were immobilized onto glass substrates. As shown in Scheme 3.2, silane was coupled to glass substrates via liquid phase deposition.³⁶⁻³⁸ The glass substrates were silanized with 3-mercaptopropyltrimethoxysilane (MPTS) to increase reactivity towards QDs by incorporating a thiol linker. Once QDs were successfully bound to the glass substrates, the substrates were analyzed using FTIR, AFM and confocal microscopy.



Scheme 3.2: Illustration demonstrating the silanization of glass substrate immobilized with QDs.

The silane is bound to the glass substrate and to adjacent silanes through a siloxane bond. Figure 3.14 shows the QD absorption and fluorescence that is seen on glass substrates after silanization, indicating successful attachment. QDs and QRs were attached either in toluene or they were phase transferred into aqueous conditions using a histidine mediated ligand exchange.

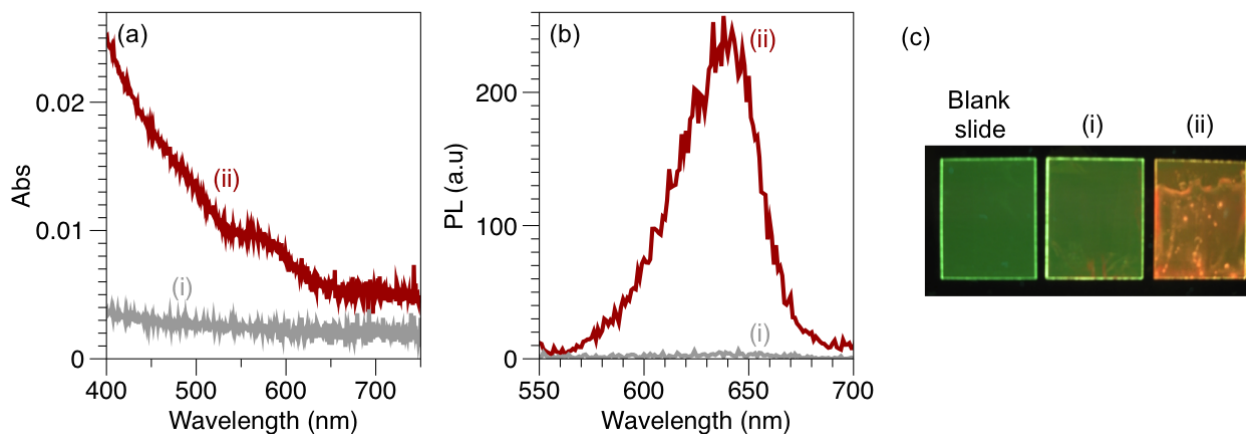


Figure 3.14: (a) UV-Vis and (b) PL spectra of (i) unsilanized glass after incubation with QDs for 7 hrs in toluene and (ii) silanized glass after incubation with QDs for 7 hrs in toluene; (c) UV illuminated image of an unsilanized blank slide, (i) unsilanized glass slide after QD incubation and (ii) silanized glass slide after QD incubation.

QD attachment with different conditions was investigated. The effect of time, solvent and QD concentration on the fluorescence of the glass was monitored. In Figure 3.15, QD/TOPO in toluene was incubated with glass slides for 7 and 74 hours. Between 7 and 74 hours, the concentration on the glass slide did not increase, indicating that QDs are immobilized after 7 hours. A slight red shift over time was observed and this could be due to interactions between adjacent QDs. The small QD PL on the unsilanized glass shows a slight nonspecific attraction for the glass, which may be due to electrostatic interactions between the QDs and free hydroxyl groups on the glass substrate.

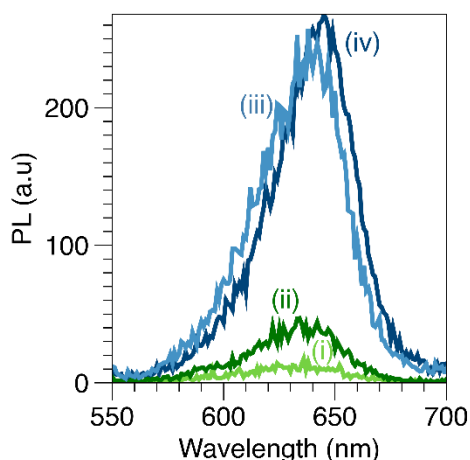


Figure 3.15: Fluorescence spectra showing the effect of different QD/TOPO incubation times with silanized and unsilanized glass (i) unsilanized glass incubated for 74 hours, (ii) unsilanized glass incubated for 7 hours, (iii) silanized glass incubated for 7 hours and (iv) silanized glass incubated for 74 hours.

For future energy transfer studies with Ppy, it is necessary to use QDs in buffers. Figure 3.16 shows the fluorescence of glass slides after incubating with QDs in toluene and in borate buffer. The glass slides have a higher fluorescence signal after incubation with QD/TOPO in toluene compared to QD/His in borate buffer. This can be due to two different effects: a larger concentration of QD/TOPO on the glass as well as the higher QY of QD/TOPO. After histidine-

mediated phase transfer, QD PL tends to drop. To determine more conclusively if there are more QDs on the glass, a calibration curve is needed.

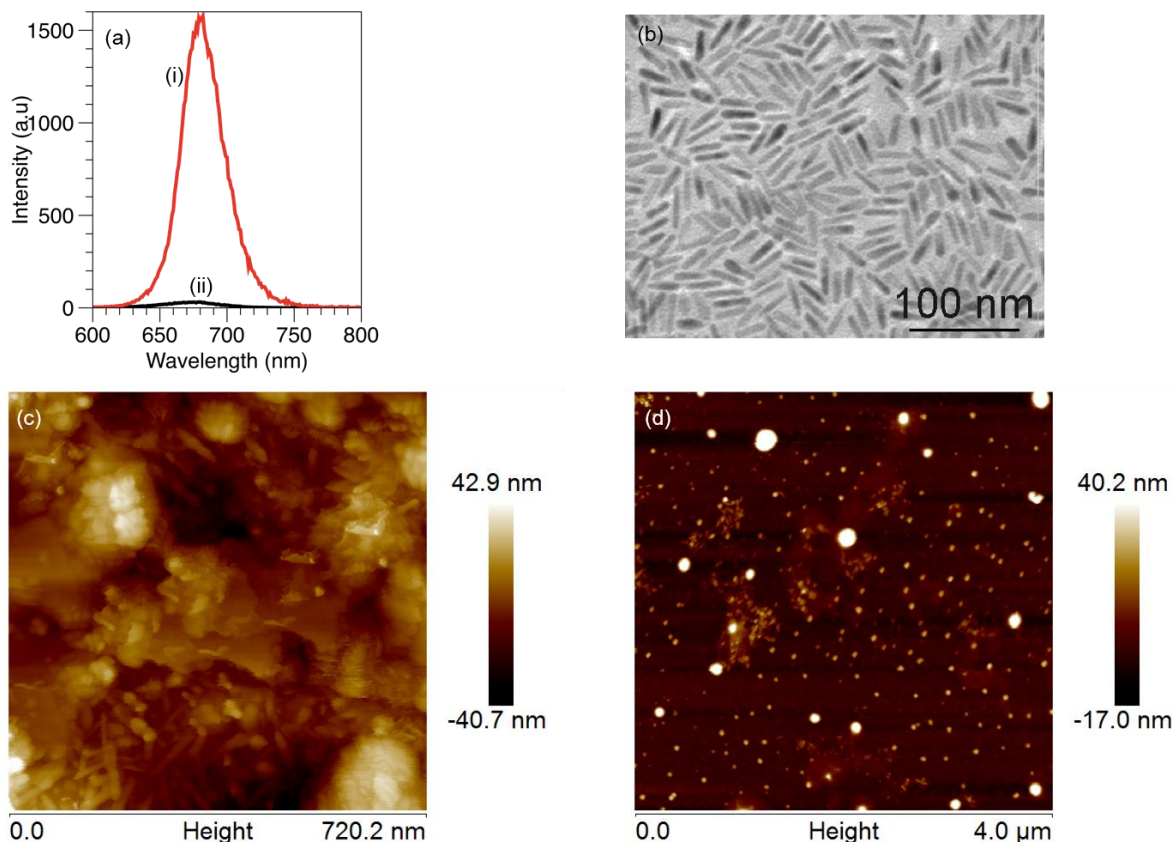


Figure 3.16: Effect of solvent on QR glass incubation: (a) (i) QR/TOPO in toluene and (ii) QR/His in borate buffer; (b) TEM of QR/TOPO (Aspect ratio = 3.72) (c) AFM of QR/TOPO and (d) AFM of QR/His.

To image the QR binding, AFM images were acquired for the hydrophilic and hydrophobic QRs, as shown in Figure 3.16. The AFM image of QR/TOPO appears to have multiple layers, so the QDs could be coupling to one another, causing aggregation. The AFM of the QR/His sample appears to be less densely populated and have less of a multilayer. This is useful for imaging the location of the protein on the QR for future studies.

Two different approaches were concurrently taken to quantify the QD/His coverage on glass. In one approach, the absorbance of the QD solution before and after glass incubation was

measured to determine the concentration of QDs that were immobilized on the glass. In the second approach, a calibration curve on silanized glass was created, where different QD/His concentrations were drop casted on to the glass and the fluorescence was measured to obtain a calibration curve. These two techniques were compared and the data is found in Figure 3.17 and table 3.3.

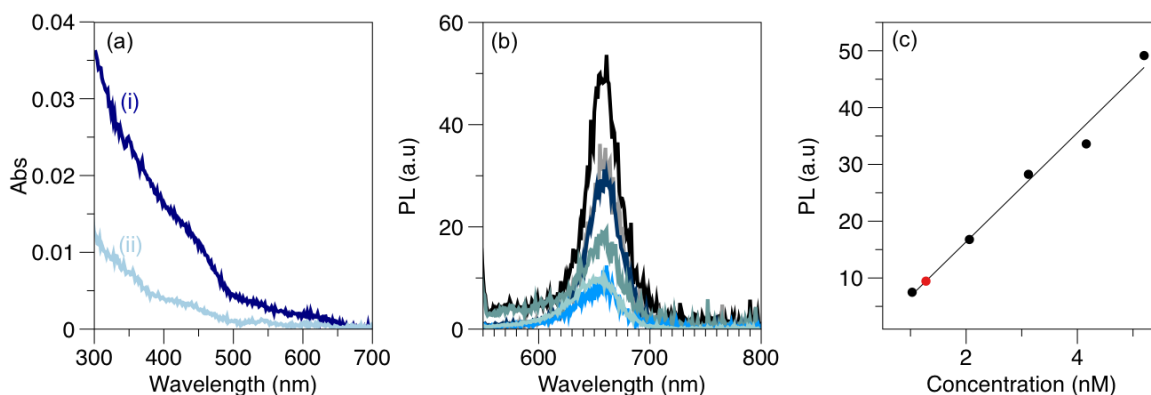


Figure 3.17: Quantification of QD(655) on glass: (a) UV-Vis of the QD glass supernatant (i) before and (ii) after glass incubation ($\epsilon_{\text{QD}} = 2.1 \times 10^6 \text{ M}^{-1}\text{cm}^{-1}$); (b) Fluorescence spectra for known QD concentrations drop casted on glass and (c) Beer's Law plot for the fluorescence spectra ($y = 9.59x - 2.82$; $R^2 = 0.98$)

As shown in table 3.3, the QD concentrations measured using the two techniques are comparable, with a 4-5% difference between them.

Table 3.3: Comparison of different techniques to quantify QDs immobilized to glass substrates

Technique	[QD] _{glass} (nM)	Surface Density (QD/cm ²)
UV – Vis	1.2	3.7×10^5
Fluorescence	1.3	3.9×10^5
% Difference	4.0 %	5.3 %

The QR immobilization was examined using FTIR. As shown in Figure 3.18, the intense peak for the siloxane bond before deposition, around 1080 cm^{-1} , becomes broader and shifts to a lower energy frequency after deposition (Si-O , $\nu = 950\text{ cm}^{-1}$).

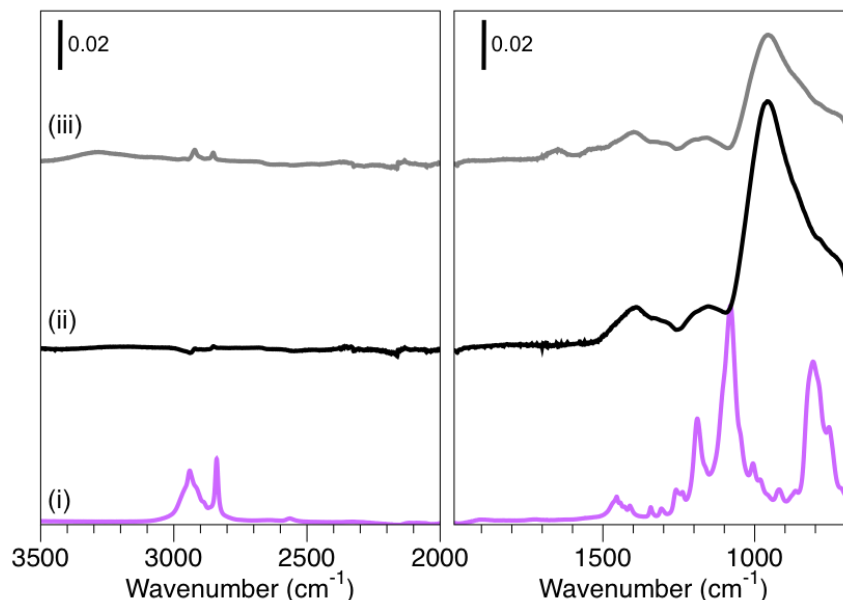


Figure 3.18: FTIR: (i) MPTS, (ii) Silanized glass, (iii) QD/His on glass. These samples were baseline corrected using a piece of glass freshly cleaned with piranha solution.

The characteristic FTIR vibrations for Figure 3.18 are listed in table 3.4.⁴⁸

Table 3.4: FTIR Vibrations

Vibration	ν
Alkane	2950 cm^{-1}
Alkane	2850 cm^{-1}
S-H stretch	2550 cm^{-1}
C – O stretch	$1450\text{-}1390\text{ cm}^{-1}$
Si-CH ₃	$1190\text{-}1150\text{ cm}^{-1}$
Si-O	$1080\text{-}950\text{ cm}^{-1}$

Confocal microscopy was used to obtain fluorescent images of the QD layer. Figure 3.19 shows a confocal image of QD655 immobilized on a glass substrate using a laser excitation with

an emission of 405 nm. The red fluorescence is attributed to QD655 and the image shows a high QD coverage on the surface. The coverage does not appear uniform and there are locations on the glass where there are clusters of QDs, which is consistent with the coverage seen on AFM.

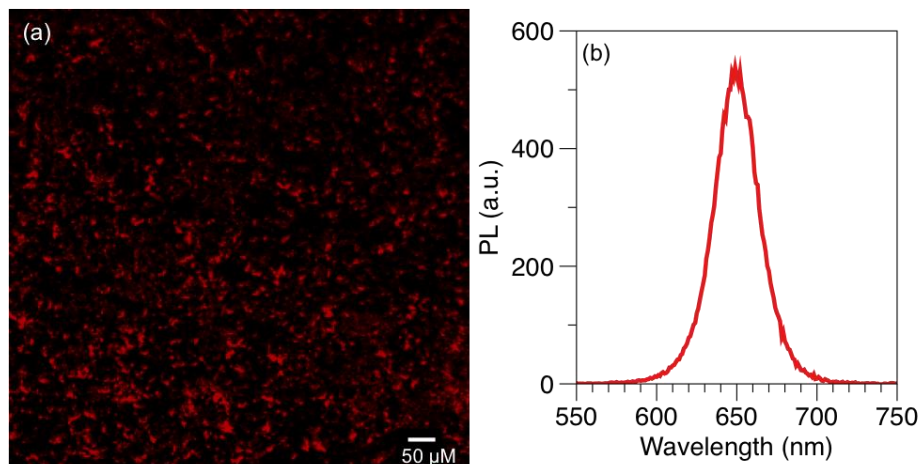


Figure 3.19: (a) False color confocal image for glass with QD655 (red) excited with a 405 nm laser and under 10x magnification; (b) PL of QD655 on glass.

Next, a glass substrate was incubated with two different color QDs and examined under confocal microscopy. A silanized glass substrate was incubated with QD515 and QD580 with a stoichiometric ratio ($r = [\text{QD515}]/[\text{QD580}]$) of 1. PL calibration experiments confirmed that $[\text{QD515}] = 4.6 \text{ nM}$ and $[\text{QD580}] = 3.2 \text{ nM}$. Control glass slides containing only QD515 and only QD580 were prepared and the confocal images were acquired. In Figure 3.20, confocal fluorescence was measured of QD515 immobilized on glass substrates. When the sample was excited at 405 nm, QD515 emission appeared. At an excitation of 488 nm, the emission for QD515 is still present but the fluorescence is not as strong because the absorption at 488 nm is less than the absorption at 405 nm. At 633 nm, the QD or emission from the QD, so the absence of signal at 633 nm indicates that the emission at the previous wavelengths were from QDs.

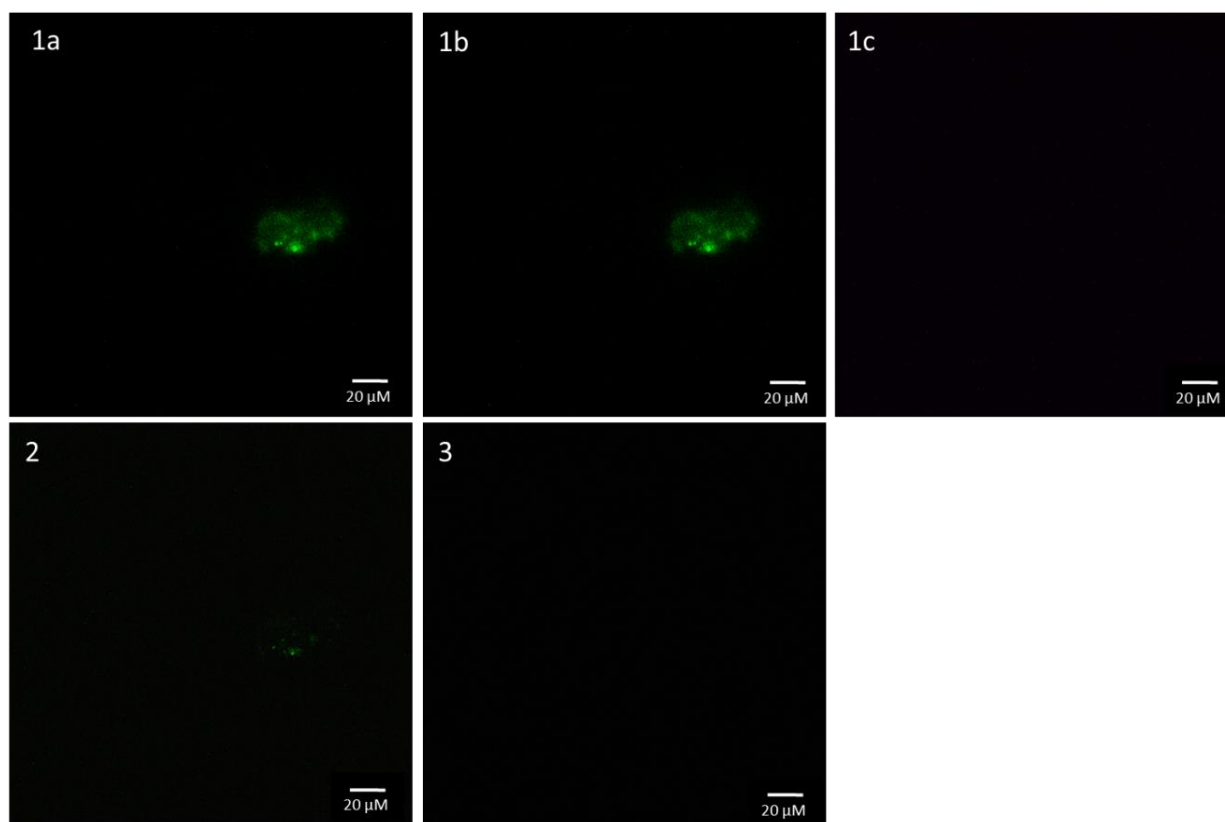


Figure 3.20: False color confocal images for glass with QD515 (green): (1a) Overlay of fluorescence images for the QD515 and the QD580 channel ($\lambda_{\text{ex}} = 405$ nm), (1b) Fluorescence of the QD515 channel ($\lambda_{\text{ex}} = 405$ nm), (1c) Fluorescence emission from the QD580 channel ($\lambda_{\text{ex}} = 405$ nm); (2) Overlay of both channels, excited at 488 nm; (3) Overlay of the emission from QD515 and QD580 ($\lambda_{\text{ex}} = 633$ nm).

Figure 3.21 shows the confocal images for QD580 immobilized on glass. As indicated with the images for QD515, the emission for QD580 was present and the emission for QD515 was absent. The sample was also imaged during an excitation of 543 nm and 633 nm. Since the fluorescence was still present at 543 nm and not 633 nm, the fluorescence emission observed was from QD580.

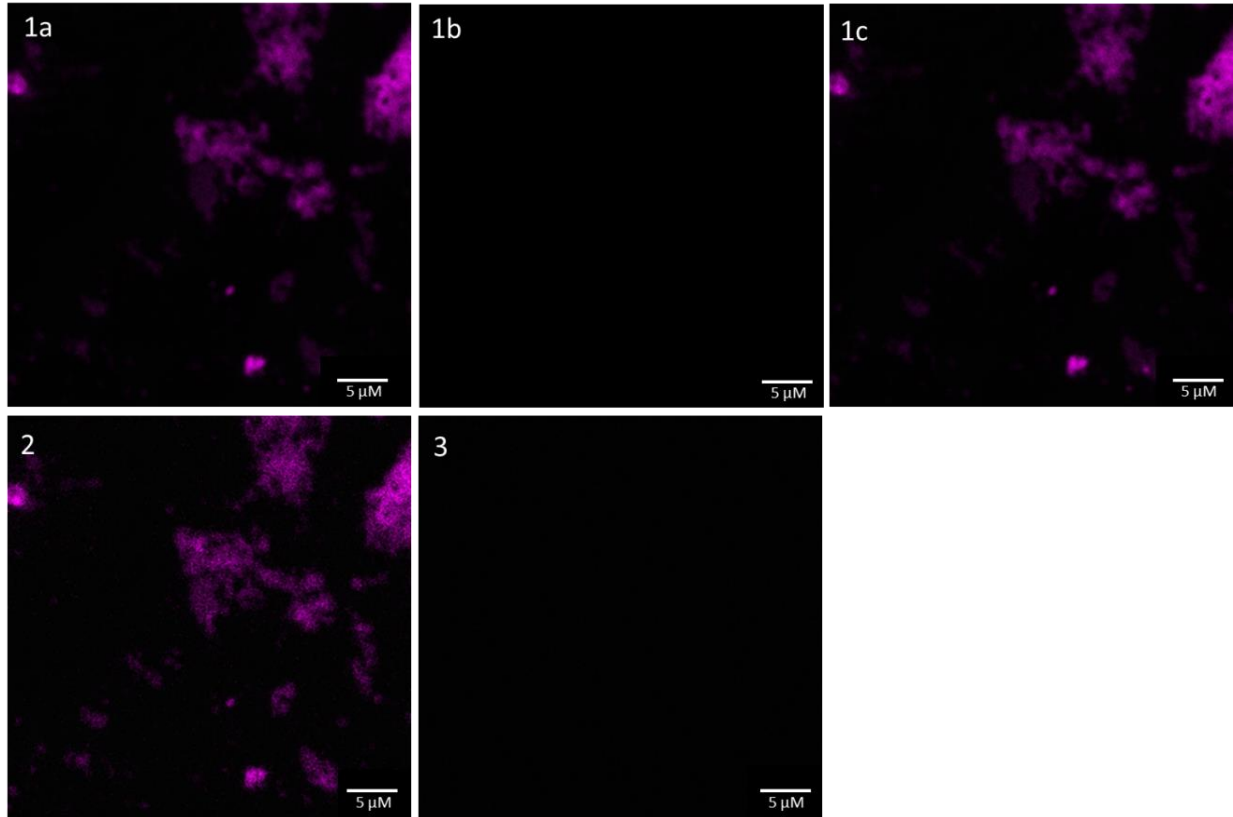


Figure 3.21: False color confocal images for glass with QD580 (purple): (1a) Overlay of the fluorescence channels for QD515 and QD580 excited at 405 nm, (1b) Fluorescence channel for QD 515, excited at 405 nm, (1c) Fluorescence intensity for QD580 only excited at 405 nm; (2) Overlay of both channels, excited at 543 nm; (3) Fluorescence emission overlaid for both QDs, excited at 633 nm.

Fluorescence images were obtained for the glass that was incubated with QD515 and QD580. In Figure 3.22, emission from both QD515 and QD580 is present when the sample was excited at 405 nm. At an excitation wavelength of 543 nm, the emission from QD515 disappears, but the emission for QD580 is still present. At an emission wavelength of 633 nm, no emission is present. The confocal data shows that both QDs were immobilized onto the glass.

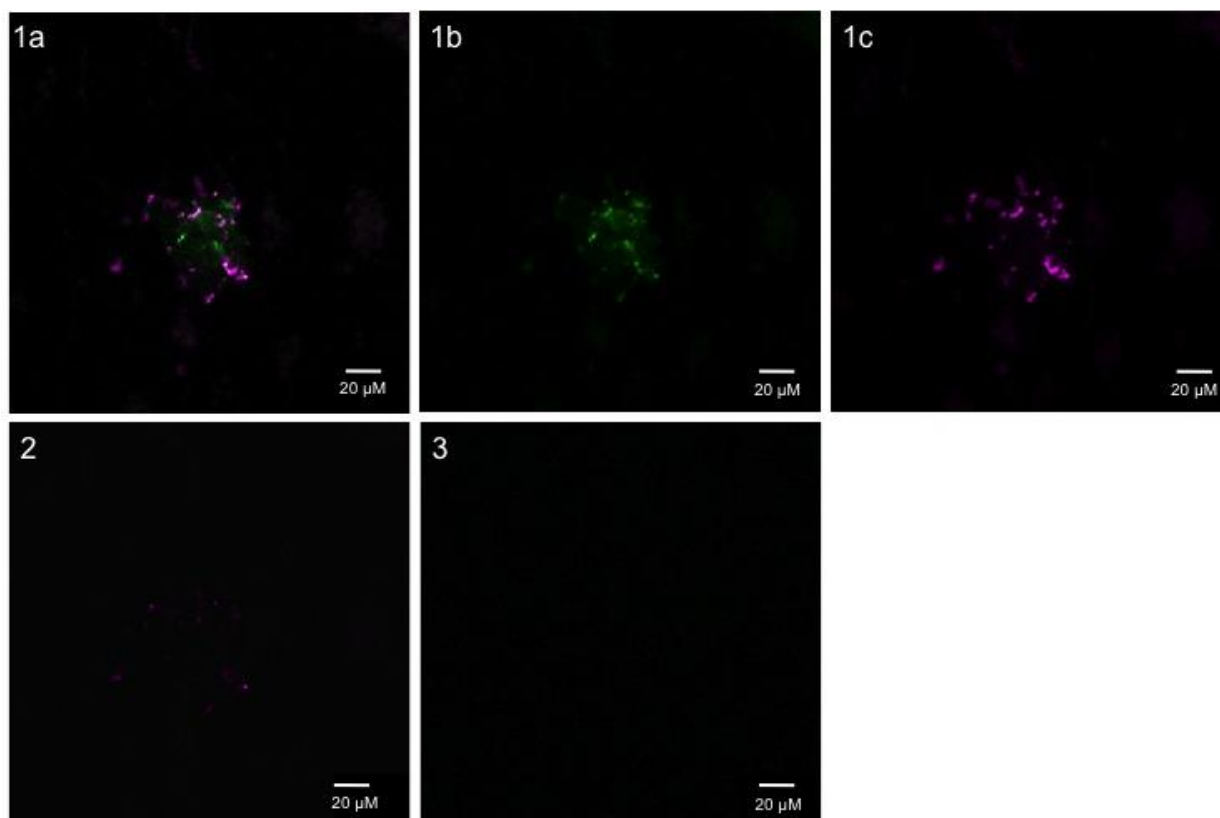


Figure 3.22: False color confocal images for glass with QD515 (green) + QD580 (purple): (1a) Excited at 405 nm overlaid both channels, (1b) Excited at 405 nm channel for QD515 only, (1c) Excited at 405 nm channel for QD580 only; (2) Excited at 543 overlaid both channels; (3) Excited at 633 overlaid both channels.

QD/Ppy was immobilized on glass to image BRET using bioluminescence imaging and on the confocal. In Figure 3.23, the PL and BL was collected for QD/PPy immobilized on glass.

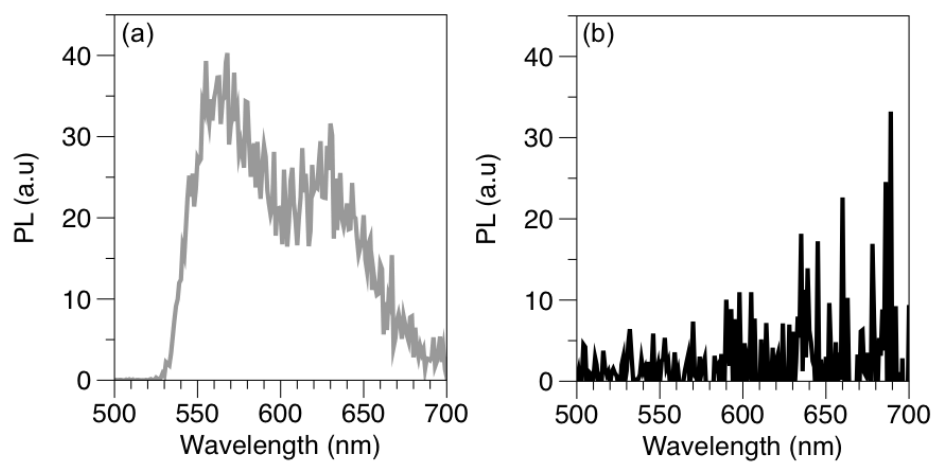


Figure 3.23: QR/Ppy+LH₂ on glass (a) PL, (b) BL.

The PL shows the presence of the QD and LH₂. Unfortunately, the BL was unable to be captured using BL spectroscopy or confocal imaging, as shown in Figure 3.24; however, the BRET on glass was visible by eye.

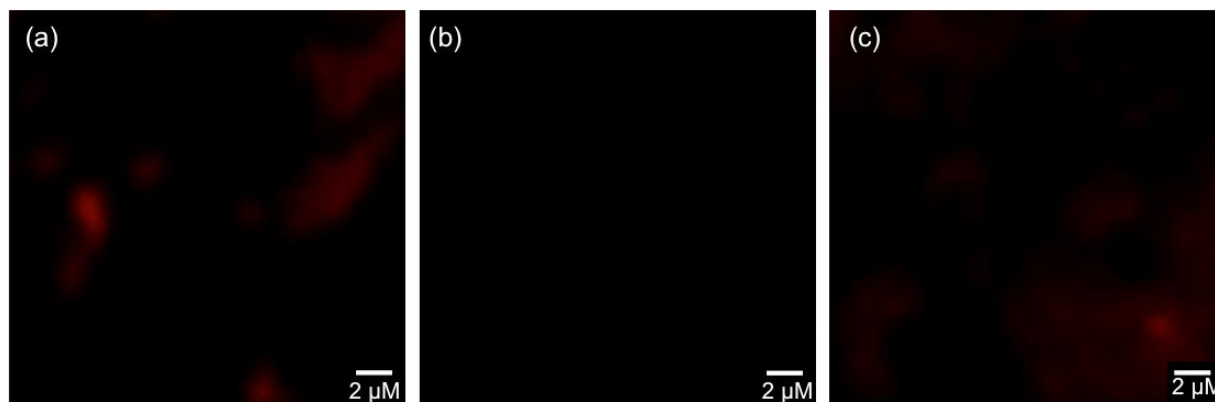


Figure 3.24: Confocal imaging of BRET on glass substrates (a) QD(655)/PPy on glass before the addition of LH₂ excited at 633 nm; (b) QD(655)/PPy + LH₂ in the absence of an excitation source; (c) QD(655)/PPy + LH₂ excited at 633 nm.

The concentration of QDs on glass is in the nanomolar regime, so the BRET emission may be too low to be imaged using the current equipment. These images were acquired on a confocal that is equipped with a photomultiplier tube (PMT), but it may not be sensitive enough to image the low signal intensity that is associated with BRET. In vivo imaging of BRET has been accomplished using a more sensitive cooled charge coupled diode detector (CCD).⁴⁹

3.4 Conclusions

In summary, a bioluminescent protein was coupled to QRs to create energy donor-acceptor pairs that do not require an external excitation source. This system can be incorporated into the QD/DNA self-assembly system in Chapter 2 to prevent coexcitation of the donor and acceptor in the FRET pair. This is important because it can make energy transfer calculations easier and it can increase the sensitivity of biosensors created from these conjugates since the QD emission is a

result of energy transfer alone. To make the transition into the QD FRET system more viable, the QD/Ppy conjugates should have long-term stability and no radiative energy transfer. The long term stability of the QR/Ppy conjugates was improved by changing the ligand during the phase transfer from his to GSH. This colloidal stability is believed to occur due to the zwitterionic nature of GSH. FTIR measurements indicate that the GSH binds to the QR surface through the thiol group. This work also showed that beyond the optimum loading ratio ($L > 2$), the decrease in BR the increase in signal intensity is due to radiative energy transfer, however, even with a nonhistagged Ppy or a large excess of imidazole, there was evidence of non-radiative energy transfer. To obtain a purely radiative system, the QRs were functionalized with a bulky ligand that made the surface inaccessible to the Ppy. The higher BR at lower loading ratios may be due to the protein binding close to the core first.

To probe the effect of the protein binding location on the BR, QRs were immobilized onto glass substrates using a liquid phase deposition technique for single particle studies. The glass substrates were imaged using photoluminescence, AFM, FTIR and confocal microscopy. The data shows successful QD immobilization in various solvents and conditions but with non-uniform multilayers. Confocal microscopy shows the presence of QDs on the glass and the ability to simultaneously attach QDs with different emission. The biggest limitation for future studies in this chapter was the inability to use confocal or BL to measure the BRET of the immobilized QRs. More sensitive instrumentation is needed to be able to measure the effect of protein binding on BR.

3.5 References

- (1) Wilson, T.; Hastings, J. W. Bioluminescence. *Annu. Rev. Cell Dev. Biol.* **1998**, *14*, 197–230.
- (2) Widder, E. A.; Falls, B. Review of Bioluminescence for Engineers and Scientists in Biophotonics. *IEEE J. Sel. Top. Quantum Electron.* **2014**, *20* (2), 232–241.
- (3) Conti, E.; Franks, N. P.; Brick, P. Crystal Structure of Firefly Luciferase Throws Light on a Superfamily of Adenylate-Forming Enzymes. *Structure* **1996**, *4* (3), 287–298.
- (4) Marques, S. M.; Esteves da Silva, J. C. G. Firefly Bioluminescence: A Mechanistic Approach of Luciferase Catalyzed Reactions. *IUBMB Life* **2009**, *61* (1), 6–17.
- (5) Navizet, I.; Liu, Y.-J.; Ferré, N.; Roca-Sanjuán, D.; Lindh, R. The Chemistry of Bioluminescence: An Analysis of Chemical Functionalities. *Chemphyschem Eur. J. Chem. Phys. Phys. Chem.* **2011**, *12* (17), 3064–3076.
- (6) Yue, L.; Liu, Y.-J.; Fang, W.-H. Mechanistic Insight into the Chemiluminescent Decomposition of Firefly Dioxetanone. *J. Am. Chem. Soc.* **2012**, *134* (28), 11632–11639.
- (7) Vieira, J.; Pinto da Silva, L.; Esteves da Silva, J. C. G. Advances in the Knowledge of Light Emission by Firefly Luciferin and Oxyluciferin. *J. Photochem. Photobiol. B* **2012**, *117*, 33–39.
- (8) White, E. H.; Steinmetz, M. G.; Miano, J. D.; Wildes, P. D.; Morland, R. Chemi- and Bioluminescence of Firefly Luciferin. *J. Am. Chem. Soc.* **1980**, *102* (9), 3199–3208.
- (9) Lakowicz, J. *Principles of Fluorescence Spectroscopy*, Second.; Kluwer Academic/Plenum Publishers: New York, NY, 1999.
- (10) So, M.-K.; Xu, C.; Loening, A. M.; Gambhir, S. S.; Rao, J. Self-Illuminating Quantum Dot Conjugates for in Vivo Imaging. *Nat. Biotechnol.* **2006**, *24* (3), 339–343.
- (11) Alam, R.; Fontaine, D. M.; Branchini, B. R.; Maye, M. M. Designing Quantum Rods for Optimized Energy Transfer with Firefly Luciferase Enzymes. *Nano Lett.* **2012**, *12* (6), 3251–3256.
- (12) Alam, R.; Zylstra, J.; Fontaine, D. M.; Branchini, B. R.; Maye, M. M. Novel Multistep BRET-FRET Energy Transfer Using Nanoconjugates of Firefly Proteins, Quantum Dots, and Red Fluorescent Proteins. *Nanoscale* **2013**, *5* (12), 5303–5306.
- (13) Alam, R.; Karam, L. M.; Doane, T. L.; Zylstra, J.; Fontaine, D. M.; Branchini, B. R.; Maye, M. M. Near Infrared Bioluminescence Resonance Energy Transfer from Firefly Luciferase-Quantum Dot Bionanoconjugates. *Nanotechnology* **2014**, *25* (49), 495606.
- (14) So, M.-K.; Loening, A. M.; Gambhir, S. S.; Rao, J. Creating Self-Illuminating Quantum Dot Conjugates. *Nat. Protoc.* **2006**, *1* (3), 1160–1164.
- (15) Lee, J. O.; Lim, B.; Kim, Y.-P. Bioluminescence Resonance Energy Transfer Nanoprobes for Imaging. *IEEE J. Sel. Top. Quantum Electron.* **2014**, *20* (3), 57–66.
- (16) Takai, A.; Nakano, M.; Saito, K.; Haruno, R.; Watanabe, T. M.; Ohyanagi, T.; Jin, T.; Okada, Y.; Nagai, T. Expanded Palette of Nano-Lanterns for Real-Time Multicolor Luminescence Imaging. *Proc. Natl. Acad. Sci.* **2015**, *112* (14), 4352–4356.
- (17) Du, J.; Yu, C.; Pan, D.; Li, J.; Chen, W.; Yan, M.; Segura, T.; Lu, Y. Quantum-Dot-Decorated Robust Transductable Bioluminescent Nanocapsules. *J. Am. Chem. Soc.* **2010**, *132* (37), 12780–12781.
- (18) Hsu, C.-Y.; Chen, C.-W.; Yu, H.-P.; Lin, Y.-F.; Lai, P.-S. Bioluminescence Resonance Energy Transfer Using Luciferase-Immobilized Quantum Dots for Self-Illuminated Photodynamic Therapy. *Biomaterials* **2013**, *34* (4), 1204–1212.

- (19) Yao, H.; Zhang, Y.; Xiao, F.; Xia, Z.; Rao, J. Quantum Dot/bioluminescence Resonance Energy Transfer Based Highly Sensitive Detection of Proteases. *Angew. Chem. Int. Ed Engl.* **2007**, *46* (23), 4346–4349.
- (20) Lan, T.-H.; Liu, Q.; Li, C.; Wu, G.; Steyaert, J.; Lambert, N. A. BRET Evidence That $\beta 2$ Adrenergic Receptors Do Not Oligomerize in Cells. *Sci. Rep.* **2015**, *5*.
- (21) Hoffman, J. B.; Choi, H.; Kamat, P. V. Size-Dependent Energy Transfer Pathways in CdSe Quantum Dot–Squaraine Light-Harvesting Assemblies: Förster versus Dexter. *J. Phys. Chem. C* **2014**, *118* (32), 18453–18461.
- (22) Berezin, M. Y.; Achilefu, S. Fluorescence Lifetime Measurements and Biological Imaging. *Chem. Rev.* **2010**, *110* (5), 2641–2684.
- (23) Dragavon, J.; Blazquez, S.; Rekiki, A.; Samson, C.; Theodorou, I.; Rogers, K. L.; Tournebize, R.; Shorte, S. L. In Vivo Excitation of Nanoparticles Using Luminescent Bacteria. *Proc. Natl. Acad. Sci.* **2012**, *109* (23), 8890–8895.
- (24) Halivni, S.; Sitt, A.; Hadar, I.; Banin, U. Effect of Nanoparticle Dimensionality on Fluorescence Resonance Energy Transfer in Nanoparticle–Dye Conjugated Systems. *ACS Nano* **2012**, *6* (3), 2758–2765.
- (25) Krahne, R.; Morello, G.; Figuerola, A.; George, C.; Deka, S.; Manna, L. Physical Properties of Elongated Inorganic Nanoparticles. *Phys. Rep.* **2011**, *501* (3-5), 75–221.
- (26) Medintz, I. L.; Uyeda, H. T.; Goldman, E. R.; Mattoussi, H. Quantum Dot Bioconjugates for Imaging, Labelling and Sensing. *Nat. Mater.* **2005**, *4* (6), 435–446.
- (27) Stobiecka, M. Novel Plasmonic Field-Enhanced Nanoassay for Trace Detection of Proteins. *Biosens. Bioelectron.* **2014**, *55*, 379–385.
- (28) Branchini, B. R.; Ablamsky, D. M.; Murtiashaw, M. H.; Uzasci, L.; Fraga, H.; Southworth, T. L. Thermostable Red and Green Light-Producing Firefly Luciferase Mutants for Bioluminescent Reporter Applications. *Anal. Biochem.* **2007**, *361* (2), 253–262.
- (29) Ando, Y.; Niwa, K.; Yamada, N.; Enomoto, T.; Irie, T.; Kubota, H.; Ohmiya, Y.; Akiyama, H. Firefly Bioluminescence Quantum Yield and Colour Change by pH-Sensitive Green Emission. *Nat. Photonics* **2008**, *2* (1), 44–47.
- (30) Branchini, B. R.; Ablamsky, D. M.; Rosenberg, J. C. Chemically Modified Firefly Luciferase Is an Efficient Source of Near-Infrared Light. *Bioconjug. Chem.* **2010**, *21* (11), 2023–2030.
- (31) Branchini, B. R.; Ablamsky, D. M.; Rosenman, J. M.; Uzasci, L.; Southworth, T. L.; Zimmer, M. Synergistic Mutations Produce Blue-Shifted Bioluminescence in Firefly Luciferase†. *Biochemistry (Mosc.)* **2007**, *46* (48), 13847–13855.
- (32) Woodroffe, C. C.; Meisenheimer, P. L.; Klaubert, D. H.; Kovic, Y.; Rosenberg, J. C.; Behney, C. E.; Southworth, T. L.; Branchini, B. R. Novel Heterocyclic Analogues of Firefly Luciferin. *Biochemistry (Mosc.)* **2012**, *51* (49), 9807–9813.
- (33) Mattoussi, H.; Mauro, J. M.; Goldman, E. R.; Anderson, G. P.; Sundar, V. C.; Mikulec, F. V.; Bawendi, M. G. Self-Assembly of CdSe–ZnS Quantum Dot Bioconjugates Using an Engineered Recombinant Protein. *J. Am. Chem. Soc.* **2000**, *122* (49), 12142–12150.
- (34) Martín-García, B.; Paulo, P. M. R.; Costa, S. M. B.; Velázquez, M. M. Photoluminescence Dynamics of CdSe QD/Polymer Langmuir–Blodgett Thin Films: Morphology Effects. *J. Phys. Chem. C* **2013**, *117* (28), 14787–14795.
- (35) Šimurda, M.; Němec, P.; Trojáněk, F.; Malý, P. Substantial Enhancement of Photoluminescence in CdSe Nanocrystals by Femtosecond Pulse Illumination. *Thin Solid Films* **2004**, *453–454*, 300–303.

- (36) Pallavicini, P.; Dacarro, G.; Galli, M.; Patrini, M. Spectroscopic Evaluation of Surface Functionalization Efficiency in the Preparation of Mercaptopropyltrimethoxysilane Self-Assembled Monolayers on Glass. *J. Colloid Interface Sci.* **2009**, *332* (2), 432–438.
- (37) Vistas, C. R.; Águas, A. C. P.; Ferreira, G. N. M. Silanization of Glass chips—A Factorial Approach for Optimization. *Appl. Surf. Sci.* **2013**, *286*, 314–318.
- (38) Halliwell, C. M.; Cass, A. E. G. A Factorial Analysis of Silanization Conditions for the Immobilization of Oligonucleotides on Glass Surfaces. *Anal. Chem.* **2001**, *73* (11), 2476–2483.
- (39) Zylstra, J.; Amey, J.; Miska, N. J.; Pang, L.; Hine, C. R.; Langer, J.; Doyle, R. P.; Maye, M. M. A Modular Phase Transfer and Ligand Exchange Protocol for Quantum Dots. *Langmuir* **2011**, *27* (8), 4371–4379.
- (40) Han, H.; Zylstra, J.; Maye, M. M. Direct Attachment of Oligonucleotides to Quantum Dot Interfaces. *Chem. Mater.* **2011**, *23* (22), 4975–4981.
- (41) Sitt, A.; Salant, A.; Menagen, G.; Banin, U. Highly Emissive Nano Rod-in-Rod Heterostructures with Strong Linear Polarization. *Nano Lett.* **2011**, *11* (5), 2054–2060.
- (42) Hadar, I.; Hitin, G. B.; Sitt, A.; Faust, A.; Banin, U. Polarization Properties of Semiconductor Nanorod Heterostructures: From Single Particles to the Ensemble. *J. Phys. Chem. Lett.* **2013**, *4* (3), 502–507.
- (43) Diroll, B. T.; Dadosh, T.; Koschitzky, A.; Goldman, Y. E.; Murray, C. B. Interpreting the Energy-Dependent Anisotropy of Colloidal Nanorods Using Ensemble and Single-Particle Spectroscopy. *J. Phys. Chem. C* **2013**, *117* (45), 23928–23937.
- (44) Shaviv, E.; Salant, A.; Banin, U. Size Dependence of Molar Absorption Coefficients of CdSe Semiconductor Quantum Rods. *ChemPhysChem* **2009**, *10* (7), 1028–1031.
- (45) Law, G. H. E.; Gandelman, O. A.; Tisi, L. C.; Lowe, C. R.; Murray, J. A. H. Mutagenesis of Solvent-Exposed Amino Acids in Photinus Pyralis Luciferase Improves Thermostability and pH-Tolerance. *Biochem. J.* **2006**, *397* (2), 305.
- (46) Park, J.; Nam, J.; Won, N.; Jin, H.; Jung, S.; Jung, S.; Cho, S.-H.; Kim, S. Compact and Stable Quantum Dots with Positive, Negative, or Zwitterionic Surface: Specific Cell Interactions and Non-Specific Adsorptions by the Surface Charges. *Adv. Funct. Mater.* **2011**, *21* (9), 1558–1566.
- (47) Mokari, T.; Sztrum, C. G.; Salant, A.; Rabani, E.; Banin, U. Formation of Asymmetric One-Sided Metal-Tipped Semiconductor Nanocrystal Dots and Rods. *Nat. Mater.* **2005**, *4* (11), 855–863.
- (48) Finocchio, E.; Macis, E.; Raiteri, R.; Busca, G. Adsorption of Trimethoxysilane and of 3-Mercaptopropyltrimethoxysilane on Silica and on Silicon Wafers from Vapor Phase: An IR Study. *Langmuir* **2007**, *23* (5), 2505–2509.
- (49) De, A.; Gambhir, S. S. Noninvasive Imaging of Protein–protein Interactions from Live Cells and Living Subjects Using Bioluminescence Resonance Energy Transfer. *FASEB J.* **2005**, *19* (14), 2017–2019.

Chapter 4

Investigating the Drug Binding in Encoded Nanocarriers for the Delivery of Idarubicin

In this chapter, I investigated the binding of an anticancer drug, idarubicin, to DNA capped AuNP nanocarriers through DNA duplex melting temperature and kinetic studies. The use of a thermoresponsive polymer for controlled drug retention and release was also explored for this system.

4.1 Introduction

Oligonucleotide functionalized AuNPs (DNA-AuNP) have been incorporated into many different applications to improve current technologies in targeted drug delivery,¹⁻⁷ biosensing,⁸ in vivo imaging,⁹ gene regulation¹⁰ and self-assembly.¹¹⁻¹⁵ In one example, Mirkin and coworkers used antisense DNA functionalized AuNPs to prevent mRNA from translating into proteins to control protein expression in cells.^{1,10} In these studies, the DNA-AuNP system was more efficient, more non-toxic and had a higher cellular delivery than commercial systems.¹⁰ This study demonstrates that AuNPs are excellent drug delivery candidates.⁹ AuNP surfaces are also very versatile and can easily be functionalized with other molecules to increase the targeting ability or control the drug release.^{4,7,16} Xia *et. al.* created drug loaded photosensitive gold nanocages to control the drug release with nIR light.¹⁶ In this system, the wavelength of nIR light matched the Au absorption, causing the Au to absorb the light and release heat energy that cause the thermoresponsive polymer chains to collapse to release the drug.¹⁶⁻¹⁸ For drug delivery, studies have also shown that AuNP drug delivery vehicles enhance the cytotoxicity and apoptosis of drug resistant cancer cells.¹⁹

Thermoresponsive “smart” polymers based on poly(N-isopropylacrylamide) (PNIPAAm) have interesting stimuli-responsive properties that make them an ideal addition to drug delivery systems.¹⁶⁻¹⁸ These polymers have a sharp, reversible, phase transition at the low critical solution temperature (T_c). When $T \leq T_c$, the polymer is hydrophilic and the chains are extended; when $T \geq T_c$, the polymer is hydrophobic and the chains agglomerate. The turbid state that is created after this transition can be measured through the amount of light that is transmitted before and after T_c . Compared to other polymers, PNIPAAm polymers have lower T_c , which is ideal for biological applications where the physiological temperature is 37 °C.

Our group recently invented encoded nanocarriers for the delivery of doxorubicin (Dox) and Actinomycin D (ActD).²⁻⁴ In my project, I designed the system to accommodate IDA, which is important because IDA interacts more efficiently with DNA and is more potent than the other anthracyclines.^{20,21} In this chapter, AuNPs were functionalized with DNA duplexes that had a high affinity for the intercalation of idarubicin (IDA). IDA is an anthracycline antineoplastic agent that is used for the treatment of a variety of cancers.²² Anthracyclines induce many intracellular effects including intercalation into nuclear DNA with a high affinity for 5'-TCA sequence, free oxygen radical liberation and direct membrane toxicity.^{21,22} The final event that leads to cell death is the inhibition of topoisomerase II, an enzyme that cleaves DNA and controls DNA supercoiling.²¹⁻²³ The amount of anthracyclines that bind to cellular DNA correlates directly to cell death, indicating the importance of DNA intercalation for the drug toxicity.²¹ As shown in Figure 4.1, the flat, planar aglycan portion of IDA intercalates in the major groove of the DNA and alters the structure by slightly unwinding the double helix, while the daunosamine sugar bends to interact with the minor groove.^{4,24} The increase in π stacking and van der Waals interactions upon IDA intercalation correspond to an increased duplex stability. Although research suggests that the prerequisite for

cell death is accumulation of IDA in the nucleus, cell studies have shown that only a small portion of drug delivered accumulates in the cell or even in the nucleus.²¹ AuNP drug delivery vehicles can be utilized to increase IDA drug targeting. Since anthracyclines have a cardiotoxic effect, increasing the drug efficacy and targeting is beneficial to limit the amount of drug needed for effective treatment.

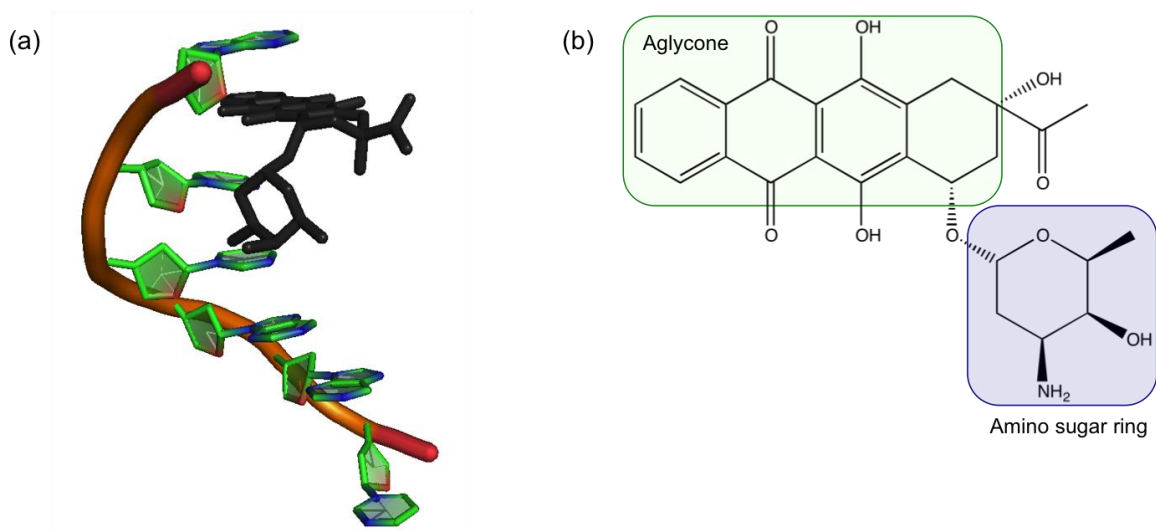


Figure 4.1: a) PyMOL representation of the drug molecule complex upon IDA intercalation in the DNA helix; b) chemical structure and functional groups of IDA.

In this chapter, the surface of AuNPs were functionalized with dsDNA (**ab**) that had a high affinity for IDA. In addition, a thermoresponsive polymer, poly(N-isopropylacrylamide-co-propylacrylamide) (**p**) with $T_c=51$ °C was incorporated into this system to control the drug release of IDA. When $T \geq T_c$, the polymer compresses, exposing the DNA and the intercalated IDA on the AuNPs. At lower temperatures, ($T \leq T_c$), the polymer is extended in an attempt to protect the intercalated IDA from desorbing from the AuNP vehicle.

4.2 Experimental

4.2.1 Chemicals.

Gold (III) chloride Hydrate (HAuCl_4 , 99.999%), Trisodium Citrate ($\text{Na}_3\text{C}_6\text{H}_5\text{O}_7$, %), DL-dithiothreitol (DTT, 99.5%), sodium phosphate monobasic monohydrate ($\text{NaH}_2\text{PO}_4 \cdot \text{H}_2\text{O}$, 98.0-102.0%), sodium phosphate dibasic hepta-hydrate ($\text{Na}_2\text{HPO}_4 \cdot 7\text{H}_2\text{O}$, 98.0-102.0%), tris(2-carboxyethyl)phosphine) (TCEP, 98%) were purchased from Sigma Aldrich. Sodium chloride (NaCl , 100%) was purchased from Fischer Scientific and sephadex G25 DNA grade columns and agarose were purchased from GE Healthcare. Idarubicin HCl (IDA) was a gift from Transo-Pharm GmbH, Siek, Germany. Poly(N-isopropylacrylamide-co-propylacrylamide) (**p**) was synthesized in house by Kristen Hamner. All oligonucleotides were purchased from Integrated DNA technologies Inc. Dialysis membranes (15 kDa) were purchased from Biotech RC.

4.2.2 Synthesis and Functionalization of Gold Nanoparticles.

AuNP Synthesis. Citrate capped gold nanoparticles (13.8 ± 1.2 nm) were prepared using a standard citrate reduction of HAuCl_4 .¹¹ A solution of 1 mM HAuCl_4 in water was heated to 100 °C for about 30 minutes while stirring before a 38 mM solution of cold sodium citrate was added. After the solution turned red, it was taken off of the heat and stirred overnight. The concentration was determined using UV-visible spectroscopy (UV-Vis) using an extinction coefficient of $2.0 \times 10^8 \text{ cm}^{-1}\text{M}^{-1}$ at $\lambda = 525$ nm. Size was determined using dynamic light scattering (DLS) and transmission electron microscopy (TEM).

AuNP with ssDNA monolayer. A 5' thiol functionalized 35-mer oligonucleotide (**a** = 5'-HS-T₁₅ GTT TCA GTT TCA GTT TCA GT-3'), was reduced using dithiothreitol and purified through a DNA grade sephadex g25 column from GE. The concentration was determined using UV-Vis at $\lambda = 260$ nm with an extinction coefficient of $307,700 \text{ cm}^{-1} \text{M}^{-1}$. The reduced and purified

DNA was introduced onto the AuNP surface through a slow salt aging process.²⁵ Briefly, the AuNP were incubated with 300 molar excess of the oligonucleotide for 9 hours at room temperature. The salt concentration of this solution was slowly increased to 200 mM over five days. The solution was then purified through centrifugation at least 3 times before the final product was resuspended in phosphate buffer saline (PBS).

AuNP with mixed polymer and ssDNA monolayer. The salt aging process was modified to graft the pNIPAAm-co-pAAm polymer onto the AuNP surface. A disulfide initiator was used during the polymer (**p**) synthesis to create a disulfide bond in the middle of the polymer chain. Reducing the disulfide with TCEP separated the chains and introduced a thiolate group to bind to the AuNP surface. AuNPs (0.01-0.1 nmoles) were incubated with 300 molar excess of **a** and 12.5 molar excess of **p** for 9 hours at room temperature. The salt concentration of this solution was increased in daily 50 mM increments to a final [NaCl] = 200 mM. The solution was purified through centrifugation (2 hours, 9000 rpm). The supernatant was replaced with fresh PBS at least 3 times. The final **p-a**/AuNP conjugates were resuspended in 10 mM PBS ([NaCl] = 100 mM).

DNA-hybridization and drug loading. The complementary DNA strand, (**b** = 5'-ACT GAA ACT GAA ACT GAA ACA A-3'), was added to the **a**/AuNP in 100 molar excess relative to the AuNP and incubated overnight at room temperature. To hybridize **a** in the **p-a**/AuNP system, the solution was heated to 51 C and incubated with **b** for 1 hour then slowly cooled for an additional hour. The solutions were purified through centrifugation and resuspended in PBS. To determine the number of duplexes on the surface of AuNP, complementary oligonucleotides were modified with a fluorophore, (**b/cy3** = 5'-cy3-TAC TGA AAC TGA AAC TGA AAC AA-3'), from IDT DNA. The **a**/AuNP were hybridized with **b/cy3** in the same manner as with the unmodified oligonucleotides (**b**). The solution was centrifuged for 2 hours at 14000 rpm and the supernatant

was removed and measured using fluorescence. A calibration curve was created to determine the concentration of DNA that was not hybridized to the surface of the AuNP.²⁶ To load the drug, different ratios ($r = [\text{drug}] / [\text{DNA}]$) of drug to DNA were incubated with **ab**/AuNP at room temperature for 40 minutes. The interaction of the drug with the DNA was examined through melting temperature by evaluating the change in absorbance at $\lambda = 260$ nm while changing the temperature 1 °C / min from 25 - 80 °C.

Gel Electrophoresis. Gels containing 1% agarose were prepared by mixing 0.500 g of agarose with 50 mL 1x TBE buffer, heating in the microwave for about 65 s then cooling slightly before pouring in the mold. The gel was allowed to set for 40 minutes before sample loading. All samples were mixed with 10 μL glycerol prior to loading. Electrophoresis was carried out at 75 V for 40-50 minutes at room temperature. Gels were photographed using a digital camera under ambient light.

4.2.3 Dialysis Monitoring of Drug Release. Each kinetics experiment was carried out using dialysis, where a 15 kDa dialysis membrane was loaded with 200 μL of IDA/**ab**/AuNP ($r = 3$) or IDA/**p-ab**/AuNP ($r = 3$), sealed and submerged in 2 mL PBS. The membrane was stirred in the buffer at 37 °C for the duration of the experiment. The fluorescence intensity of aliquots from the solution outside of the membrane was measured every 5-10 minutes until the intensity remained constant, indicating that equilibrium had been reached. All IDA intensities were converted into concentrations using a fluorescence calibration curve.

4.2.4 Instrumentation

UV Visible Spectroscopy (UV-Vis). See section 2.2.5

Photoluminescence Spectroscopy (PL). See section 2.2.5

Dynamic Light Scattering (DLS). Malverne Zetasizer Nano ZS equipped with 633 nm

laser source and backscattering detector at 173 for hydrodynamic diameter (d_h) measurements, which are averaged from 6-10 measurements. All samples were filtered using a 0.22 m syringe filter.

Transmission Electron Microscopy (TEM). TEM spectra were collected on a JEOL 2000EX at 120 kV with a tungsten filament by Rabeka Alam at SUNY-ESF, N.C Brown Center for Ultrastructure Studies.

Fourier Transform Infrared Spectroscopy (FTIR). See section 2.2.5

Gel Electrophoresis. See section 2.2.5

4.2.5 Calculations

Kinetics. The free drug concentration at equilibrium was determined by fitting the kinetics data (%IDA released vs time) to an exponential as shown in Equation 4.1 using Microsoft Excel solver.²⁻⁴

$$y = \alpha(1 - e^{-\beta t}) \quad (4.1)$$

Where y is the percent drug released at time t, α is the percent drug released after equilibrium and β is the first order dissociation rate constant.³ The free drug concentration at equilibrium [IDA] was determined using Equation 4.2.

$$[IDA] = \frac{\alpha}{100} * [IDA]_{Total} \quad (4.2)$$

Where $[IDA]_{total}$ is the total drug concentration in the system. The chemical equation describing the association and dissociation of the IDA-DNA complex is shown in Equation 4.3.



where site is the dsDNA binding site and complex is the intercalation of IDA into the binding site and k_a and k_d are the association and dissociation rate constants, respectively. Equation 4.4 shows the rate equations at equilibrium, where the rate of the association and dissociation are equal.

$$k_a[IDA][site] = k_d[Complex] \quad (4.4)$$

Equation 1.4 can be rearranged to express equilibrium constant, K_{eq} , in terms of the products and the reactants or the rate constants, as shown in Equation 4.5.

$$K_{eq} = \frac{k_a}{k_d} = \frac{[Complex]}{[IDA][site]} \quad (4.5)$$

AuNP Concentration. The concentration of AuNPs was determined by using the extinction coefficient (ϵ) of $2 \times 10^8 \text{ M}^{-1}$ and Beer's Law, as shown in Equation 4.6.

$$A = \epsilon bc \quad (4.6)$$

Where A is the absorbance at 400 nm, b is the path length (1 cm) and c is the AuNP concentration.

4.3 Results and Discussion

In this project, the use of DNA functionalized AuNPs as a drug delivery vehicle to transport the intercalating chemotherapeutic agent idarubicin (IDA) was investigated. This system is unique because the AuNP vehicle can support a high drug concentration and is very flexible; it can be functionalized with molecules that target receptors that are overexpressed in cancer cells, such as folic acid or G protein-coupled receptors, to deliver the drug straight to the cancer tumor.²⁷ A thermoresponsive polymer was also incorporated to attempt to increase drug retention in the delivery vehicle for more controlled drug release.¹⁶⁻¹⁸

TEM measurements showed the citrate capped AuNPs (cit/AuNP) had a diameter of 13.8 ± 1.2 nm, as shown in Figure 4.2.

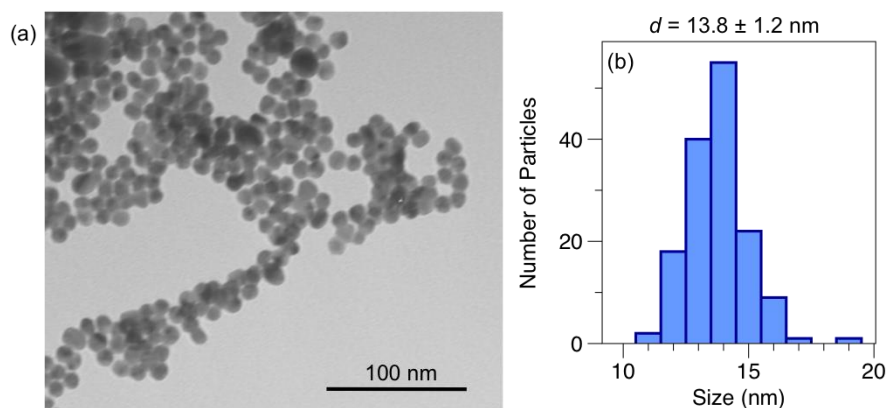
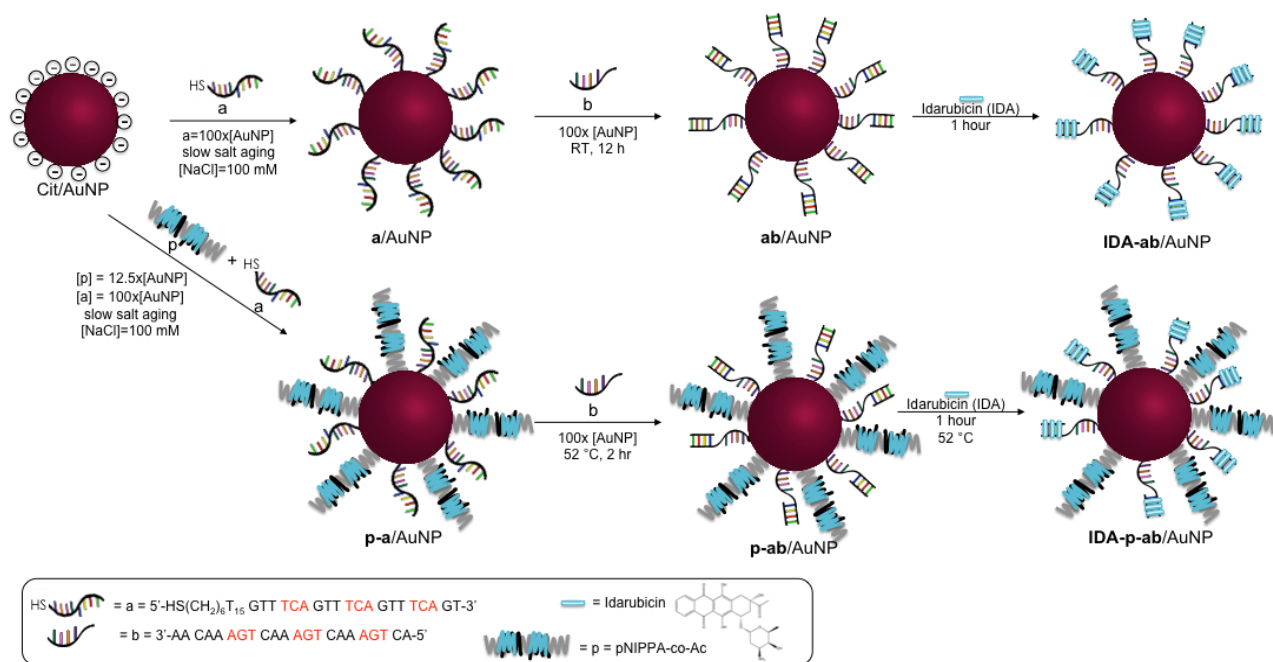


Figure 4.2: (a) TEM and (b) size distribution histogram (c) number weighted DLS spectra for cit/AuNP.

To create encoded nanocarriers, AuNPs were functionalized with DNA and a thermoresponsive polymer, as shown in Scheme 4.1. Cit/AuNPs were functionalized with SH-ssDNA (a) through a slow salt aging process followed by hybridization with a complementary strand (b).²⁵ The ab/AuNP conjugates were incubated with IDA to produce IDA/ab/AuNP through intercalation into the DNA duplex. To incorporate a thermoresponsive polymer pNIPAAm-co-

pAAM (**p**), the polymer was added during the salt aging process and hybridization and IDA loading was achieved at 52 °C, which is higher than the polymer's T_c .



Scheme 4.1: The polymer and dsDNA functionalization of AuNPs. IDA binding sites are highlighted in red.

The number of DNA complexes (**ab**) on the AuNPs were quantified by hybridizing the ssDNA on the particle to a fluorescent complementary strand (**b-cy3**) and hybridized to the DNA strand on the particle.²⁶ The hybridized AuNP conjugates were centrifuged and the supernatant photoluminescence was measured to determine the concentration of unbound **b-cy3**. A dsDNA loading of 44 ± 2 DNA duplexes (**ab**) per AuNP was measured for the **ab**-AuNP system, which corresponds to about 132 high-affinity IDA sites per AuNP, and the **p-ab**/AuNP system had an average dsDNA loading of 41 ± 5 DNA/AuNP, which corresponds to about 123 high-affinity IDA sites per AuNP.

The AuNP systems were characterized via DLS, UV-Vis, DNA duplex melting temperature (T_m) and kinetic studies. Figure 4.3 compares the UV-Vis surface plasmon shift upon

binding dsDNA to the AuNP. The peak at $\lambda = 260$ nm correlates with the DNA, so as the DNA is introduced and hybridized, the peak becomes more defined. The slight red shift of the surface plasmon indicates a change in the particle's interface upon displacing the weakly bound citrate molecules with the stronger binding thiolated DNA.

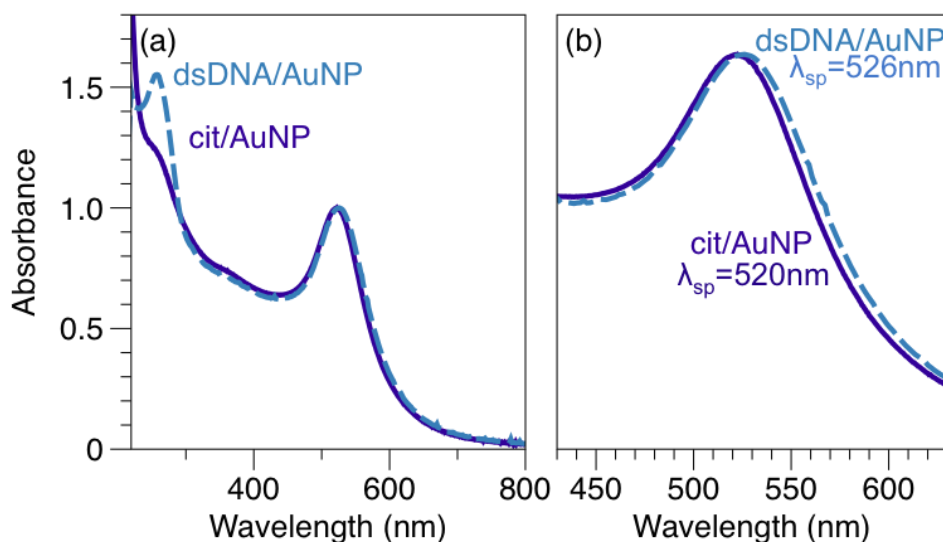


Figure 4.3: (a) Full UV-Vis Spectra for dsDNA/AuNP and cit/AuNP; (b) UV-Vis zoomed into the surface plasmon peak.

Dynamic light scattering (DLS) shows an increase in the particle's hydrodynamic diameter (d_h) upon ssDNA modification and hybridization as shown in table 4.1. The increase in d_h after ssDNA, dsDNA and polymer indicate successful functionalization. The highly negatively charged DNA strands cause the d_h to almost double compared to the cit-AuNPs.

Table 4.1: Change in AuNP d_h for the various functionalization steps

Sample	d_h (nm)
Cit-AuNP	17.6 ± 0.2
a /AuNP	32.1 ± 0.6
ab /AuNP	42.2 ± 0.8
p-a /AuNP	85.8 ± 7.5

The electrophoretic gel movement of the **a**/AuNP and **p-a**/AuNP were compared, as shown in Figure 4.4. After polymer modification, the d_h increased by over 50 nm at room temperature, indicating the polymer is extended past the ssDNA strands. As expected, the **p-a**/AuNP conjugate moved slower due to the larger d_h and the shielding of the highly negatively charged DNA backbone by the polymer.

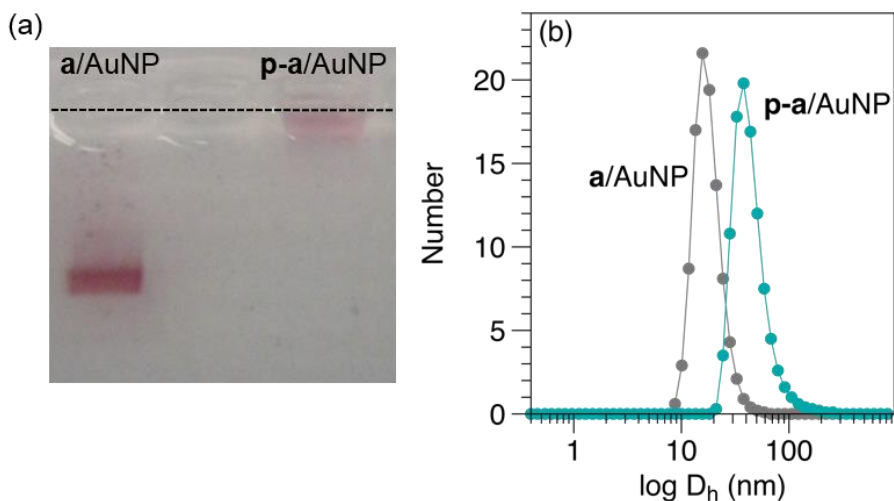


Figure 4.4: (a) gel electrophoresis and (b) DLS spectra of the **a**/AuNP and **p-a**/AuNP conjugates

The thermal denaturation of the DNA duplex for the **p-ab**/AuNP conjugates couldn't be measured as shown in Figure 4.5. The thermal profile resembled that of the **p-a**/AuNP conjugates and the polymer alone, where the absorption transition is at the polymer's T_c . The T_m for the **ab**/AuNP conjugate before drug loading was 66 °C, which is higher than the reported T_m of 56.4 °C for **ab** in the absence of the AuNP due to the cooperative melting effects on the AuNP surface.²⁸

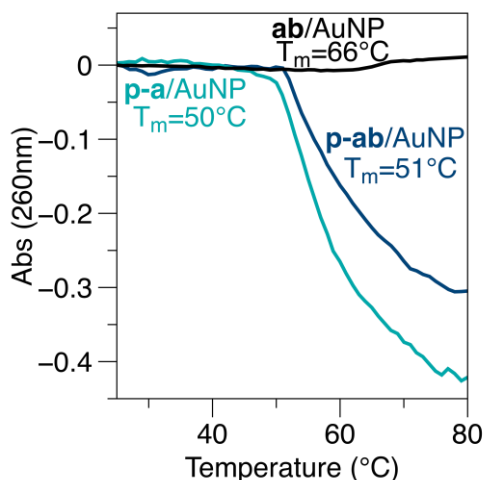


Figure 4.5: Change in absorbance as a function of T_m for **a/AuNP**, **ab/AuNP**, and **p-ab/AuNP**.

The effect of drug loading ($r = [\text{IDA}] / [\text{AuNP}]$) on the T_m of the DNA duplex was evaluated, as shown in Figure 4.6. As drug loading increased, the melting temperature increased, indicating successful IDA intercalation at the double helix. The increase in T_m is due to reduced electrostatic interactions, stronger van der Waals interactions and increased π stacking between DNA strands due to the intercalation of the aglycone portion of the drug. A higher, secondary melting temperature (T_m') appears after drug loading compared to the **ab/AuNP** system without IDA. This secondary T_m also appeared in the DOX system that was previously developed in our lab, but it occurred at temperatures below T_m , around 25-30 °C.^{2,3} Since this secondary T_m' only occurs after drug binding, it suggests that there are stronger binding interactions between the DNA, IDA and the AuNP.

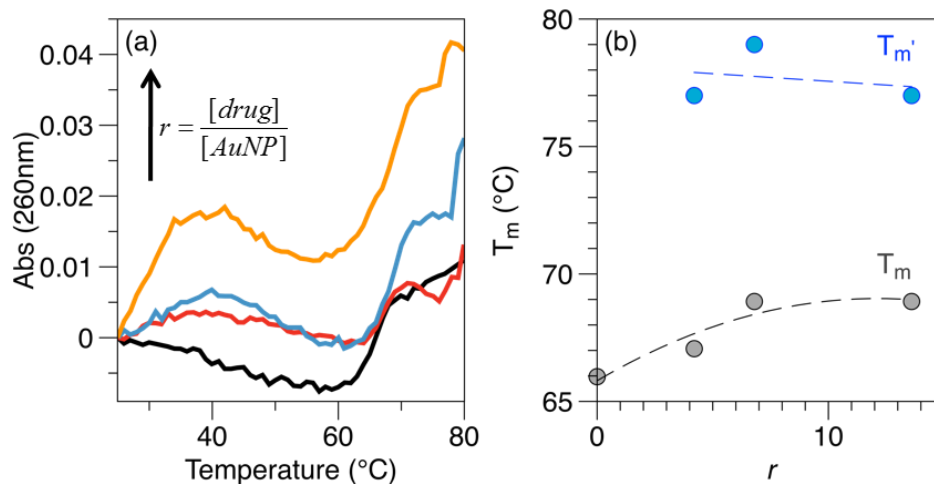
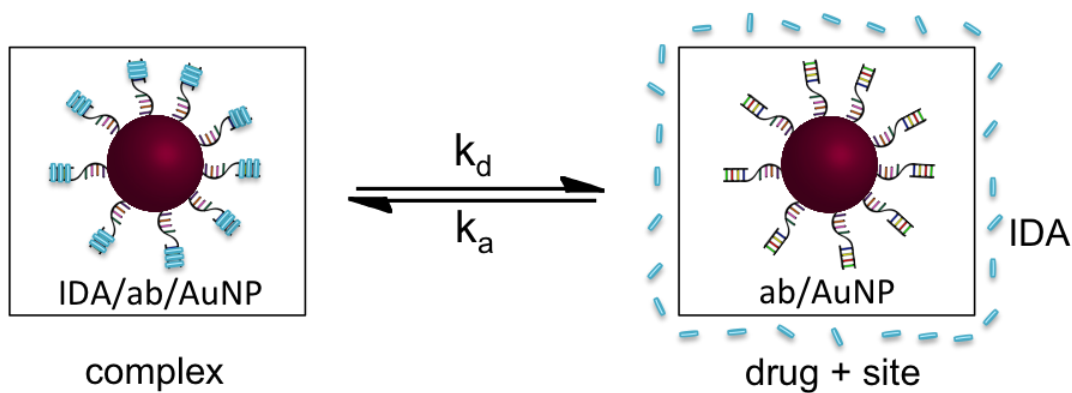


Figure 4.6: (a) Thermal denaturation of IDA/ab/AuNP loaded with different ratios of drug. (b) Ratio of drug as a function of melting temperature ($y = 66.2 + 0.3x$; $R^2 = 0.92$). ($[ab/AuNP] = 7$ nM)

The kinetics of drug release at equilibrium was measured for the two different nanocarriers. To do this, the nanocarrier was loaded into a dialysis membrane and the appearance of the fluorescent IDA outside of the membrane was measured and compared to a calibration curve to determine the drug binding at equilibrium. Scheme 4.2 gives an overview of this process.



Scheme 4.2: Schematic describing the drug equilibrium for the association and disassociation of IDA from the AuNP nanocarrier.

Figure 4.7 shows the results of the dialysis experiments for the two nanocarriers at physiological temperature ($T = 37\text{ }^{\circ}\text{C}$). The data was fit to an exponential to calculate the equilibrium constants.²⁻⁵

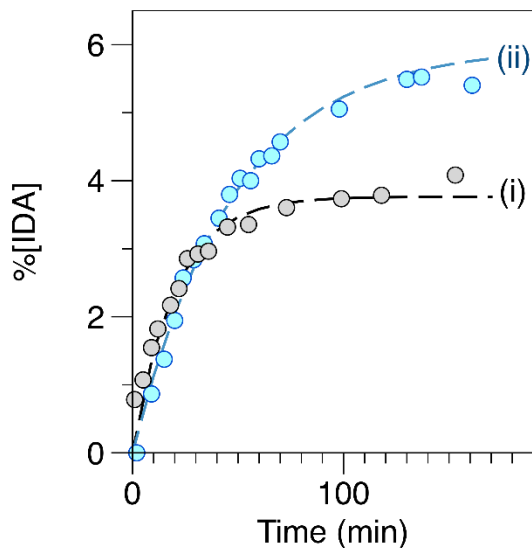


Figure 4.7: Results of dialysis experiments monitoring the dissociation of IDA from (i) IDA/**ab**/AuNP ($y = 3.76(1 - e^{-0.05t})$, $R^2=0.96$), and (ii) IDA/**p-ab**/AuNP ($y = 5.96(1 - e^{-0.02t})$, $R^2=0.99$).

The data was fit to exponential equations to determine the kinetic parameters, α and β and the results are tabulated in table 4.2.

Table 4.2: Summary of Kinetic and Equilibrium results for the release of IDA from the different nanocarriers at 37 °C.

Nanocarrier	α (%)	β (min^{-1})	K_{eq} (M^{-1})
IDA/ ab /AuNP	3.8	0.05	3.0×10^8
IDA/ p-ab /AuNP	6.0	0.02	1.6×10^8

As shown in table 4.2, the associated complex is highly favored due to the large equilibrium constants for both of the nanocarriers. The IDA/**p-ab**/AuNP system had a higher K_{eq} and slower drug release compared to IDA/**ab**/AuNP, but it was also expected to have a lower drug release

since the polymer should block the drug from desorbing from the nanocarrier. There was only a 2.2% difference in drug release between the two vehicles. Since the DNA hybridization studies had a 4.5% uncertainty, which is larger than the difference in drug release between the two vehicles, this data is inconclusive as to whether there is less drug retention in the IDA/**p-ab**/AuNP system. The drug was added to completely saturate the drug binding sites ($r = 3$) so excess IDA present in the system would give a higher than expected drug release since excess IDA would be nonspecifically bound. In future experiments, the drug release at lower drug loading and at the polymer's transition temperature can be measured to determine if the drug released at equilibrium is due to a lower drug retention or if it is due to experimental errors.

The binding constant of IDA complexed with free DNA duplexes in solution has been reported as $K = 5.14 \times 10^5 \text{ M}^{-1}$.²⁰ This is 1000 times smaller than the values calculated in both drug delivery vehicles, indicating a stronger drug-molecule complex in the AuNP systems. Stronger binding constants for molecules bound to AuNP surfaces compared to unbound molecules has been reported previously and described through a cooperative binding theory, where a higher DNA packing density leads to increased association constants.^{10,28}

Previously in our lab, the release of DOX was measured from AuNP functionalized with DNA alone (DOX/**2ab**/AuNP) and DNA and **p** (DOX/**p-2ab**/AuNP) and the release of ActD from ActD/**3ab**/AuNP, where **2ab** and **3ab** are the high affinity dsDNA strands for DOX and ActD, respectively.²⁻⁴

Table 4.3: Summary of Published Kinetic and Equilibrium results for the release of DOX and ActD from the different nanocarriers at 37 °C.

Nanocarrier	α (%)	β (min^{-1})	K_{eq} (M^{-1})
DOX/ 2ab /AuNP ⁵	28.8	0.00635	9.4×10^6
DOX/ p-2ab /AuNP ⁵	21.5	0.00429	1.9×10^7
ActD/ 3ab /AuNP ³	35.5	0.0068	1.0×10^6

As shown in table 4.3, the DOX and ActD systems had a higher percentage of drug released at equilibrium than the IDA system and a higher rate constant, which is consistent with studies that showed that IDA interacts more strongly with DNA than other anthracyclines. Unlike in the IDA system, the DOX system showed an increase in K_{eq} by about 50% with the addition of a polymer, demonstrating that the drug is more strongly bound to the **p**-AuNP system. In this system, there was a 50% decrease in K_{eq} indicating that IDA is less strongly bound in the **p**-AuNP system, but that system released less drug at equilibrium.

4.4 Conclusions

In these studies, there was an increase in DNA T_m after drug binding, indicating successful intercalation of IDA at the double helix. A thermoresponsive polymer was integrated into the system to increase drug retention. The IDA/**p-ab**/AuNP system had a higher equilibrium constant but a lower rate constant and higher percent drug release. Since the percent drug release for both systems is on the same order as the uncertainty for the DNA quantification, it is inconclusive if one nanocarrier is better than the other. The high number of IDA binding sites (120-132 IDA/AuNP), the stabilization of the DNA duplex with the addition of the anticancer drug and the high binding constant makes this a promising system as a therapeutic agent for drug delivery.

4.5 References

- (1) Giljohann, D. A.; Seferos, D. S.; Daniel, W. L.; Massich, M. D.; Patel, P. C.; Mirkin, C. A. Gold Nanoparticles for Biology and Medicine. *Angew. Chem. Int. Ed.* **2010**, *49* (19), 3280–3294.
- (2) Alexander, C. M.; Maye, M. M.; Dabrowiak, J. C. DNA-Capped Nanoparticles Designed for Doxorubicin Drug Delivery. *Chem. Commun.* **2011**, *47* (12), 3418–3420.
- (3) Alexander, C. M.; Dabrowiak, J. C.; Maye, M. M. Investigation of the Drug Binding Properties and Cytotoxicity of DNA-Capped Nanoparticles Designed as Delivery Vehicles for the Anticancer Agents Doxorubicin and Actinomycin D. *Bioconjug. Chem.* **2012**, *23* (10), 2061–2070.
- (4) Alexander, C. M.; Hamner, K. L.; Maye, M. M.; Dabrowiak, J. C. Multifunctional DNA-Gold Nanoparticles for Targeted Doxorubicin Delivery. *Bioconjug. Chem.* **2014**, *25* (7), 1261–1271.
- (5) Hamner, K. L.; Alexander, C. M.; Coopersmith, K.; Reishofer, D.; Provenza, C.; Maye, M. M. Using Temperature-Sensitive Smart Polymers to Regulate DNA-Mediated Nanoassembly and Encoded Nanocarrier Drug Release. *ACS Nano* **2013**, *7* (8), 7011–7020.
- (6) Hwu, J. R.; Lin, Y. S.; Josephrajan, T.; Hsu, M.-H.; Cheng, F.-Y.; Yeh, C.-S.; Su, W.-C.; Shieh, D.-B. Targeted Paclitaxel by Conjugation to Iron Oxide and Gold Nanoparticles. *J. Am. Chem. Soc.* **2009**, *131* (1), 66–68.
- (7) Zhang, X.-Q.; Xu, X.; Lam, R.; Giljohann, D.; Ho, D.; Mirkin, C. A. Strategy for Increasing Drug Solubility and Efficacy through Covalent Attachment to Polyvalent DNA–Nanoparticle Conjugates. *ACS Nano* **2011**, *5* (9), 6962–6970.
- (8) Zhang, X.; Servos, M. R.; Liu, J. Instantaneous and Quantitative Functionalization of Gold Nanoparticles with Thiolated DNA Using a pH-Assisted and Surfactant-Free Route. *J. Am. Chem. Soc.* **2012**, *134* (17), 7266–7269.
- (9) Murphy, C. J.; Gole, A. M.; Stone, J. W.; Sisco, P. N.; Alkilany, A. M.; Goldsmith, E. C.; Baxter, S. C. Gold Nanoparticles in Biology: Beyond Toxicity to Cellular Imaging. *Acc. Chem. Res.* **2008**, *41* (12), 1721–1730.
- (10) Rosi, N. L.; Giljohann, D. A.; Thaxton, C. S.; Lytton-Jean, A. K. R.; Han, M. S.; Mirkin, C. A. Oligonucleotide-Modified Gold Nanoparticles for Intracellular Gene Regulation. *Science* **2006**, *312* (5776), 1027–1030.
- (11) Maye, M. M.; Nykypanchuk, D.; van der Lelie, D.; Gang, O. A Simple Method for Kinetic Control of DNA-Induced Nanoparticle Assembly. *J. Am. Chem. Soc.* **2006**, *128* (43), 14020–14021.
- (12) Cobbe, S.; Connolly, S.; Ryan, D.; Nagle, L.; Eritja, R.; Fitzmaurice, D. DNA-Controlled Assembly of Protein-Modified Gold Nanocrystals. *J. Phys. Chem. B* **2003**, *107* (2), 470–477.
- (13) Di Michele, L.; Varrato, F.; Kotar, J.; Nathan, S. H.; Foffi, G.; Eiser, E. Multistep Kinetic Self-Assembly of DNA-Coated Colloids. *Nat. Commun.* **2013**, *4*.
- (14) Wang, B.; Wang, M.; Zhang, H.; Sobal, N. S.; Tong, W.; Gao, C.; Wang, Y.; Giersig, M.; Wang, D.; Möhwald, H. Stepwise Interfacial Self-Assembly of Nanoparticles via Specific DNA Pairing. *Phys. Chem. Chem. Phys.* **2007**, *9* (48), 6313.

- (15) Zhang, Y.; Lu, F.; Yager, K. G.; van der Lelie, D.; Gang, O. A General Strategy for the DNA-Mediated Self-Assembly of Functional Nanoparticles into Heterogeneous Systems. *Nat. Nanotechnol.* **2013**, *8* (11), 865–872.
- (16) Yavuz, M. S.; Cheng, Y.; Chen, J.; Cobley, C. M.; Zhang, Q.; Rycenga, M.; Xie, J.; Kim, C.; Song, K. H.; Schwartz, A. G.; Wang, L. V.; Xia, Y. Gold Nanocages Covered by Smart Polymers for Controlled Release with near-Infrared Light. *Nat. Mater.* **2009**, *8* (12), 935–939.
- (17) Chakraborty, S.; Bishnoi, S. W.; Pérez-Luna, V. H. Gold Nanoparticles with Poly(N-Isopropylacrylamide) Formed via Surface Initiated Atom Transfer Free Radical Polymerization Exhibit Unusually Slow Aggregation Kinetics. *J. Phys. Chem. C* **2010**, *114* (13), 5947–5955.
- (18) Eeckman, F.; Moës, A. J.; Amighi, K. Evaluation of a New Controlled-Drug Delivery Concept Based on the Use of Thermoresponsive Polymers. *Int. J. Pharm.* **2002**, *241* (1), 113–125.
- (19) Wang, F.; Wang, Y.-C.; Dou, S.; Xiong, M.-H.; Sun, T.-M.; Wang, J. Doxorubicin-Tethered Responsive Gold Nanoparticles Facilitate Intracellular Drug Delivery for Overcoming Multidrug Resistance in Cancer Cells. *ACS Nano* **2011**, *5* (5), 3679–3692.
- (20) Ozluer, C.; Kara, H. E. S. In Vitro DNA Binding Studies of Anticancer Drug Idarubicin Using Spectroscopic Techniques. *J. Photochem. Photobiol. B* **2014**, *138*, 36–42.
- (21) Gieseler, F.; Biersack, H.; Brieden, T.; Manderscheid, J.; Nüßler, V. Cytotoxicity of Anthracyclines: Correlation with Cellular Uptake, Intracellular Distribution and DNA Binding. *Ann. Hematol.* **1994**, *69* (1), S13–S17.
- (22) Charak, S.; Mehrotra, R. Structural Investigation of idarubicin–DNA Interaction: Spectroscopic and Molecular Docking Study. *Int. J. Biol. Macromol.* **2013**, *60*, 213–218.
- (23) Liu, L. F.; Rowe, T. C.; Yang, L.; Tewey, K. M.; Chen, G. L. Cleavage of DNA by Mammalian DNA Topoisomerase II. *J. Biol. Chem.* **1983**, *258* (24), 15365–15370.
- (24) Mukherjee, A.; Lavery, R.; Bagchi, B.; Hynes, J. T. On the Molecular Mechanism of Drug Intercalation into DNA: A Simulation Study of the Intercalation Pathway, Free Energy, and DNA Structural Changes. *J. Am. Chem. Soc.* **2008**, *130* (30), 9747–9755.
- (25) Hurst, S. J.; Lytton-Jean, A. K. R.; Mirkin, C. A. Maximizing DNA Loading on a Range of Gold Nanoparticle Sizes. *Anal. Chem.* **2006**, *78* (24), 8313–8318.
- (26) Sun, D.; Gang, O. DNA-Functionalized Quantum Dots: Fabrication, Structural, and Physicochemical Properties. *Langmuir* **2013**, *29* (23), 7038–7046.
- (27) Li, S.; Huang, S.; Peng, S.-B. Overexpression of G Protein-Coupled Receptors in Cancer Cells: Involvement in Tumor Progression. *Int. J. Oncol.* **2005**, *27* (5), 1329–1339.
- (28) Jin, R.; Wu, G.; Li, Z.; Mirkin, C. A.; Schatz, G. C. What Controls the Melting Properties of DNA-Linked Gold Nanoparticle Assemblies? *J. Am. Chem. Soc.* **2003**, *125* (6), 1643–1654.

Chapter 5

Conclusions and Future Outlook

In this thesis, I discussed my dissertation work involving the biofunctionalization of various nanoparticles for self-assembly and energy transfer applications. In Chapter 2, hydrophobic QDs were encapsulated in amphiphilic polymers and functionalized with oligonucleotides through EDC/NHS coupling and click chemistry. One of the largest challenges in this project was an inconsistent batch to batch coupling, which was hypothesized to be due to the presence of excess polymer and QD aggregates. To overcome this, the QDs were purified in a sucrose density gradient, which lead to decreased absorbance scattering, an increased DNA loading on the particles and a decreased d_h . The purified QDs were then assembled into multicolor clusters on a solid support using DNA mediated interactions. The QD dimers were released from the support and the QD-QD energy transfer was measured indirectly by comparing the PL ratio before and after assembly. An increase in PL for the QD acceptor and a decrease for the QD donor was indicative of energy transfer. The energy transfer had to be measured indirectly because QDs have a broad absorption profile that causes both the donor and the acceptor QDs in the cluster to be coexcited. To overcome these limitations that arise with QDs as energy acceptors, a bioluminescent protein was used as an energy donor to excite quantum rods (QRs) without the need for an external light source, as discussed in Chapter 3.

In Chapter 3, a bioluminescent protein from the North American firefly, *Photinus pyralis* (Ppy) was conjugated to QRs. Since the spectra was obtained with the excitation source blocked, the resulting signal is either a result of non-radiative energy transfer through bioluminescence resonance energy transfer (BRET), radiative energy transfer from unbound protein, or a combination of the two. Control experiments showed that the signal was mostly from non-radiative

energy transfer and a small amount is possibly from unbound protein illuminating the sample. Elimination of the radiative contributions to the BRET signal is important to make the incorporation of Ppy into the energy transfer QD clusters a viable option. Another limitation that needed to be overcome was the long term instability of the BRET signal. In these conjugates, I measured the stability of the BRET signal and found that the signal decreased almost entirely within 24 hours. To overcome this limitation, I used glutathione (GSH) in place of histidine (His) to facilitate the phase transfer by replacing the native organic capping ligands. After subsequent functionalization with Ppy, the BRET signal remained stable over the course of one week. His is a small, low charged molecule but GSH is a larger and more highly charged molecule, so it is hypothesized that GSH increases stability because the ligands that remain after Ppy conjugation increase the electrostatic interactions between the colloidal QRs. Future experiments can focus on incorporating the Ppy donor into the QD cluster assembly system and creating higher ordered structures with QDs or other nanomaterials such as AgNPs for biosensing applications.

In the final Chapter, I functionalized AuNPs with a thermoresponsive polymer and dsDNA that had a high affinity for IDA to create encoded nanocarriers for controlled drug delivery. Thermal melting experiments confirmed that the thermoresponsive polymer had a T_c of 51 °C and DLS measurements showed that the polymer extended past the DNA strands. At physiological temperature, the DNA was encapsulated in the AuNP conjugates, which protects IDA from desorbing from the surface. After drug intercalation, an increase in DNA T_m indicated intercalation at the double helix. Kinetics studies revealed that the addition of the thermoresponsive polymer lead to an increase in the equilibrium constant by two fold. There was only a 2.2% difference in drug release between the two vehicles, and since the DNA hybridization studies had a 4.5% uncertainty, this data is inconclusive as to whether the polymer increases drug retention. Both

vehicles showed low drug release, small dissociation rate constant of 0.02-0.05 min⁻¹ and high equilibrium constant of 1.6 x 10⁸-3.0 x 10⁸ M⁻¹, indicating that these nanoconjugates can act as efficient vehicles for in vivo drug delivery. Compared to the ActD and DOX vehicles that were developed previously in our lab, the IDA vehicles released less drug. This is consistent with the reports in literature that indicate that IDA interacts stronger with DNA than the other anthracyclines. This vehicle can be modified to increase drug targeting by further functionalizing the AuNP surface with molecules that target the receptors that are overexpressed in cancer cells.

KAITLIN JEANNE COOPERSMITH

1-014 Center for Science and Technology
Syracuse, NY 13244-4100

kcoopers@syr.edu
516-640-9061

EDUCATION

Ph.D. in Chemistry Expected: June 2015
Syracuse University, Syracuse NY
Advisor: Professor Mathew M. Maye
B.S. in Chemistry, Minor in Physics, *Magna Cum Laude* May 2011
State University of New York at Potsdam, Potsdam, NY

PUBLICATIONS

Kaitlin Coopersmith, H. Han, M. Maye, Stepwise Assembly and Characterization of DNA Linked Two-Color QD Clusters, *Langmuir*, **2015**, *Accepted*

K.L Hamner, C. M. Alexander, **Kaitlin Coopersmith**, D. Reishofer, C. Provenza, J. Dabrowiak, M. M. Maye, Using Temperature Sensitive Smart Polymers to Regulate DNA-Mediated Nanoassembly and Encoded Nanocarrier Drug Release, *ACS Nano*, **2013**, 7, 7011-7020

M. Hepel, D. Blake, M. McCabe, M. Stobiecka, **Kaitlin Coopersmith**, “Assembly of Gold Nanoparticles Induced by Metal Ions”, Chapter in a book: *Functional Nanoparticles for Bioanalysis, Nanomedicine and Bioelectronic Devices*, M. Hepel, C. Zhong (Eds.), ACS Symposium Series, Vol. 1112, American Chemical Society Washington, DC. **2012**, 207-240.

M. Stobiecka, A. Prance, **Kaitlin Coopersmith**, M. Hepel “Antioxidant effectiveness in preventing paraquat-mediated oxidative DNA damage in the presence of H₂O₂”, Chapter in a book: *Oxidative Stress: Diagnostics Prevention and Therapy*, S. Andreescu, M. Hepel (Eds.), ACS Symposium Series, Vol. 1083, American Chemical Society Washington, DC. **2011**, 211-233

M. Stobiecka, **Kaitlin Coopersmith**, M. Hepel, Resonance Elastic Light Scattering (RELS) Spectroscopy of fast Non-Langmuirian Ligand-Exchange in Glutathione-Induced Gold Nanoparticle Assembly, *J. Colloid Interface Sci*, **2010**, 350, 168-177.

RESEARCH

Graduate Research Assistant, Advisor: Dr. Mathew Maye, *Syracuse University*, 2012-Present

DNA Modified Gold Nanoparticles for Drug Delivery: Gold nanoparticles were synthesized and functionalized with dsDNA strands that had a high affinity for the clinically approved chemotherapy drug idarubicin (IDA). A thermoresponsive co-polymer was added to the surface to increase drug retention. Drug binding was analyzed through thermal DNA denaturation measurements, dynamic light scattering and kinetic studies.

DNA-Mediated Assembly of Multi-Color Qdot Clusters: CdSe/ZnS quantum dots (QD) and quantum rods (QRs) were synthesized and their interfaces were functionalized with ssDNA of 30-50 bases with a range of surface linking approaches. The DNA was used as a mediator to assemble the QDs and QRs into discrete architectures, like dimers or trimers, which can be used in single molecule sensing. This type of research is very interdisciplinary and can be utilized in future lab-on-a-chip technologies or for integrated biosensors to help detect toxins or monitor environmental conditions. The morphology and behavior of these QD/DNA conjugates were studied using transmission electron microscopy, dynamic light scattering, gel electrophoresis, Fourier Transform Infrared Spectroscopy, Ultraviolet-Visible spectroscopy and Photoluminescence spectroscopy.

Undergraduate Research Assistant, Advisor: Dr. Maria Hepel,
State University of New York at Potsdam, 2009-2011

Glutathione Induced Gold Nanoparticle Assembly: In this project, glutathione was used as a mediator to assemble gold nanoparticles. Through resonance elastic light scattering, dynamic light scattering and transmission electron microscopy, it was found that the citrate capped gold nanoparticles underwent ligand exchange with glutathione and the assembly was driven by hydrogen bonding between the glutathione molecules as well as through zwitterionic interactions.

DNA Biosensors for Studies of Interactions of Herbicides and Pesticides with DNA: This was an advanced honors research project, where DNA damage was detected through cyclic voltammetry and photoluminescence using Nile blue as a redox probe for DNA damage. The DNA was immobilized on a gold electrode through an amide bond between the oligonucleotide and a self-assembled monolayer of mercaptopropionic acid on the gold electrode. The amount of Nile blue that intercalated into reduced DNA was measured and the DNA damage in the presence of different herbicides and antioxidants were studied. This research was included in an ACS book chapter where I was a co-author.

SKILLS

Spectroscopy: Ultraviolet-Visible Spectroscopy, Fluorescence and Polarization Spectroscopy, Dynamic, Light Scattering, Fourier Transform Infrared Spectroscopy, Nuclear Magnetic Resonance

Microscopy: Atomic Force Microscopy, Confocal Microscopy, Transmission Electron Microscopy

Thermal Analysis: Thermogravimetric Analysis

Chemical Synthesis: Gold nanoparticles, Semiconductor nanocrystals, Vacuum atmosphere glovebox usage, Schlenk line techniques, Thin film deposition in solution

Computer Software: IgorPro, PhotoChemCad, Datagraph, Microsoft Office Suite, Adobe Illustrator

**HONORS
& AWARDS**

Alpha Chi Sigma Chemistry Fraternity	2011
ACS Undergraduate Award in Analytical Chemistry	2010
Joseph B. Kilmer Undergraduate Research Apprenticeship	2010
Gamma Sigma Epsilon Chemistry Honor Society	2009
Omicron Delta Kappa National Leadership Honor Society	2009
Jessie J. McNall Scholarship Recipient	2009
Phi Eta Sigma National Freshman Honor Society Member	2008

TEACHING

Graduate Teaching Assistant, *Syracuse University*, Chemistry Department

General Chemistry Recitation	Fall 2012, Spring 2015
General Chemistry for Engineers Lab	Fall 2014
Forensic Chemistry Lab	Spring 2013
General Chemistry Laboratory	Fall 2011, Spring 2012

Undergraduate Teaching Assistant, *SUNY Potsdam*, Chemistry

Organic Chemistry I Fall 2009

Tutor at the Student Success Center, *SUNY Potsdam*

General Chemistry 2008-2011

**POSTER
PRESENTATIONS**

Kaitlin Coopersmith, Hyunjoo Han, Mathew M. Maye, "DNA Mediated Assembly and Purification of Qdot Clusters"
(MRS Fall Meeting, December 2014)

Kaitlin Coopersmith, Mathew M. Maye, "The DNA Mediated Assembly and Ultracentrifugation Based Purification of Multi-color Qdot Clusters"
(Stevenson Biomaterials Poster Session, October 2014)

Kaitlin Coopersmith, R. Davon Slaton, Hyunjoo Han, Mathew M. Maye, "Stepwise Assembly of multicolor qdot clusters using a DNA-Mediated Approach"
(246th National Meeting of the ACS, September 2013)

Kaitlin Coopersmith, Mathew M. Maye, "Oligonucleotide Functionalized Quantum Dots"
(Biotechnology Research Symposium, May 2013)

Kaitlin Coopersmith, Janet Peachy, Maria Hepel, "Paraquat and Catechol-Mediated DNA Damage"
(National Council for Undergraduate Research, April 2011)

Amanda Prance, **Kaitlin Coopersmith**, Magdalena Stobiecka, Maria Hepel, "DNA Sensors for the Assessment of DNA Damage by Atrazine"
(National Conference on Undergraduate Research, April 2011)

Kaitlin Coopersmith, Magdalena Stobiecka, Maria Hepel, "Monitoring of the interactions of biomarkers of oxidative stress-glutathione with gold nanoparticles using elastic light scattering"

(Annual Northern NY Local Section of the ACS Undergraduate and Graduate Chemistry Research Symposium, April 2011)

Kaitlin Coopersmith, Maria Hepel, Magdalena Stobiecka, “Paraquat-Mediated DNA Damage”

(Learning and Research Fair at SUNY Potsdam, April 2011)

Kaitlin Coopersmith, Magdalena Stobiecka, Maria Hepel, “Fluorescence Resonance Energy Transfer Between Functionalized Dyes and Gold Nanoparticles”

(Learning and Research Fair at SUNY Potsdam, April 2011)

Amanda Prance, **Kaitlin Coopersmith**, Maria Hepel, “DNA Intercalation biosensors for studies of interactions of herbicides and pesticides with DNA”

(240th National Meeting of the ACS, August 2010)

Kaitlin Coopersmith, Magdalena Stobiecka, Maria Hepel, “Fluorescence Resonance Energy Transfer between Functionalized Coumarin Dyes and Gold Nanoparticles

(240th National Meeting of the ACS, August 2010)

Kaitlin Coopersmith, Magdalena Stobiecka, Maria Hepel, “Nanomaterial surface energy transfer (NSET) between multiple fluorescent dyes and gold nanoparticles”

(ACS North Eastern Regional Meeting, June 2010)

Amanda Prance, **Kaitlin Coopersmith**, Magdalena Stobiecka, Maria Hepel, “DNA sensors for the assessment of DNA damage by Atrazine”

(ACS North Eastern Regional Meeting, June 2010)

Amanda Prance, **Kaitlin Coopersmith**, Magdalena Stobiecka, Maria Hepel, “DNA Biosensors for Studies of Interactions of Herbicides and Pesticides with DNA”

(Learning and Research Fair at SUNY Potsdam, April 2010)

Kaitlin Coopersmith, Magdalena Stobiecka, Maria Hepel “Resonance Energy Transfer in a Multi-component Fluorescent Dye Systems Influenced by Gold Nanorod Quadrupole Surface Plasmon Coupling”

(Pittsburgh Conference on Analytical Chemistry and Applied Spectroscopy, March 2010)

Kaitlin Coopersmith, Magdalena Stobiecka, Maria Hepel, “Radiationless processes in the Multicomponent System Coumarin-Fluorescein-Rhodamine in the Presence of Gold Nanoparticles”

(238th National Meeting of the ACS, August 2009)